The interplay of the cell membrane with the cytoskeleton

DISSERTATION

zur Erlangung des akademischen Grades

Doctor rerum naturalium
(Dr. rer. nat.)

vorgelegt

der Fakultät Mathematik und Naturwissenschaften
der Technischen Universität Dresden

von

Dipl.-Phys. Jochen Albert Max Schneider
geboren am 21. August 1985 in Berlin

MAX-PLANCK-INSTITUT FÜR PHYSIK KOMPLEXER SYSTEME

Dresden, 2016

Eingereicht am: 19. Februar 2016
Verteidigt am: 27. Juni 2016

1. Gutachter (1st referee): Prof. Dr. Frank Jülicher
2. Gutachter (2nd referee): Prof. Dr. Marino Arroyo

Acknowledgments

This thesis is dedicated to my former physics school teacher Frank Pozniak. He raised my fascination for physics, which finally made me choose physics at university and continue research afterwards, leading to my PhD work. This choice shall emphasize the important role of teachers for the development of children and their interests for subjects, which is, unfortunately, more and more underestimated nowadays. Not underestimated but equally important for a successful completion of a PhD project is, besides the intrinsic fascination for the subject, the support from family and friends. I am very glad that I could rely on so many people every day. Special thanks shall go to my mother and my grandfather. My mother taught me how to be persistent and determined and my grandfather has always been a shining example for the nobility of academia.

From the scientific point of view I would like to thank, primarily, my supervisor Guillaume Salbreux who introduced me to biophysical research and guided me with great patience, enthusiasm and expertise. I also highly appreciated the advices of Frank Jülicher, director of the Biophysical Division at the Max Planck Institute for the Physics of Complex Systems. It helped me to put the often technical and detailed work into a broader scientific perspective. Moreover, I would like to thank all my colleagues who created a very open-minded, cooperative working environment, which led to many fruitful discussions.

Moreover, I would like to thank the Max Planck Society and The Francis Crick Institute for providing exceptional working conditions, which facilitated a very creative and focused work.

Abstract

Past work has attributed a major role for the mechanics and shape of a biological cell to the cell cortex, a viscoelastic polymer network under contractile tension, and as the outermost part of the cell cytoskeleton located beneath the cell membrane. Its importance has been shown, for instance, for the spatial separation of daughter cells during cell division, for certain modes of cell migration and for the morphology of tissues. Furthermore, it has been discussed more recently that the contractility of the cortex can cause the membrane, which is anchored to the cortex via linker proteins, to buckle into out-of-plane microstructures, such as bulges, buds and tubes. This observation has been proposed as a fast mechanism to buffer occurring membrane excess area and as a regulator of membrane tension.

In this thesis we study the mechanical effect of cell membrane buckling by treating the cell membrane as an anchored lipid bilayer with a surface tension and a bending energy. In order to account for the anchoring we introduce two different approaches. In the first approach we anchor a membrane with imposed surface area along a discrete square lattice and calculate the resulting equilibrium shape of the membrane. We find that within each lattice element the membrane shape is close to an axisymmetric shape if anchors are located on the edges of the square. Based on this finding, in the second approach, we model the membrane as a collection of axisymmetric protrusions where each protrusion is anchored along its basal boundary. The buckling shapes are determined by the membrane excess area, a hydrostatic pressure difference across the membrane and a local point force, accounting for cortex filaments pushing on the membrane. The membrane tension is set by the imposed membrane area. We then use this description of an anchored membrane to propose a model for the global cell mechanics and geometry based on the interplay of cell membrane and cortex. This model involves a closed system of equations describing the balance of osmotic and hydrostatic pressure differences, the force balance at the cell surface and a membrane area elasticity due to membrane fluctuations. With the help of this model we predict that the membrane takes a buckled shape as a result of the contractility of the cortex. We obtain shape diagrams for the occurrence of out-of-plane membrane structures, such as blebs, microvilli and tubular invaginations, depending on the contractility, the linker density and the cell osmolarity. Furthermore, we investigate the role of membrane buckling for cytokinesis, the final stage of cell division where the cell separates into two daughter cells. We show how a buckling asymmetry between the two cell poles of the dividing cell can trigger a flow of lipids across the cleavage furrow. Moreover, we hypothesize that the membrane buckling could cause an effective surface elasticity helping to stabilize cell division.

Zusammenfassung

In der Vergangenheit wurde gezeigt, dass der Zellkortex, ein viskoelastisches, kontraktiles Polymernetzwerk direkt unterhalb der Zellmembran, als Teil des Zellskeletts eine bedeutende Rolle für die Mechanik und die Form von biologischen Zellen einnimmt. Wichtigen Einfluss hat er bei der Separation von Tochterzellen während der Zellteilung, bei bestimmten Arten der Zellfortbewegung und bei der Formgebung von Zellgeweben. Weiterhin wurde kürzlich gezeigt, wie die Zellmembran, die mittels spezieller Proteine mit dem Kortex verankert ist, als Folge der Kontraktilität im Kortex kleine Wölbungen, Knospen und Finger ausbilden kann. Diese Deformationen treten auf, um Zusatzmembran aufzufangen und die Oberflächenspannung der Membran zu regulieren.

In dieser Arbeit untersuchen wir den mechanischen Effekt der beschriebenen Deformationen, in dem wir die Zellmembran als eine verankerte Lipiddoppelschicht mit assozierter Oberflächenspannung und Krümmungsenergie beschreiben. Um ihrer Verankerung Rechnung zu tragen, folgen wir zwei Ansätzen. In ersterem verankern wir eine Membran mit gegebener Oberfläche entlang eines diskreten, quadratischen Gitters und berechnen die resultierende Gleichgewichtsform der Membran. Wir finden, dass die Membran innerhalb jedes Gitterquadrats fast rotationssymmetrische, lokale Wölbungen ausbildet, wenn Ankerpunkte auf den Kanten des Gittersquadrats platziert sind. Darauf aufbauend modellieren wir mit dem zweiten Ansatz die Membran als Zusammenschluss von rotationssymmetrischen Ausstülpungen, wobei jede dieser entlang ihres unteren Randes verankert ist. Sie sind weiterhin durch die vorhandene Zusatzfläche, einen hydrostatischen Druckunterschied zwischen beiden Membranseiten, sowie durch eine Punktkraft, hervorgerufen von kortikalen Filamenten, bestimmt. Die zugehörige Oberflächenspannung der Membran bestimmen wir durch die Fixierung der Membranfläche. Wir benutzen diese Beschreibung für eine verankerte Membran, um ein Modell für die globalen geometrischen und mechanischen Eigenschaften der Zelle, basierend auf der Wechselwirkung von Zellmembran und -cortex, aufzustellen. Dieses Modell beinhaltet ein geschlossenes Gleichungssystem für das Gleichgewicht von osmotischer und hydrostatischer Druckdifferenz, dem Kräftegleichgewicht an der Zelloberfläche und der Oberflächenelastizität, ausgehend von Membranfluktuationen. Mit Hilfe dieses Modells können wir schlussfolgern, dass aufgrund der Kontrakilität des Zellkortex lokale Deformationen der Membran auftreten. Noch größere Deformationen, wie Blasen, Mikrovilli oder röhrenförmige Einstülpungen können wir mittels Phasendiagrammen vorhersagen, die von der Kontraktilität im Kortex, der Dichte der Membranankerpunkte und der Zellosmolarität abhängen. Des Weiteren untersuchen wir die Rolle der beschriebenen Membranwölbungen während der Zytokinese, der letzten Phase der Zellteilung, wo sich die Zelle in zwei Tochterzellen zerteilt. Wir zeigen, wie eine Asymmetrie dieser Deformationen zwischen den beiden noch verbunden Tochterzellen zu einem Lipidfluss entlang der Teilungsfurche führen kann. Darüber hinaus stellen wir die Hypothese auf, dass diese Deformationen zu einer effektiven Oberflčhenelastizität führen, die zur Stabilisierung der Zellteilung beitragen könnte.

CONTENTS

List of important symbols **17**

1 Introduction **19**

1.1 Internal organization of eukaryotic cells 20
  1.1.1 The cytoskeleton and its function 21
  1.1.2 The cell membrane 24
1.2 Cell division 26
1.3 Physics of lipid bilayer membranes 28
  1.3.1 The energy of curved lipid bilayer membranes 28
  1.3.2 Shape fluctuations 31
  1.3.3 Equilibrium shape equations 33
1.4 Scope of this thesis 38

2 A membrane bound at discrete anchoring points **45**

2.1 Membrane anchors arranged on a square lattice . . . 46
2.2 Solution of the shape equation 49
2.3 Mechanical properties for constant surface area . . . 52
  2.3.1 Membrane surface tension 52
  2.3.2 Anchoring forces 56
2.4 Equilibrium shapes for constant surface area 56
  2.4.1 The limit of zero pressure difference and corner anchors only 58

3 A membrane as a collection of protrusions 61
3.1 Shape equations for axisymmetric membrane protrusions 62
3.2 Equilibrium shapes for constant surface area 66
3.2.1 For zero pressure difference 66
3.2.2 For inflating pressure differences 68
3.2.3 For compressing pressure differences 69
3.2.4 For an additional point force at the protrusion tip 71
3.3 Mechanical properties for constant surface area . . . 74
3.3.1 Membrane surface tension 74
3.3.2 Lateral membrane tension 76
3.3.3 Vertical protrusion force 79
3.4 Combining protrusions to a membrane 79
3.4.1 Flow equation for the lipid exchange between protrusions 81
3.5 Equilibrium area distribution between coupled protrusions 82
3.5.1 Without force perturbations 85
3.5.2 With point force perturbations 87
3.5.3 With partial point force perturbations 88

4 Applications to cell biophysics 91
4.1 The cell membrane as a collection of protrusions . . 92
4.2 Cell mechanics based on the membrane-cortex interplay 94
4.2.1 Closed description 94
4.2.2 Self-consistent solution 98
4.3 Membrane blebs and tubes 103
4.3.1 Caused by cortical filaments and lipid flow . . 103
4.3.2 Caused by the discrete membrane anchoring . 106

4.4 Cell membrane mechanics during cytokinesis 112
4.4.1 Membrane buckling due to cell pole contractions 112
4.4.2 Flow equation for lipid exchange across the cleavage furrow 115
4.4.3 Membrane buckling as a contribution for cell elasticity during cytokinesis 120

5 Conclusions and outlook 125

A Differential geometry of surfaces 133

B Variational principle and the shape equations 137
B.1 Variation calculus 137
B.2 Shape equations in Monge parameterization 139
B.3 Shape equations in arc length parameterization . . . 143

C Derivation of the anchored membrane sheet solution 153

D Numerical solution for protrusion shapes 167

E Membrane protrusions in analytical limits 181
E.1 Weak-bending approximation 181
E.2 Zero-rigidity approximation 186
E.3 Tube approximation 189

F Alternative lateral tension expression 193

G Self-consistent solution for the membrane-cortex layer 197

References 201

List of figures 219

LIST OF IMPORTANT SYMBOLS

Geometrical quantities

Λ	contour length of a membrane protrusion
Ω	membrane excess area
ψ	tilt angle between contour line and z-axis
ξ	mesh size of the anchoring lattice
A	(cell) membrane area
$A_{\parallel}$	projected area of a membrane sheet
C_0	spontaneous curvature
h	elevation of membrane in z-direction
H, $\mathcal{K}$	mean curvature, Gaussian curvature
L	elongation of a membrane protrusion in z-direction
l	protrusion diameter
R	cell radius
S	apparent cell surface area
V	(cell) volume enclosed by the membrane

Mechanical quantities

$\mathcal{F}$	(mechanical) membrane energy

Δp	pressure difference across the membrane
γ, γ^*	membrane surface tension, $\gamma^* = \gamma + \frac{\kappa}{2} C_0^2$
$\gamma_{\|}$	lateral membrane tension
κ, κ_{G}	bending rigidity, Gaussian rigidity
$\mathcal{T}$	temperature
σ	stress
f	point force at the membrane protrusion tip
f_{a}	anchor force per linker protein
K	elastic modulus
T	active contractile tension in the cell cortex

Other physical quantities

Π_{ext}	external osmotic pressure of a cell
k_{B}	Boltzmann constant, $k_{\mathrm{B}} = 1.380658 \cdot 10^{-23}\,\mathrm{J\ K^{-1}}$ [1]
N_{int}	number of solute molecules inside the cell
N_{l}	number of lipids
N_{p}	number of protrusions on the cell surface
t	time

Other mathematical symbols

$\delta(x)$	Dirac delta function
δ_{ij}	Kronecker symbol
$\nabla_{\|}$	two-dimensional Nabla operator
ρ, φ, z	cylindrical coordinates
$\triangle_{\|}$	two-dimensional Laplace operator
s, u	arc length and normalized arc length, $u = 2s/\Lambda$
x, y, z	cartesian coordinates

INTRODUCTION 1

Biological organisms are known as one of the most complex systems. Their metabolisms and reproduction mechanisms follow actively[1] driven, highly dynamic processes. Nevertheless, the progress in experimental techniques during the last century, and therewith the ability to observe and measure these processes quantitatively, is increasingly triggering the demystification of this complexity. *Biochemical pathways* were identified as blueprints for signaling and remodeling in biology. Lately, physical principles have gained more attention as a second important framework. Known and extended concepts of thermodynamics and statistical physics, of mechanics and hydrodynamics are used to describe many different biological processes across all length scales.

This work applies mechanical concepts on the cellular level, more precisely on the outermost part of most eukaryotic cells, the cell membrane coupled to the underlying cytoskeleton. In this introductory chapter we first give an overview of the internal cell organization with an emphasis on cell membrane and outer cytoskeleton. Afterwards, we present previously developed physical concepts for the description of lipid bilayer membranes. Both the biological and the physical introduction are then used to motivate this work, based

---

[1] Here *active* means under consumption of externally provided energy, see also section 1.1.1.

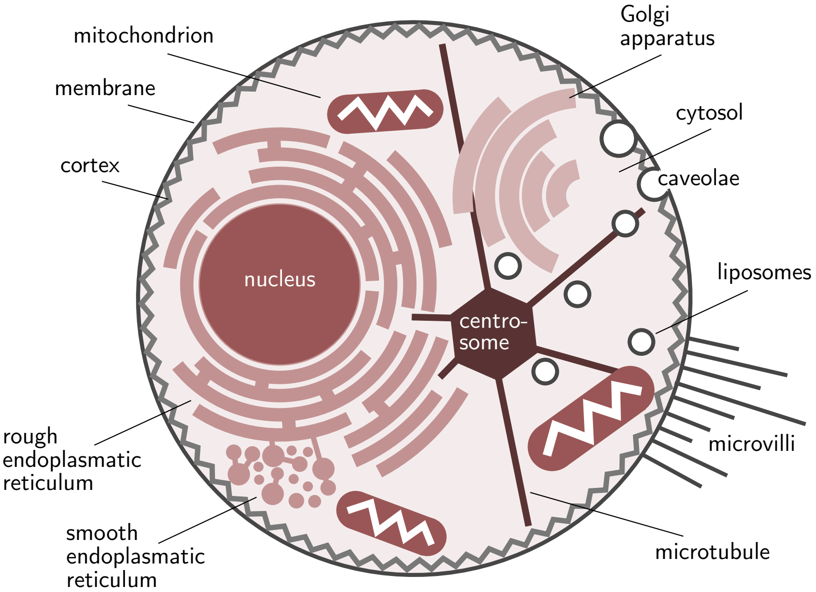
mitochondrion
membrane
cortex
Golgi apparatus
cytosol
caveolae
nucleus
centro-some
liposomes
microvilli
rough endoplasmatic reticulum
smooth endoplasmatic reticulum
microtubule

Figure 1.1 | **Illustration of the internal cell organization.**

on recent experimental and theoretical findings. Finally, we give an outlook to the following chapters.

1.1 | Internal organization of eukaryotic cells

The knowledge of the principal internal organization of living organisms grew during the last centuries in the same way as the optical observation methods developed. Initial observations with simple optical lenses gave only a poor insight compared to modern techniques such as, for instance, *confocal microscopy* [2–4] or *electron microscopy* [5–7]. One of the first key discoveries was that every biological organism consists of minimal, self-sustaining entities, so-called *biological cells* [8]. Since that time the progressive collection of further information led to a well accepted picture of the principal internal organization of cells [9]. Based on this, organisms can be divided into three *domains*: *archaea*, *bacteria* and *eukaryotes* [10]. The first two are often summarized as *prokaryotes*. In this work we will focus on eukaryotic cells, in particular on animal cells. An illustration of their principal internal structure is shown in Figure 1.1.

An important difference between prokaryotes and eukaryotes is that eukaryotic cells contain a *cell nucleus*. It hosts the *deoxyribonucleic acid* (*DNA*), which stores the genetic information of the organism, and belongs to the group of *organelles* inside the cell (see Figure 1.1 for other organelles). Each organelle fulfills a certain task in the *metabolism* of the cell. Besides organelles, two other important cellular structures are the *cytoskeleton* and the *membrane*, discussed further in the following.

1.1.1 | The cytoskeleton and its function

The cytoskeleton consists of three main protein polymer structures, *microtubules*, *intermediate filaments* (not shown in Figure 1.1) and *actin filaments* [9]. Together with multiple other associated proteins they are crucial for the shape and the mechanical properties of a cell and also take part in the regulation of the internal cell traffic.

For this work the most important cytoskeletal structure is the *cell cortex*, which is a thin layer of about 200 nm thickness, located right underneath the cell membrane [11]. It is predominantly built by the protein monomer *actin*, which has a typical diameter of 5 nm [12]. These monomers polymerize to double-stranded, helical filaments, which are bundled and cross-linked via *cross-linker proteins* to a polymeric meshwork with mesh sizes ranging from 20 nm to 250 nm

[13, 14][2]. Such a meshwork is illustrated in Figure 1.2.

The actin meshwork is highly dynamic as it undergoes a continuous turnover. This is, on the one hand, due to actin monomers attaching and detaching from filaments with a characteristic turnover time in the range of seconds to tens of seconds [16, 17]. On the other hand, also cross-linker proteins can change their actin binding partners at timescales comparable to those of actin turnover [17–19]. As a consequence of the turnover, the cell cortex is a *viscoelastic* medium, elastic because of the dense meshwork geometry on time scales shorter than the turnover time, viscous on larger timescales due to the dynamic rearrangements within the meshwork [16, 20–22].

Besides the viscoelastic character, the cell cortex is also an *active* medium. It is actively driven by two-headed bundles of myosin motor proteins, which exert local forces to the meshwork by consuming energy from *ATP hydrolysis* [23]. On average, this leads to an active contractile tension inside the cell cortex T, which can vary from $10\,\mathrm{pN}/\mu\mathrm{m}$ to $1000\,\mathrm{pN}/\mu\mathrm{m}$, not only depending on the cell type but also on the cell state [16, 24]. The exact details of the relationship between this active tension and the local force generation in the meshwork is not yet fully understood. However, experiments suggest a simple saturation relation between the tension and the number of active myosin motors N_m [25, 26]:

$$T = T_\mathrm{m}^\mathrm{eff}\,\frac{(1+N^*)N_\mathrm{m}}{N_\mathrm{m}+N^*} \quad \overset{N^*\to\infty}{\longrightarrow} \quad T = T_\mathrm{m}^\mathrm{eff}\,N_\mathrm{m}. \qquad (1.1)$$

Here N^* is the characteristic saturation number which leads to a linear relationship between myosin motors and tension as it goes to infinity. The coefficient $T_\mathrm{m}^\mathrm{eff}$ can be seen as an effective contribution of a single myosin motor to the overall tension. In an order of magnitude

---

[2] Thermal fluctuations have only a small influence on actin filaments in the cell cortex as their persistence length is of the order of $15\,\mu\mathrm{m}$ [15].

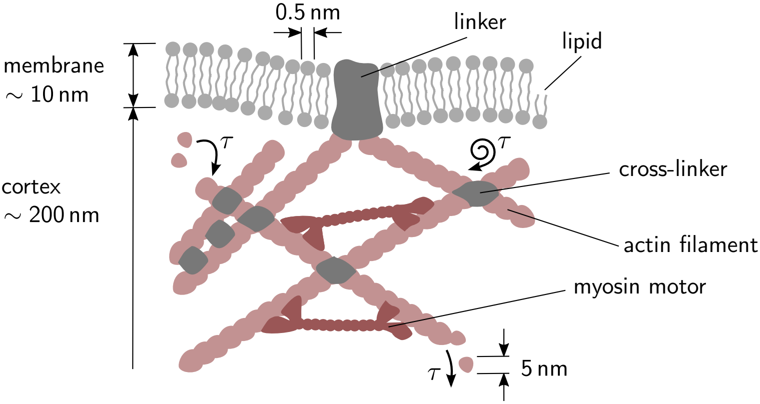

Figure 1.2 | Illustration of the cell membrane with the underlying cell cortex. The arrows with the symbol τ indicate the turnover of actin monomers and (cross-)linker proteins (see text).

estimate it can be expressed as $T_{\mathrm{m}}^{\mathrm{eff}} \simeq f_{\mathrm{mf}} l_{\mathrm{mf}} / S n_{\mathrm{mf}}$, where n_{mf} is the number of myosin motors bundling to one motor filament, f_{mf} the force exerted by one such filament, l_{mf} its length and S the apparent cell surface area, spanned by the cell cortex [27].

The cell cortex is also called *actomyosin cortex* because of its multifaceted and dynamic properties dictated by actin and myosin. Due to these properties it is, to a large extent, the determining cellular structure for the global mechanics and morphology of the cell [16, 28]. A prominent example is the cell rounding at the beginning of the final phase of cell division, caused by enhanced myosin activity and thus enhanced contractile tension in the cortex [29–31]. Other examples can be found in migrating cells where the interplay of tension and cortex remodeling can trigger the motility [32, 33], in early embryonal development where the actomyosin flow leads to left-right symmetry breaking [34], or in multicellular systems where the tension maintains the principal tissue structure and guides morphogenesis [35–38].

1.1.2 | The cell membrane

The cell membrane is the outermost structure of eukaryotic cells. It consists of amphiphilic lipids with *hydrophilic heads* and *hydrophobic tails*, which assemble to a *bilayer* with an inner and an outer *leaftlet*, where the hydrophobic tails face each other (see Figure 1.2). The typical thickness of the bilayer is of the order of 10 nm to which the hydrophilic head contributes with a radius of approximately 0.5 nm [9]. Besides lipids itself the bilayer is enriched by different types of membrane proteins. Those which are permanently embedded in the membrane are called *integral* membrane proteins, those which only attach occasionally from the outside *peripheral* membrane proteins [39]. Both types play an important role for signal and nutrient transduction across the membrane and act as adhesion sites for other proteins inside and outside the membrane [9][3]. Special channel proteins establish gateways for small particles, such as ions [41]. Curvature inducing proteins, such as *clathrin* or *caveolin*, trigger *cytosis*, the intracellular transport of material via small lipid vesicles called *endosomes* [42,43]. A particularly important class of proteins are the so-called *linker proteins*. They provide binding sites for both actin filaments and integral membrane proteins and, thus, are responsible for the anchoring of the membrane to the cytoskeleton. Common examples for these proteins are *ezrin*, *radexin* and *moesin* [44, 45]. Their mean distance lies between 0.2 μm and 1 μm [46]. Equivalently to cross-linkers in the cell cortex also linker proteins have characteristic turnover times. The turnover between linker and cortex is of the order of less than a second, the turnover between linker and membrane of the order of a few seconds [47].

Due to its many microscopic ingredients the cell membrane is highly dynamic, driven by thermal and partly also active random processes. Its shape is undulated by thermal and actively stimulated fluctuations of different wavelengths [48–55]. Lipids can switch leaflets by spontaneous and induced *flip-flop* events. Most lipids switch on timescales of a day per lipid, however, some special types can switch in only a few milliseconds [56–58]. Furthermore, lipids can spin and, more importantly, diffuse laterally, in the same way as membrane proteins. The diffusion constant of freely diffusing lipids is of the order of $10\,\mu\mathrm{m}^2/s$ [59, 60]. The diffusion constant of integral membrane proteins is approximately one order below that of lipids [61, 62].

---

[3] It is interesting to note that membrane proteins could make up to 30 % of all genetically encoded proteins [40].

The diffusive character of the membrane motivated the development of a relatively simple membrane picture, the *mosaic model* [63]. Assuming an averaged shape without fluctuations, it regards the membrane as a locally flat, incompressible, two-dimensional fluid, homogeneous in composition. However, recent observations suggest that the actual membrane state is more complicated, of which two aspects are especially interesting for this work. First, the interaction between membrane and cell cortex via linker proteins can divide the membrane into local compartments [13, 64, 65]. Cortical filaments act as *fences* and hinder the free diffusion between the different compartments, a characteristic *hop diffusion* is observed instead [59, 66]. Second, the membrane is often not completely flat attached to the cell cortex but exhibits small, persistent out-of-plane microstructures, such as extracellular lipid assemblies, *caveolae* or *microvilli* [43, 67–69]. Since the pure membrane reacts, indeed, inelastic regarding lateral tensions[4], these microstructures could act as membrane buffers giving the membrane an effective extra expansibility [71–77]. Additionally, on time scales larger than a few minutes up to an hour, the modulation of endocytosis and exocytosis could also mediate the change of membrane area [78–82].

---

[4] Experimentally lipid bilayers and cell membranes exhibited a maximal stretch of approximately $4\,\%$ close to lytic tensions of the order of $10^4\,\mathrm{pN}/\mu\mathrm{m}$ [70].

1.2 | Cell division

For the development of life in general and of multicellular organisms in particular it is crucial that cells replicate. Initially, different hypotheses for this replication process were discussed, before, finally, it was observed that the replication is achieved by a periodic division of each mother cell into two equal daughter cells (see Figure 1.3a,b) [83][5]. Later, different cell phases prior the observable division were identified and summarized in the *cell cycle* [9]. It consists of the *I-phase* or *interphase* where the cell is growing and DNA is replicated, and the *M-phase* or *mitotic phase* where the actual division takes place.

The mitotic phase can be subdivided into *mitosis* and *cytokinesis*[6]. When the cell enters mitosis it rounds up by stiffening the cortex and increasing the tension in it [29–31, 86, 87]. At the same time microtubules assemble into a *spindle* structure [88, 89], for which the rounding acts as a stabilizer [86, 90, 91]. This spindle breaks the symmetry of the cell and regulates the separation of DNA into two daughter nuclei [92, 93]. At the end of this process the cell consists of two *cell poles* (Figure 1.3a) and enters cytokinesis by ingression of the *cleavage furrow* (Figure 1.3b) whose position is mainly determined by the spindle [94–96]. Its ingression is caused by a contractile ring where myosin is further enhanced [97–101]. The contraction proceeds until the constriction becomes large enough to split the cell apart.

In a recent work Sedzinski *et al.* showed that during cytokinesis the position of the cleavage furrow can destabilize, sometimes accompanied by oscillations of the cell pole volumes (Figure 1.3c,d)

---

[5] In special cases also asymmetric divisions can occur [84] or the mother cell can divide into more than two daughter cells [85].

[6] Besides mitosis *meiosis* is an alternative process, in which four daughter cells develop, each with half the genetic information compared to the mother cell.

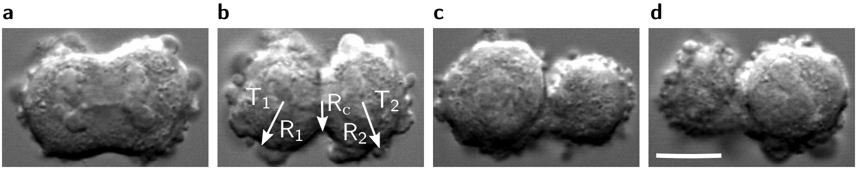

Figure 1.3 | Cell pole oscillations during cytokinesis. Here an L929 mouse fibroblast cell is shown, which has already finished the internal preparation for cell division, in **a**, *e.g.*, two separate nuclei are visible. Under certain conditions (see text), the spatial separation, accomplished by ingression of the cleavage furrow (**b**), can destabilize mechanically [26]. One *pole* of the cell contracts then, the other expands (**c**). Sometimes this leads to persistent oscillations with periodic expansions and contractions on either side (**d**). Here one period lasts about 6 min. **b** includes parameters for a theoretical modeling (see (1.2)). Image taken with a bright field microscope, scale bar: 10 μm [Images provided by Andrea Pereira, University College London].

and terminated by an aborted division [26]. A supporting theoretical model describes the cell poles as overlapping spheres with pole radii R_1 and R_2 (see Figure 1.3), pole volumes V_1 and V_2, and the conserved total volume $2V_\mathrm{s}$. The shape evolution is described by the linear dynamic ansatz

$$\frac{\alpha}{V_\mathrm{s}}\frac{dV_1}{dt} = -\frac{\alpha}{V_\mathrm{s}}\frac{dV_2}{dt} = -\underbrace{\left[\,2\frac{T_1}{R_1} - 2\frac{T_2}{R_2}\,\right]}_{\Delta p_\mathrm{Laplace}} - \frac{K_\mathrm{3D}}{V_\mathrm{s}}(V_1 - V_2), \qquad (1.2)$$

where α a friction coefficient. The right-hand side corresponds to the total pressure difference between the cell-poles. It consists of an elastic term with the *bulk compression modulus* [102]

$$K_\mathrm{3D} := V\left.\frac{d\Delta p}{dV}\right|_\mathrm{sym}, \qquad (1.3)$$

evaluated at the state where the two cell poles are symmetric and a term $\Delta p_\mathrm{Laplace}$, representing *Laplace's law* [103, 104]. This, in turn, depends on the contractile tensions T_1 and T_2 inside the cortex of both poles. As is discussed in more detail in [26], these tensions are coupled to the dynamics of actin, for which a second dynamic equation is proposed that takes into account the turnover of actin filaments. Overall, the stability analysis of this model reveals that the observed instability of cell division is triggered by three parameters: the tension in the symmetric case T_s, the turnover rate τ and the bulk elasticity $K_{3\mathrm{D}}$. It can be deduced that the following condition must be satisfied approximately in order to guarantee stable cell division:

$$\frac{T_\mathrm{s}}{R_\mathrm{s} K_{3\mathrm{D}}} \approx 1. \tag{1.4}$$

Here R_s is the radius of the two symmetric cell poles.

1.3 | Physics of lipid bilayer membranes

The physical modeling of cell membranes focuses mainly on two aspects. One is the lateral organization of lipids and membrane proteins, *e.g.*, by *molecular dynamics simulations* [105]. The second, which is relevant for this thesis, is the geometrical shape adopted by cell membranes. For simplicity, most of the past work has focused here on fluid membranes, ignoring the anchoring to an underlying cell cortex. From now on, we will call these not anchored membranes *lipid bilayer membranes* or simply *membranes.*

1.3.1 | The energy of curved lipid bilayer membranes

The observation of non-spherical, *e.g.*, biconcave, shapes of red blood cells and lipid vesicles suggested that the shape of lipid bilayer membranes, in contrast to soap bubbles, is not only determined by surface tension [106–109]. In principle, these shapes can be described by taking into account an additional *bending rigidity*, giving rise to a curvature energy [106, 110, 111]. Experimental measurements found that this rigidity is of the order of $20\,k_{\mathrm{B}}\mathcal{T}$ [112]. Several curvature energy expressions have been proposed, accounting for different lipid bilayer properties such as slow flip-flop of lipids between leaflets (see section 1.1.2) [113, 114]. However, often it is sufficient to treat the membrane as a single rigid layer. Especially for cell membranes, which consist of a lipid mixture, this is a good approximation, as they usually contain components which can switch leaflets relatively fast [57, 58]. Then the bilayer character is negligible. The curvature energy of such a simplified membrane is written in terms of the *mean curvature* $H = (C_1 + C_2)/2$ and the *Gaussian curvature* $\mathcal{K} = C_1 C_2$, where C_1 and C_2 are the principal curvatures of the surface (for details see appendix A). Together, H and K uniquely define the curvature at each point of the membrane and the expression for the energy is given by integrating the curvature over the entire membrane surface area A [110]:

$$\mathcal{F}_{\mathrm{C}} = \int dA \left[\frac{\kappa}{2} (2H - C_0)^2 + \kappa_{\mathrm{G}} \mathcal{K} \right] . \tag{1.5}$$

Here the bending rigidity κ, the *Gaussian rigidity* κ_{G} and the *spontaneous curvature* C_0 are intrinsic material properties of the membrane. The latter accounts for an asymmetry in the bilayer composition, *e.g.*, different types of lipids in the inner and outer leaflet or a larger number of proteins embedded in one of them. The model in (1.5) has been the basis to study and verify many different membrane shapes of, for instance, vesicles [106,107,109,115], membrane tubes [116,117] and invaginations [118, 119].

We use (1.5) in this work with some modifications and simplifications. First, we focus on closed surfaces. Then the *Gauss-Bonnet theorem* states that the integral over the Gaussian curvature is topologically invariant [120]. That is, if the membrane is not changing its topology this term gives only a constant contribution to the energy. Second, throughout this work we assume that the composition of the membrane is homogeneous. Then the parameters κ and C_0 are constants and can be excluded from integration[7]. Furthermore, we add three further terms to (1.5) which introduce a coupling between physical and geometrical quantities: the coupling between the *surface tension* γ and the *surface area* A of the membrane; the coupling between the *pressure difference* $\Delta p := p_{\text{int}} - p_{\text{ext}}$ accross the membrane and the *volume* V enclosed by the membrane; and the coupling of a *point force* f perpendicular to the membrane and the *elongation* L of the membrane at the position of the point force. Then the energy reads as[8]

$$\mathcal{F} = \frac{\kappa}{2} \oint dA (2H - C_0)^2 + \gamma A - \Delta p V - f L. \tag{1.6}$$

For each of the introduced couplings two *ensembles* are distinguishable. Either the physical parameter is fixed and the geometrical quantity adjusts accordingly or the geometrical quantity is conserved and the related physical parameter acts as a *Lagrange multiplier*, ensuring the conservation of the associated geometrical parameter. One example is the often assumed conservation of membrane area A. This gives an additional condition, which determines the surface tension γ.

---

[7] Reported gel-like membrane inhomogeneities, called *lipid rafts*, would modulate the bending rigidity locally but seem to be relatively small in cells [121, 122].

[8] Note that in general the surface tension γ is not spatially invariant. However, as we assume here a homogeneous membrane composition γ adopts a constant value in the entire membrane.

1.3.2 | Shape fluctuations

Since the bending rigidity of lipid bilayer membranes is roughly of the order of the characteristic thermal energy $k_{\mathrm{B}}\mathcal{T}$ its shape is undulated by thermal fluctuations [48, 123]. A relatively simple mathematical description of these undulations can be derived by applying the energy (1.6) to an in average flat membrane assuming zero pressure difference, zero point forces and expanding the mean curvature up to linear order[9] [48]. This approach has been extended for other energy expressions [124–126] and for spherical and more complicated average shapes [127–129]. Also the effects of pressure [130], active fluctuations driven by cytoskeletal motor proteins [54, 131, 132] and the effect of anchoring points to the cytoskeleton [133, 134] have been discussed recently.

The thermally fluctuating membrane has a *persistence length* of [135, 136]

$$\xi_{\mathrm{p}} = l_{\mathrm{mic}}\, e^{\frac{4\pi}{3}\frac{\kappa_{\mathrm{b}}}{k_{\mathrm{B}}\mathcal{T}}}, \tag{1.7}$$

where l_{mic} is a microscopic length, *e.g.*, the thickness of the membrane (see Figure 1.2). With a rigidity $\kappa_{\mathrm{b}} = 20\, k_{\mathrm{B}}\mathcal{T}$ the persistence length becomes $\xi_{\mathrm{p}} \sim 10^{34}\,\mu\mathrm{m}$ and is thus many orders of magnitude larger than the typical circumference of a cell, $\pi R \sim 10\,\mu\mathrm{m}$. Therefore, the membrane shape is determined by a persistent, average *equilibrium shape* (see section 1.3.3), around which the membrane is fluctuating with small undulations [137].

For the average equilibrium shape *effective* parameters can be introduced, in case of the energy (1.6) an effective bending stiffness, an effective surface tension and a projected area. These parameters arise from their *bare* counterparts, associated to the total membrane [132, 135, 136, 138, 139][10]. In general, the relation between effective

---

[9] See explanation on the *weak-bending approximation* in section 1.3.3.

[10] The effective parameters are also called *renormalized* parameters.

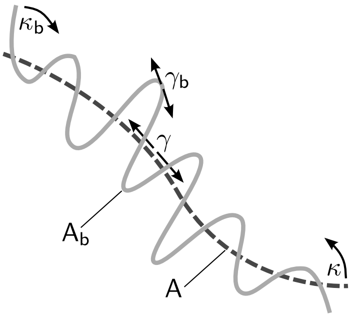

Figure 1.4 | Schematic of a fluctuating membrane. The dark gray dashed line indicates the average equilibrium shape of the membrane with an effective area A, an effective surface tension γ and an effective bending rigidity κ. The light gray solid line marks a snapshot of the dynamic, thermal undulations around the equilibrium shape with the associated bare quantities.

and bare quantities can be stated as

$$A = A(A_\mathrm{b}, \kappa_\mathrm{b}, \gamma_\mathrm{b}), \quad \kappa = \kappa(A_\mathrm{b}, \kappa_\mathrm{b}, \gamma_\mathrm{b}), \quad \gamma = \gamma(A_\mathrm{b}, \kappa_\mathrm{b}, \gamma_\mathrm{b}), \tag{1.8}$$

where the subscript b indicates the bare values and the not subscripted quantities shall be understood as effective quantities from now on. An illustration of the relation between bare and effective quantities is provided in Figure 1.4. Physically the bare quantities are related to subcellular properties, *e.g.*, the total area is approximately proportional to the lipid number, $A_\mathrm{b} \sim N_\mathrm{l}$. The effective quantities, on the other hand, relate to cellular properties. Most analytical derived expressions for (1.8) studied flat membranes, only recently curved geometries have been considered [130].

In this work we assume for the surface tension and the bending rigidity that

$$\kappa \simeq \kappa_\mathrm{b}, \qquad \gamma \simeq \gamma_\mathrm{b}. \tag{1.9}$$

Furthermore, we use an approximate relation between A_b and A, derived for flat membranes [138]:

$$\frac{A_\mathrm{b} - A}{A} \simeq \frac{k_\mathrm{B}\mathcal{T}}{8\pi\kappa} \log\left[\frac{\kappa q_\mathrm{max}^2 + \gamma}{\kappa q_\mathrm{min}^2 + \gamma}\right]. \tag{1.10}$$

Here $q_\mathrm{min} := \pi/l_\mathrm{mem}$ and $q_\mathrm{max} := \pi/l_\mathrm{mic}$ are the minimal and maximal possible fluctuation modes of the membrane, respectively. Whereas the maximal mode is determined by the microscopic length of lipids, $l_{\text{mic}} \sim 5\,\text{nm}$, the minimal mode is set by the characteristic size of the membrane. Equation (1.10) implies that in the limit of maximal confinement of the membrane, when $l_{\text{min}} \simeq l_{\text{max}}$, the fluctuations vanish and, thus, projected and total membrane area coincide, *i.e.*, $A \simeq A_{\text{b}}$.

1.3.3 | Equilibrium shape equations

The *equilibrium shape* of a lipid bilayer membrane, the average shape of the fluctuating membrane, is defined as the shape which minimizes the energy $\mathcal{F}$ and can be found mathematically by the variation of this energy [140][11]. Here the energy (1.6) is given by the effective quantities, introduced in section 1.3.2, and depends via the volume, the surface area and the curvature on the equilibrium shape and only on this. Hence, the energy minimum is uniquely determined by the equilibrium shape.

In order to find the equilibrium shape the variation of the energy, denoted by $\delta\mathcal{F}$, has to vanish. A general parameterization independent *shape equation*, which determines the equilibrium shape, can be derived for the variation of (1.6) [141]. However, in many cases it is more convenient to start from a specific *parameterization*. This uniquely defines the position of the surface in the three-dimensional space and depends only on two independent parameters u and v. The geometrical quantities of the energy (1.6) can then be expressed in terms of the chosen parameterization, as discussed in more detail in appendix A. The variation of the energy leads to a set of bulk and boundary terms, where the latter have to vanish identically, as discussed in appendix B, and the bulk terms give rise to a system of coupled partial differential equations, the so-called *Euler-Lagrange equations*. These equations determine the equilibrium shape upon integration constants which need to be specified by boundary conditions.

---

[11] The variation can also return unstable maximizing shapes, which, however, the system would leave eventually due to thermal fluctuations.

The choice of parameterization is arbitrary because any physical quantity, in particular the energy, must be invariant under coordinate transformations [142]. Therefore, it is convenient to choose the parameterization according to the principal geometrical features of the surfaces. In this work we use two different parameterizations, the *Monge parameterization* and the *arc length parameterization*. For the Monge parameterization, we set the point force f to zero.

Monge parameterization

In the Monge parameterization a height function h is used to describe the position of a surface with respect to a flat reference plane. This reference plane is parameterized by u and v which are chosen here to coincide with the two cartesian coordinates x and y:

$$x = u, \quad y = v, \quad z = h(u, v) \equiv h(x, y). \tag{1.11}$$

The one-dimensional case, where h is a function of x only, is illustrated in Figure 1.5a. The Monge parameterization is only well-defined if the slope of the surface remains finite in any point, *i.e.*, the condition $\arctan \|\nabla_{\|} h\| < \pi/2$ is satisfied. Here $\nabla_{\|}$ is the two-dimensional *nabla operator*. In the context of the *weak-bending approximation*, often this condition is further confined by postulating $\|\nabla_{\|} h\| \ll 1$. This approximation is equivalent to very weak undulations of the surface where $h(x, y)$ is only changing slowly along the reference plane. The surface can then be seen as a relatively flat rectangular

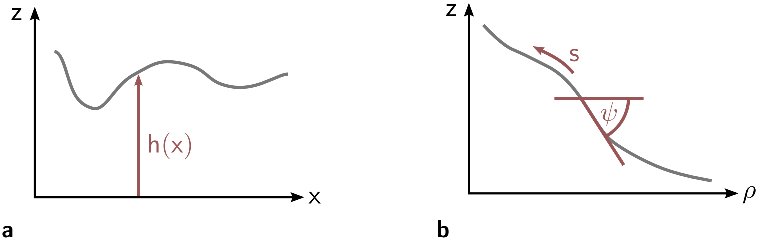

Figure 1.5 | Schematic of two special parameterizations for curves and surfaces. a Monge parameterization; **b** arc length parameterization.

sheet. As discussed in appendix B.2 in detail, the energy expression for such a sheet can be linearized and the corresponding shape equation deduces to

$$\triangle_{\parallel}^{2} h(x,y) - \frac{\gamma^*}{\kappa} \triangle_{\parallel} h(x,y) = \frac{\Delta p}{\kappa} \tag{1.12}$$

with the two-dimensional *Laplace operator* $\triangle_{\parallel}$ and the renormalized surface tension

$$\gamma^* := \gamma + \frac{\kappa}{2} C_0^2. \tag{1.13}$$

The squared Laplace operator is called *biharmonic operator*. The boundary terms, which also occur in the variation calculus, are negligible for our later calculations. The square root of the ratio κ/γ^* defines a *characteristic bending length*

$$\lambda = \sqrt{\frac{\kappa}{\gamma^*}}. \tag{1.14}$$

Since (1.12) is, in principle, solvable with analytical methods, the weak-bending approximation has been used extensively in the past to study various questions regarding the shape of membranes [48, 143–147].

Arc length parameterization

Whereas the Monge parameterization $h(x,y)$ is a convenient choice to describe the shape of rectangular membrane sheets it is inappropriate for membranes with axial symmetry, *i.e.*, where the shape is independent of an arbitrary rotation around the symmetry axis as it is the case, *e.g.*, for ideal membrane tubes [116–118]. A better choice is then a Monge parameterization of the form $z = h(\rho)$, where ρ is the cylindrical radius and h is independent of the second parameter, the polar angle φ[12]. However, this choice has the same disadvantage of a limited height gradient. To overcome this limitation the *arc length parameterization* can be used for axial symmetric membranes. Its independent parameters are the arc length s of the *contour line*, as is illustrated in Figure 1.5b, and the polar angle φ. The coordinate transformation can be written as

$$x = \rho(s)\cos\varphi, \quad y = \rho(s)\sin\varphi, \quad z = h(s). \tag{1.15}$$

In contrast to the Monge parameterization, here the coordinate transformation yet depends on two functions, the cylindrical radius $\rho(s)$ and the height $h(s)$. However, also for the arc length parameterization, a single shape function can be introduced. It is given by the *tilt angle* $\psi(s)$ between the contour tangent and the ρ-axis and is related to $\rho(s)$ and $h(s)$ via

$$\frac{d\rho}{ds} = -\cos\psi, \quad \frac{dh}{ds} = \sin\psi. \tag{1.16}$$

These relations require a modification of the energy (1.6) by two additional Lagrange terms in order to ensure their conservation in the variation calculus. By introducing two Lagrange multipliers $\mu(s)$

---

[12] It is introduced in more detail in appendix B.2 and used in the appendices E.2 and D

and $\nu(s)$ the modified energy $\mathcal{F}^*$ follows as

$$\mathcal{F}^* = \mathcal{F} + \mu\left(\frac{d\rho}{ds} + \cos\psi\right) + \nu\left(\frac{dh}{ds} - \sin\psi\right). \tag{1.17}$$

The variation of (1.17) involves five functionals, namely $\delta\rho$, δh, $\delta\psi$, $\delta\mu$ and $\delta\nu$. A sixth degree of freedom for the equilibrium shape is the overall *contour length* Λ of the surface. As a consequence, also the boundary positions of the contour line, s_1 and s_2, are not fixed and need to be included into the variation [148]. Alternatively, the boundaries can be chosen in such a way that the arc length ranges from $s_1 = 0$ to $s_2 = \Lambda/2$. Then the arc length can be normalized by $\Lambda/2$ and the new parameter u ranges from $u_1 = 0$ to $u_2 = 1$ and Λ enters the energy by the coordinate transformation from s to u. The total contour length Λ is then an additional free parameter in the energy, while the integral boundaries remain constant. Overall, six coupled (differential) equations can be found from energy minimization, as demonstrated in appendix B.3:

$$\begin{aligned}
0 &= -\Delta p\Lambda\rho^2\,\cos\psi - \frac{8\kappa}{\Lambda}\rho\psi_{|uu} + \kappa\Lambda\frac{\sin 2\psi}{\rho} \\
&\quad + \frac{1}{\pi}\left(\left(4\kappa\psi_{|u} - f\Lambda - 2\Lambda\nu\right)\cos\psi - 2\Lambda\mu_{|u}\sin\psi\right), \qquad (1.18)\\
0 &= 2\,\gamma\Lambda + C_0^2\kappa\Lambda + 4C_0\kappa\,\psi_{|u} - 2\Delta p\Lambda\rho\sin\psi \\
&\quad - \kappa\Lambda\frac{\sin^2\psi}{\rho^2} + \frac{4\kappa}{\Lambda}\psi_{|u}^2 - 4\mu_{|u}, \qquad (1.19)\\
0 &= \nu_{|u}, \qquad (1.20)\\
0 &= \frac{\Lambda}{2}\cos\psi + \rho_{|u}, \qquad (1.21)\\
0 &= -\frac{\Lambda}{2}\sin\psi + h_{|u}, \qquad (1.22)\\
0 &= 2\pi\int_0^1 du\left[\rho\left(2\gamma + C_0^2\kappa - \frac{4\kappa}{\Lambda^2}\psi_{|u}^2\right)\right.
\end{aligned}$$

$$
\begin{aligned}
&-2C_0\kappa\sin\psi-\frac{f}{\pi}\sin\psi-\Delta p\rho^2\sin\psi\\
&+\kappa\frac{\sin^2\psi}{\rho}+2\mu\cos\psi-2\nu\sin\psi\Bigg]\,,
\end{aligned}
\tag{1.23}
$$

where the notation $_{|u} := \frac{\partial}{\partial u}$ is used for simplicity. Equations (1.21) and (1.22) ensure the consistency of the variation, as they coincide with the imposed relations (1.16) between ρ and ψ and h and ψ, respectively. Equations (1.19) and (1.20) for μ and ν will serve as constraint conditions for the two actual shape defining quantities, $\psi(u)$ and Λ.

In addition to the shape equations, there are three boundary terms

$$
\left.\frac{\partial\mathcal{L}^*}{\partial\psi_{|u}}\delta\psi\right|_0^1=\left.\frac{\partial\mathcal{L}^*}{\partial\rho_{|u}}\delta\rho\right|_0^1=\left.\frac{\partial\mathcal{L}^*}{\partial h_{|u}}\delta h\right|_0^1\overset{!}{=}0
\tag{1.24}
$$

with

$$
\begin{aligned}
\frac{\partial\mathcal{L}^*}{\partial\psi_{|u}}&=-\kappa\rho\left(\frac{\sin\psi}{\rho}-\psi_{|s}-C_0\right)\,,\\
\frac{\partial\mathcal{L}^*}{\partial\rho_{|u}}&=\mu\,,\quad\frac{\partial\mathcal{L}^*}{\partial h_{|u}}=\nu,
\end{aligned}
\tag{1.25}
$$

and $\mathcal{L}^*$ being the integrand of the energy $\mathcal{F}^*$ (see (B.25) and (B.27) on page 144 and 144). With the help of imposed boundary conditions the boundary terms (1.24) can be evaluated and the shape equations can be solved uniquely.

1.4 | Scope of this thesis

The first quantitative descriptions of cell membranes focused on those aspects where the membrane can be treated as a lipid bilayer without interactions to the underlying cell cortex. Most remarkable are contributions on membrane fluctuations, red blood cell shapes and the principal lateral organization of lipids and membrane proteins, as discussed in the previous sections. However, since novel microscopic techniques not only allow to observe the outer membrane but also the cortex beneath, more recent work started to explore the interaction between cell cortex and membrane. For instance, experiments determined the critical force needed to detach the membrane from the cell cortex [149], resolved the compartmentalized microstructure of the membrane due to the underlying cortex meshwork [13, 64, 150] and studied the biochemical pathways of binding [151]. Theoretical contributions proposed different concepts to account for the membrane-cortex interaction. Coarse-grained approaches introduced an energy expression for the combined membrane-cortex layer [152, 153] or assumed a continuos adhesion energy [70]. Others treated the interaction by ligand-receptor binding kinetics [154] or by anchoring the membrane at spatially localized pinning sites [133, 155–158]. These concepts have been used to describe hindered diffusion and its influence on the formation of ordered lipid microdomains [153, 159–162]. Also the effect on membrane fluctuations has been discussed where both the anchoring itself and also the perturbation induced by active fluctuations inside the cortex are important [133, 134, 157, 158]. The latter has also been identified as the driving mechanism for transversal propagating membrane waves [131, 163].

Another large group of studies focused on mechanisms, triggered by membrane-cortex interactions, which cause the deformation of the cell membrane into local, persistent *out-of-plane structures*[13]. *Blebs* form when the membrane detaches locally from the cortex or the cortex ruptures locally [149, 164–166]. *Microvilli* are induced by actin bundles pushing from the inside against the membrane [167]. *Buds* and *caveolae* are mediated by membrane prote-

---

[13] Here the term *persistent* is used to distinguish these structures from non-persistent fluctuations.

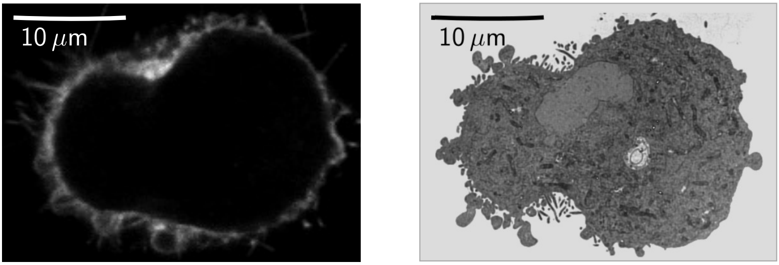

Figure 1.6 | Local membrane deformations during cytokinesis. The images show a L929 mouse fibroblast cell during cytokinesis. The left image has been taken with a confocal microscope, where the intensity is proportional to the membrane marker CAAX. The right image has been taken with an electron microscope (a single slice of the cell). Both give evidence for an accumulation and ruffling of membrane on the smaller cell pole, whereas on the other pole the membrane is rather smooth. [Images provided by Andrea Pereira (left) and Ortrud Wartlick (right), University College London].

ins [119, 168–171]. Local contractions of the cell cortex can stimulate the formation of unmediated collections of buds, *bulges* and *tubes* [155, 172–177].

In this context recent experiments with mouse fibroblast cells during cytokinesis raised our attention. As discussed in section 1.2, under certain conditions their cleavage furrow position can destabilize, resulting in volume oscillations between the two daughter cell poles [26]. Very recently, Andrea Pereira and Ortrud Wartlick from Ewa Paluch's group[14] have provided confocal images of the labeled cell membrane as well as electron microscopy images, both shown in Figure 1.6. Such images indicate that cell pole oscillations also affect the shape of the cell membrane. On the side of the contracting pole the membrane strongly accumulates into small buds, bulges and microvilli, on the expanding side it appears relatively flat.

The finding of these local membrane structures provokes the

---

[14] Medical research Council, Laboratory for Molecular Cell Biology, University College London, UK.

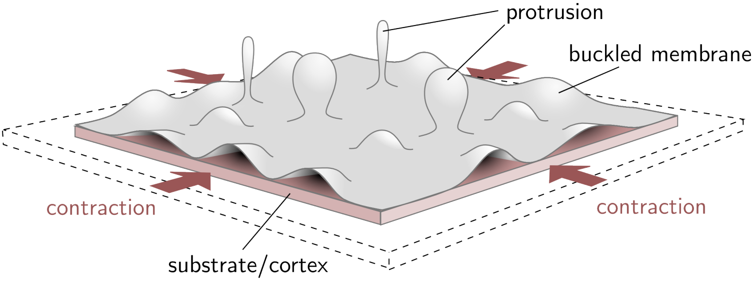

Figure 1.7 | Illustration of membrane buckling induced by lateral compression. When the underlying substrate or cell cortex of the membrane, to which the membrane is attached, contracts or is compressed, the membrane can locally buckle as studied in [155, 175]. The buckling can lead to the formation of different protrusion types, such as buds and tubes [175].

following questions: How can the appearance of these structures, that are rather triggered by forces than by proteins, be understood in a larger cellular context? That is, on the one hand, how exactly does the cortex mechanics influence the membrane? How do cortex contractions induce membrane protrusions, what types, and how is the membrane tension modified then? On the other hand, can the mechanical state of the membrane, in turn, also affect global mechanical properties of the cell, which are assumed to be dictated, to a large extent, by the cell cortex?

Partly, these questions have been addressed previously. An overall cell surface tension, consisting of contributions from both the cortex and the membrane, has been used to determine the mechanical equilibrium of the cell via Laplace's law [154]. The magnitude of the surface tension has been proposed to regulate the ability of a cell to form extrusions, such as blebs and *lamellipodia*, used, *e.g.*, for cell migration [178, 179]. Three other studies are especially related to the experimental observations for dividing cells, discussed above (Figure 1.6): Staykova *et al.* have shown *in vitro* that a lipid bilayer coupled to an underlying elastic substrate responds to a compression of the substrate with a local buckling, *i.e.*, detachment of the membrane from the substrate (see illustration in Figure 1.7) [174, 175]. This buckling is due to the fact that lipid bilayers are effectively incompressible and thus must compensate the lateral compression by storing excess area in out-of-plane structures. As Staykova *et al.* quantified, these structures take the form of bulges and can eventually turn into tubular or spherical protrusions, upon a further compression of the substrate. This finding is remarkable because it demonstrates that the formation of such localized out-of-plane structures does not require the assistance of curvature inducing molecules, as studied previously [180]. Instead a pure mechanical stimulus is sufficient. The idea that forces can induce membrane buckling has also been discussed by Sens *et al.* to describe red blood cell shedding [73, 155]. They apply the concept of force balance to the anchoring points where the cell membrane is attached to the underlying contractile cortex. Above a critical contractility the tightly attached membrane buckles, forms a bulge and may, eventually, vesiculate. Finally, Lenz *et al.* showed that even in absence of contractility an intrinsic curvature of cortex filaments can induce buckling [177].

Although the mentioned investigations made important contributions for the addressed questions, a global cellular description which combines cortex and membrane mechanics and, at the same time, accounts for the formation of membrane microstructures is yet missing. It is the main goal of this thesis to introduce such a description. It shall be simple enough to give analytical insights but also capable to provide interesting physical implications, of which some will be discussed here.

We will begin in chapter 2 with a relatively flat membrane, which is anchored at discrete points to an underlying square lattice, comparable to the previously suggested fence-like structure, induced

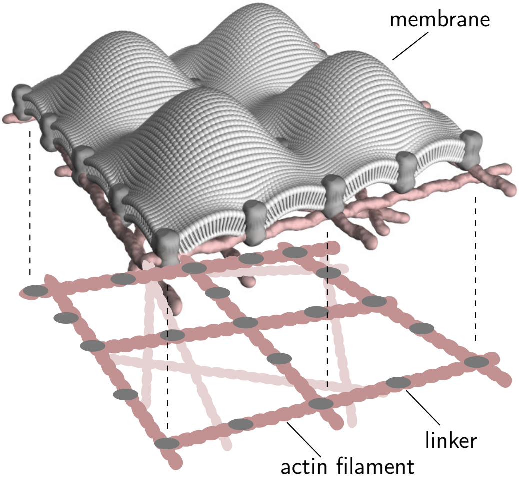

Figure 1.8 | Illustration of an anchored membrane buckled due to available excess area.

by the underlying filamentous cortex meshwork [59, 66]. We will introduce a physical description which allows to calculate analytically the out-of-plane membrane shape, depending on the given excess area (compared to the projected square), a hydrostatic pressure difference across the membrane and the anchoring configuration. An illustration of such a model membrane is shown in Figure 1.8. In chapter 3 we will then assume that the bulge-like structure, occurring in each of these square lattice elements, can roughly be treated as an axisymmetric protrusion and will therewith propose a model membrane setup by a collection of protrusions. This model accounts for more complicated protrusion geometries such as tubes and buds, for which we will study the stability. We will then assume that this model can be used, in good approximation, to describe a cell membrane anchored to the underlying cell cortex. Based on this, we will describe in chapter 4 the outer shell of the cell as a coupled layer of cortex and membrane, from which the membrane surface tension and shape, the pressure difference between cell inside and outside and the cell radius can be determined independently. We will use this description to study the formation of blebs and microvilli in cells, depending on the cortical tension and the external osmotic pressure. Moreover, we will discuss the experimental observations, shown in Figure 1.6, quantitatively. In the last chapter we will conclude our findings and will give a brief outlook of potential future interests.

A MEMBRANE BOUND TO DISCRETE ANCHORING POINTS 2

Summary: As we have discussed in section 1.4, in some situations the cell membrane can be structured into different types of local protrusions. The ability of forming them arises from available *excess area*, which is distributed on a smaller cellular *apparent surface area.* Moreover, the membrane is also constrained by the underlying cell cortex as it is attached to it by linker proteins. This fact motivates the question how this attachment affects the exact structuring of available excess area and if it can trigger particular local out-of-plane shapes.

In this chapter we approach this question by developing a simplified analytical membrane model where a membrane is tightly anchored at discrete points, which are periodically arranged on a flat square lattice[1]. We study the resulting membrane structure, the forces exerted on the anchoring points and the surface tension within the membrane as a function of excess area, pressure difference and the exact arrangement of anchoring points. Based on this, we find that, as soon as anchors are not only placed at the corners of the square lattice but also along the edges, the preferential out-of-plane shape is given by *membrane bulges* with almost axial symmetry, one

---

[1] A related description, based on a different modelling approach, has been suggested previously in [156, 181].

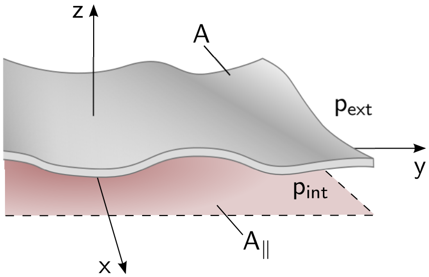

Figure 2.1 | Illustration of a membrane sheet. A is here the total membrane area, $A_{||}$ the area projected in the x-y-plane and $p_{\mathrm{int}} - p_{\mathrm{ext}}$ the pressure difference across the membrane.

bulge located in each of the lattice squares. If the anchors are located in the corners only and the pressure difference is zero, we find, besides the bulge-like pattern, a second *ridge-like* pattern, which exhibits long-range folds.

2.1 | Membrane anchors arranged on a square lattice

Throughout this chapter we regard the lipid bilayer membrane as a thin, infinitely spread sheet with only weak shape undulations as sketched in Figure 2.1. In this limit we can use the Monge parameterization in the weak-bending approximation to describe its elevation h as a function of x and y (see section 1.3.3). Furthermore, we treat the membrane sheet in the constant effective area ensemble where the total number of lipids and, thus, the total area stored in fluctuations A_{b} is undetermined but the average area A is fixed. Since the sheet is infinitely extended along the axes, it is useful to normalize A by the projected area $A_{||}$ underneath the membrane in order to have a finite area measure. The area conservation can then be written as

$$\Omega := \frac{A}{A_{||}} - 1 \overset{!}{=} \mathrm{const.} \tag{2.1}$$

The quantity Ω is a measure for the *excess area* of the membrane sheet in relation to its projected area. Condition (2.1) determines the surface tension γ, which acts as a Lagrange multiplier then. Additionally, a pressure difference $\Delta p = p_{\text{ext}} - p_{\text{int}} > 0$ is applied across the membrane, where p_{int} is below the membrane and p_{ext} above (see Figure 2.2b).

The exertion of a non-vanishing pressure difference Δp on a free membrane sheet would lead to an accelerated shift of the sheet towards the lower pressures. Such a shift is suppressed when the membrane is fixed at discrete *anchoring points*. As then the membrane remains at rest, the force exerted by the pressure difference must be compensated by a *resistive force* provided by these anchoring points. This is illustrated in Figure 2.2b where the anchored membrane is sketched in a side view. At the anchoring points (dark gray) an outward pointing force f_{out} (blue), generated by a larger pressure p_{int} compared to p_{ext}, is balanced by the inward force f_{in} (red).

In principle, any spatial distribution of membrane anchoring points, holding the membrane in position, is conceivable. For simplicity, we study the simplified case where anchoring points are arranged at equal height on a two-dimensional, quadratic, periodic lattice with mesh size ξ, shown in Figure 2.2a. Examples of different unit elements for this lattice are shown in Figure 2.2c. The unit elements are symmetric with respect to the x and y direction and the anchors are placed equidistantly along the edges. Their number is tunable by a parameter q. For $q = 0$ anchoring points are only located at each corner of the lattice. For $q = 1$ one additional intermediate anchor is placed on each edge and for $q = 2$ two. We can formalize the position of the anchors by the function

$$G_{mn;s} = \delta(x - \xi n - x_s)\delta(y - \xi m - y_s) \tag{2.2}$$

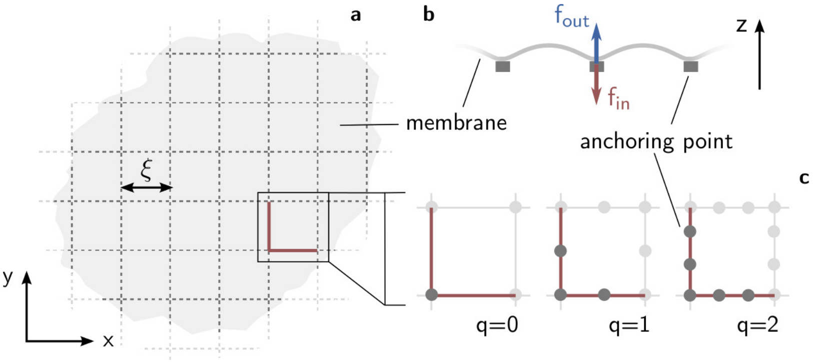

Figure 2.2 | Membrane sheet bound to a square lattice of discrete anchoring points. In **a** a top view with indicated anchoring mesh (dashed lines) of mesh size ξ is shown. **b** provides a side view of the membrane bound by anchors. **c** shows three different examples of unit lattice elements. At each lattice corner one anchoring point is located. Additional anchors can be placed in between along the edges of the lattice. The value q defines the exact number of such intermediate anchors.

with the chosen coordinate representation

$$x_s = \begin{cases} \frac{s}{q-1}\xi & 0 \leq s \leq q, \\ 0 & q < s \leq 2q, \end{cases} \tag{2.3}$$

$$y_s = \begin{cases} 0 & 0 \leq s \leq q, \\ \frac{s-q}{q-1}\xi & q < s \leq 2q. \end{cases} \tag{2.4}$$

Here the indices n and m label the different lattice elements, both running from $-\infty$ to ∞, and s the individual anchors within one unit element, running from 0 to $2q$.

With the help of the function $G_{mn;s}$ we can deduce the shape equation for a membrane sheet constraint by periodically arranged anchors. It is given by (1.12) on page 35 with additional terms arising from the resistive force $f_{\mathrm{a}}^{(s)}$ at the position of the anchors:

$$\triangle_{\parallel}^{2} h(x,y) - \frac{\gamma^{*}}{\kappa}\triangle_{\parallel} h(x,y) = \frac{\Delta p}{\kappa} + \sum_{s=0}^{2q} \frac{f_{\mathrm{a}}^{(s)}}{\kappa\,\xi^{2}} \sum_{n,m} G_{mn;s}. \tag{2.5}$$

The introduced resistive forces are determined by ensuring that all anchoring points remain at the same height, independent of the choice of Δp. We discuss this in more detail in the following section. From symmetry arguments, identical anchors in the neighboring lattice elements must experience the same force. Only the forces within one unit element can differ between the anchors. That is why the forces only carry the index s.

For convenience, we use dimensionless quantities from now on. We first introduce a normalized energy $\overline{\mathcal{F}} := \mathcal{F}/\kappa$. Secondly, with the mesh size ξ we can normalize the coordinates to $\overline{x} := x/\xi$, $\overline{y} := y/\xi$ and $\overline{h} := h/\xi$. Furthermore, we then introduce a normalized pressure difference $\overline{\Delta p}$, normalized anchor forces $\overline{f}_{\mathrm{a}}^{(s)}$, normalized spontaneous curvature $\overline{C}_0$ and normalized surface tension $\overline{\gamma}$ as follows:

$$\overline{\Delta p} := \frac{\xi^3}{\kappa}\Delta p, \quad \overline{f}_{\mathrm{a}}^{(s)} := \frac{\xi}{\kappa} f_{\mathrm{a}}^{(s)}, \quad \overline{C}_0 := \xi\, C_0, \quad \overline{\gamma} := \frac{\xi^2}{\kappa}\gamma. \tag{2.6}$$

Moreover, in Monge parameterization in weak-bending approximation the excess area can be expressed as (see also Table B.1 on page 150)

$$\Omega \equiv \frac{1}{2}\int_0^1 d\overline{x}d\overline{y}\,\overline{\nabla}_{\|}\overline{h}^2. \tag{2.7}$$

2.2 | Solution of the shape equation

Using the weak-bending approximation has the advantage that the resulting shape equation (2.5) can be solved analytically. This can be done by computing the *fundamental solution* $\overline{h}_{\mathrm{f}}$ of (2.5) and construct the solution $\overline{h}$ as the convolution of $\overline{h}_{\mathrm{f}}$ with a *source term* $\overline{Q}$ [182]:

$$\overline{h}(\overline{x},\overline{y}) = (\overline{Q} * \overline{h}_{\mathrm{f}})(\overline{x},\overline{y}). \tag{2.8}$$

As a source term we understand in this context the inhomogeneity of a differential equation. In our case it is given by the right-hand side of (2.5).

The solution (2.8) uniquely describes the boundary value problem with sources up to an arbitrary gauge function $\overline{h}_0$ which satisfies the homogeneous problem

$$\left[\overline{\triangle_{\|}}^2 - \overline{\gamma}^* \overline{\triangle_{\|}}\right] \overline{h}_0(\overline{x}, \overline{y}) = 0. \tag{2.9}$$

Any such $\overline{h}_0$ can be added to the solution $\overline{h}$ without changing its validity [183]. In particular, this includes a constant solution. We make use of this to gauge $h(x, y)$ such that the anchoring points are always located at $z = 0$.

In detail, the derivation of $\overline{h}$, according to (2.8), is explained in appendix C. Here we summarize a few key aspects. First of all, from the construction of the fundamental solution $\overline{h}_\mathrm{f}$ we conclude that the Fourier transform of (2.8) is given by[2]:

$$\hat{\overline{h}}(\overline{k}_x, \overline{k}_y) = \frac{\hat{\overline{Q}}(\overline{k}_x, \overline{k}_y)}{\overline{k}^4 + \overline{\gamma}^* \overline{k}^2}. \tag{2.10}$$

The hatted quantities are those in the Fourier k-space, where $\overline{\mathbf{k}}$ is the normalized wave number vector with the cartesian components $\overline{k}_x$ and $\overline{k}_y$. The sought profile $\overline{h}(\overline{x}, \overline{y})$ can then be calculated by the inverse Fourier transformation of (2.10) if, beforehand, the Fourier transform $\hat{\overline{Q}}(\overline{k}_x, \overline{k}_y)$ can be computed. In case of our shape equation (2.5) this is relatively easy because the Fourier transformation of the source term reduces to the transformation of standard functions. The resulting function $\hat{\overline{Q}}(\overline{k}_x, \overline{k}_y)$ contains δ-distributions only. Two terms are proportional to the zeroth mode δ-distribution $\delta(\overline{k}_x)\delta(\overline{k}_y)$. Each of them would lead to a divergence of the height profile, due to the denominator of (2.10). The reason for this divergence lies in the origin of these two terms. One of them corresponds to the pressure difference $\overline{\Delta p}$, the other to the resistive anchoring forces $\overline{f}_{\mathrm{a}}^{(s)}$. If only one of both would be present, the membrane sheet would be displaced continuously until infinity. Thus, the divergence originates from an unbalanced force exerted on the membrane. However, this effect is eliminated as we introduced the resistive forces such that they exactly balance the pressure difference and the membrane sheet is held in place.

---

[2] The definition of the Fourier transformation, used here, is given by (C.4) and (C.5) on page 154.

The matching of the two zeroth mode terms leads to one defining condition for $\overline{f}_{\mathrm{a}}^{(s)}$. In total $2q+1$ such conditions are needed to uniquely determine all anchoring forces within one unit element. The remaining $2q$ follow from the fact that the anchors are all kept at the same height. All $2q+1$ conditions can be summarized in a matrix equation, which determines all $\overline{f}_{\mathrm{a}}^{(s)}$:

$$\sum_{s=0}^{2q} \overline{M}_{ls}\overline{f}_{\mathrm{a}}^{(s)} = \overline{N}_l, \tag{2.11}$$

where $\overline{M}$ is a square matrix with the entries

$$\overline{M}_{ls} = \begin{cases} 1 & \text{for } l = 0, \\ \overline{\Gamma}_{\overline{\gamma}^*}(\overline{x}_l - \overline{x}_s, \overline{y}_l - \overline{y}_s) & \\ \quad - \overline{\Gamma}_{\overline{\gamma}^*}(\overline{x}_0 - \overline{x}_s, \overline{y}_0 - \overline{y}_s) & \text{otherwise,} \end{cases} \tag{2.12}$$

and $\overline{N}$ a vector with the entries

$$\overline{N}_l = \begin{cases} -\overline{\Delta p} & \text{for } l = 0, \\ 0 & \text{otherwise.} \end{cases} \tag{2.13}$$

The used function $\overline{\Gamma}_\alpha(\overline{x},\overline{y})$ is defined as

$$\begin{aligned}\overline{\Gamma}_\alpha(\overline{x},\overline{y}) :=& \frac{1}{4\pi^4}\sum_{n,m\geq 1}\frac{\cos(2\pi n\overline{x})\cos(2\pi m\overline{y})}{(n^2+m^2)^2+\frac{\alpha}{4\pi^2}(n^2+m^2)}\\ &+\frac{1}{8\pi^4}\sum_{n\geq 1}\frac{\cos(2\pi n\overline{x})+\cos(2\pi n\overline{y})}{n^4+\frac{\alpha}{4\pi^2}n^2}.\end{aligned} \tag{2.14}$$

Also the final height profile of the anchored membrane sheet can be expressed by $\overline{\Gamma}_\alpha$:

$$\overline{h}(\overline{x},\overline{y}) = \sum_{s=0}^{2q}\overline{f}_{\mathrm{a}}^{(s)}\left[\overline{\Gamma}_{\overline{\gamma}^*}(\overline{x}-\overline{x}_s,\overline{y}-\overline{y}_s)-\overline{\Gamma}_{\overline{\gamma}^*}(\overline{x}_s,\overline{y}_s)\right]. \tag{2.15}$$

2.3 | Mechanical properties for constant surface area

2.3.1 | Membrane surface tension

For a membrane sheet with fixed (normalized) surface tension $\overline{\gamma}^*$ (2.15) together with (2.11) would be enough to describe it. However, since we want to study the shape for a fixed effective surface area we have to adjust $\overline{\gamma}^*$ accordingly. This is achieved by plugging $\overline{h}(\overline{x},\overline{y})$ from (2.15) into the area relation (2.7) and solving it for $\overline{\gamma}^*$. In general, this cannot be done with analytical methods. Instead it needs to be solved numerically as we explain in appendix C. For the corresponding solution $\overline{\gamma}^*$ we find that

$$\overline{\gamma}^* = \overline{\gamma}^*(\Omega,\overline{\Delta p}). \tag{2.16}$$

In fact, $\overline{\gamma}^*$ is only a function of one independent parameter, defined by the ratio[3]

$$\beta = \frac{\overline{\Delta p}^2}{\Omega}. \tag{2.17}$$

---

[3] A plot of $\overline{\gamma}^*(\beta)$ is provided in Figure C.3 on page 165.

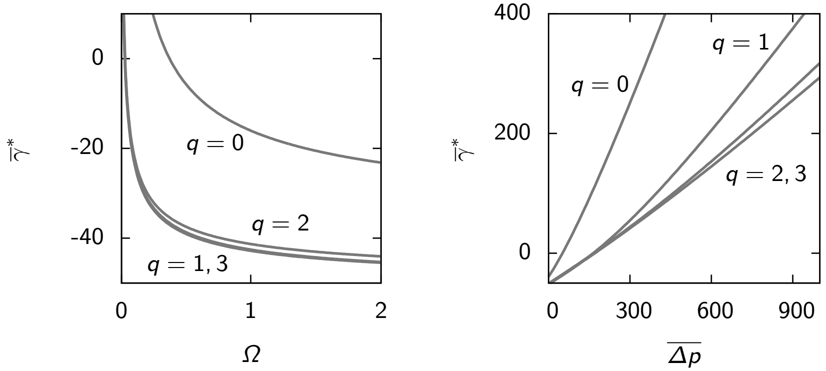

Figure 2.3 | Surface tension of an anchored membrane sheet. Plotted as a function of the excess area with a constant pressure difference $\overline{\Delta p} = 100$ (left), as a function of the pressure difference with a constant excess area $\Omega = 0.1$. Both is plotted for different anchor configurations as indicated.

This ratio shows that pressure and excess area have inverse effects on the surface tension. Increasing the pressure is qualitatively the same as decreasing the excess area. The quantitative dependencies are shown for four different anchor configurations in Figure 2.3. In the limit of a large pressure difference, with a constant finite excess area, $\overline{\gamma}^*$ increases linearly with $\overline{\Delta p}$. More precisely, we find that

$$\overline{\gamma}^* \propto \frac{\overline{r}^*}{\sqrt{\Omega}}\overline{\Delta p} \quad \text{for} \quad \beta \to \infty. \tag{2.18}$$

Here $\overline{r}^*$ is a numerical constant specified in Table 2.1. The limit of large pressure difference is equivalent to the limit of $\Omega \to 0$. In both cases β goes to infinity. Hence, the found approximation (2.18) also describes the divergent behavior of $\overline{\gamma}^*$ near $\Omega = 0$. Qualitatively, this divergence can be understood in the following way: A finite pressure difference will always tend to buckle the membrane sheet. This buckling can only be suppressed by putting the membrane under infinite

Table 2.1 | Numerical values corresponding to the asymptotic behavior of $\overline{\gamma}^*(\Omega, \overline{\Delta p})$. The constants correspond to the following relations: $\overline{\gamma}^* \propto \overline{\gamma}_0^* + \overline{r}_0^* \overline{\Delta p}/\sqrt{\Omega}$ ($\beta \to 0$), $\overline{\gamma}^* \propto \overline{r}^* \overline{\Delta p}/\sqrt{\Omega}$ ($\beta \to \infty$) and $\overline{\gamma}^*(\beta_0) = 0$. The constants are obtained analytically and their precision is determined by the expansion order of the height profile $\overline{h}$ (see appendix C).

q	β_0 $[10^5]$	$\overline{\gamma}_0^*$	${\overline{r}_0^*}^{-2}$	${\overline{r}^*}^{-2}$
0	0.264	$-4\pi^2$	$2\pi^2$	5.64
1	2.71	−51.8	124	22.1
2	2.78	−50.7	114	38.0
3	2.91	−52.0	112	45.1

positive tension. On the other hand, for $\overline{\Delta p} \to 0$ the surface tension always becomes negative, as it also does for increasing Ω, until it, eventually, reaches a minimal negative value $\overline{\gamma}_0^*$, provided in Table 2.1. In principle, the occurrence of a negative surface tension can be understood by the curvature caused by excess area. More excess area is equivalent to more curvature and is energetically less favorable according to our energy ansatz. Hence, if possible, the membrane would exclude lipids in order to reduce its curvature and, thus, the energy. This tendency gives rise to a negative surface tension where the lipids have to resist a squeezing. In fact, this mechanism can also explain why the surface tension is always significantly lower for $q > 0$ compared to $q = 0$. At $\overline{\Delta p} = 0$ the enhanced constraining of the shape, due to more anchors, leads to a larger curvature of the membrane sheet. This leads, according to our previous arguments, to a lower surface tension. Secondly, more anchors damp the impact of the pressure difference on the membrane shape. That is why $\overline{\gamma}^*$ also increases more slowly for $q > 0$. Both aspects can be concluded

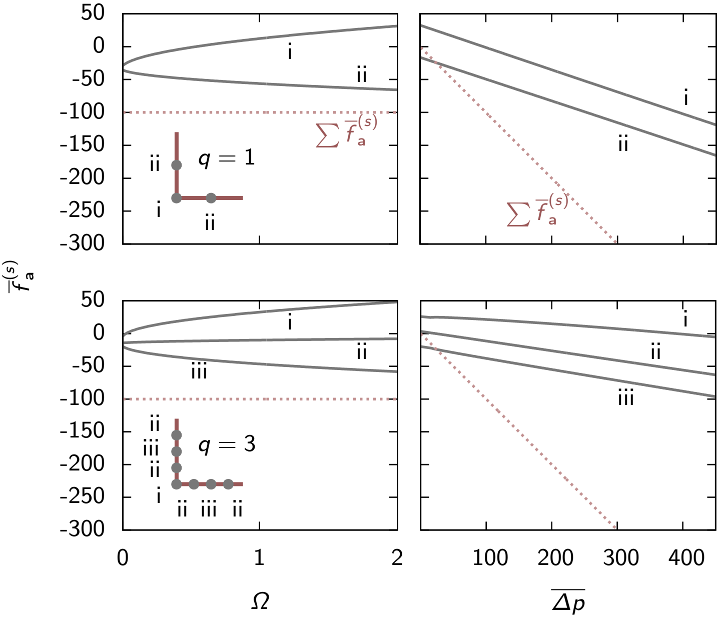

Figure 2.4 | **Resistive forces at the membrane anchoring points.** Plotted are two examples for the configurations $q = 1$ (top) and $q = 3$ (bottom). For varying area (left) a constant pressure difference $\overline{\Delta p} = 100$ is used and for varying pressure difference (right) a constant area $\Omega = 0.5$ is used. The inset schematics give an orientation for the position of the respective anchor. The dashed line indicates the total anchoring force, which has to be equal to $-\overline{\Delta p}$.

from the energy $\overline{\mathcal{F}}$ of one unit element of the membrane sheet, shown in Figure C.2b on page 162. At $\overline{\Delta p} = 0$, where $\overline{\mathcal{F}}$ coincides with the curvature energy $\overline{\mathcal{F}}_C$, $\overline{\mathcal{F}}$ is larger for $q > 0$ than for $q = 0$, indicating the larger curvature. And for $\overline{\Delta p} > 0$ it changes more slowly, indicating the effect of pressure on the shape is weaker.

2.3.2 | Anchoring forces

Having the surface tension $\overline{\gamma}^*$ we can compute the force $\overline{f}_{\mathrm{a}}^{(s)}$ via (2.11). The result is shown for two example configurations at $q = 1$ and $q = 3$ as a function of Ω and $\overline{\Delta p}$ in Figure 2.4. The two most important observations are these: Firstly, although (2.11) implies that $\sum_s \overline{f}_{\mathrm{a}}^{(s)} = \overline{\Delta p}$, each individual force $\overline{f}_{\mathrm{a}}^{(s)}$ does not converge necessarily to zero for $\overline{\Delta p} \to 0$. This is only the case if also $\Omega \to 0$ (not shown in Figure 2.5). That is, also the curvature of the membrane sheet, due to the excess area, feedbacks to the anchoring points. This means that the anchors do not only prevent the membrane from detachment due to pressure difference but also from invagination. This finding is related to the second important observation, namely that $\overline{f}_{\mathrm{a}}^{(s)}$ can take both values smaller and larger than zero. The case $\overline{f}_{\mathrm{a}}^{(s)} < 0$ corresponds to a membrane *pulling* on the anchors, $\overline{f}_{\mathrm{a}}^{(s)} > 0$ to an inward *pushing*. Thus, curvature and pressure difference affect the sign of the forces similarly as this of the surface tension. Increasing $\overline{\Delta p}$ at constant Ω leads, eventually, to a pulling force at all anchoring points (Figure 2.4 right). A larger excess area can reduce this pressure induced pulling at some anchoring points so that the force direction is inverted (see, *e.g.*, Figure 2.4 left, anchor i). In general, the pressure difference seems to have a larger impact on the middlemost anchors, the curvature on those closer located to the corners of the lattice. To check the consistency of these observations, we also plotted in Figure 2.4 the sum of all forces (red dashed line), which is found to be equal to $-\overline{\Delta p}$ for all values of Ω and $\overline{\Delta p}$, as required.

2.4 | Equilibrium shapes for constant surface area

Based on the found expression for $\overline{h}(\overline{x}, \overline{y})$ in (2.15) and the computed surface tension $\overline{\gamma}^*(\Omega, \overline{\Delta p})$ from the previous section, we now

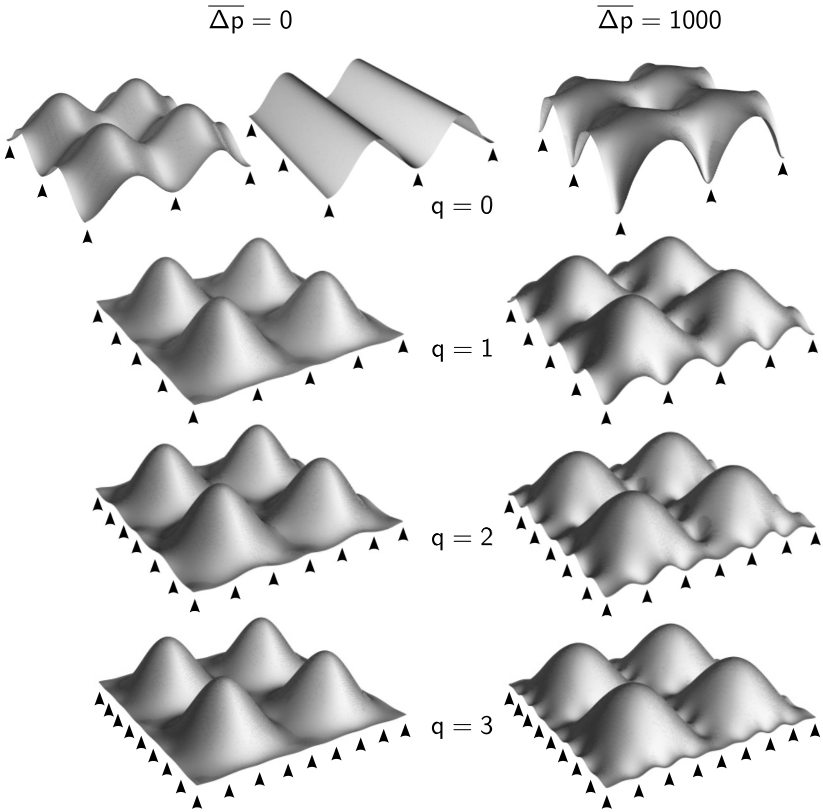

Figure 2.5 | Equilibrium shapes of a membrane sheet anchored to a square lattice of discrete anchoring points. Shown are four neighboring elements of the periodic lattice. The area is in all cases $\Omega = 0.5$. The two columns correspond to two different pressure differences as indicated and the four rows to different anchor configurations as introduced in Figure 2.2. The anchor positions are indicated by small arrows. For the case $\overline{\Delta p} = 0$ and $q = 0$ (left upper corner) two distinct solutions are possible (see text for explanation).

study the equilibrium shape of the periodically anchored membrane sheet with a fixed surface area, which shall be in excess compared to the underlying basal plane. Some examples are plotted in Figure 2.5. Chosen are the four anchor configurations $q = 0$, $q = 1$, $q = 2$

and $q = 3$ at $\overline{\Delta p} = 0$ and $\overline{\Delta p} = 1000$. One of the main observations from these shapes is that the addition of intermediate anchoring points along the lattice edges ($q > 0$) leads, as one would expect intuitively, to the formation of separate membrane *bulges* in each unit element, with almost axial symmetry[4]. Interestingly, the exact number of intermediate anchors seems not to matter much for the principal formation, already for $q = 1$ the shape changes significantly and is for larger q only slightly modified further. This agrees with the previous results for the surface tension which mainly changes from $q = 0$ to $q = 1$. This characteristic change becomes especially visible for low pressure difference (Figure 2.5 left) where the shapes for $q > 0$ look nearly identical as the membrane lies almost flat on top of the lattice edges and the symmetry of the bulges is almost axial in all three cases, *i.e.*, each bulge can be rotated around an axis going through the center of the lattice square with changing the overall shape only marginally. In contrast, for large pressure differences (Figure 2.5 right) the discrete anchoring is rather pronounced and the different configurations are still distinguishable.

2.4.1 | The limit of zero pressure difference and corner anchors only

It is interesting to take a closer look at the case $q = 0$ and $\overline{\Delta p} = 0$. We find that in this limit the equilibrium shape can be described by the simple, sinusoidal expression

$$\overline{h}(\overline{x}, \overline{y}) = \frac{1}{\pi}\sqrt{\frac{\Omega}{2}}\left[2 - \cos\left(2\pi\overline{x}\right) - \cos\left(2\pi\overline{y}\right)\right]. \tag{2.19}$$

How this can be concluded from the solution (2.15) is explained at the very end of appendix C. However, it is also straight forward to verify (2.19) with the help of the homogenous shape equation (2.9), for which (2.19) is a solution.

---

[4] In fact, in the limit $q \to \infty$ we expect our results to be comparable to those reported in [184] for a single bulge bound to a quadratic frame.

In fact, the solution (2.19) is only one of a whole set of sinusoidal solutions of the form $\overline{h}_0 \sim \cos(\overline{\mathbf{k}} \cdot \overline{\mathbf{r}})$ with the condition

$$\|\overline{\mathbf{k}}\| = \begin{cases} \sqrt{|\overline{\gamma}^*|} & \overline{\gamma}^* < 0, \\ 0 & \text{otherwise} \end{cases} \tag{2.20}$$

for the absolute value of the wave number vector $\overline{\mathbf{k}}$. The second case corresponds to the trivial solution $\overline{h}_0 = \text{const.}$ On the other hand, the first case can be chosen for $\overline{\gamma}^* = -4\pi^2$ (as found for $q = 0$ and $\overline{\Delta p} = 0$) such that

$$\overline{h} + \overline{h}_0 = \frac{\sqrt{\Omega}}{\pi} \left[1 - \cos(2\pi \overline{x}_i)\right], \tag{2.21}$$

where $\overline{x}_i$ is either $\overline{x}$ or $\overline{y}$. As mentioned earlier, any homogeneous solution can be added to the special solution $\overline{h}$ so that (2.21) represents another possible solution, besides (2.19), for the equilibrium shape of an anchored membrane sheet. In contrast to bulge-like solutions, this out-of-plane shape corresponds to membrane *ridges*. Interestingly, both solutions (2.19) and (2.21) take exactly the same energy value $\overline{\mathcal{F}} = 4\pi^2\Omega$. This means that both are equivalently favorable solutions for the anchor configuration $q = 0$ at zero pressure difference. That is why both solutions are shown in Figure 2.5 (top left)[5]. For all other configurations ridges can not be expected as solutions with minimal energy, based on our calculations (see appendix C for details). This can be understood by the fact that the membrane pattern for $q > 0$ is rather characterized by periodically repeated bulges instead of sinusoidal functions.

---

[5] A previous theoretical work predicted the transition between membrane bulges and ridges due to non-zero local spontaneous curvature [147].

A MEMBRANE AS A COLLECTION OF PROTRUSIONS

3

Summary: In the previous chapter we developed a simple analytical model to describe the shape of a membrane sheet which is discretely anchored on a periodic square lattice. An important outcome of this study was that a membrane with excess area will form bulges with almost axial symmetry if it is anchored along the edges of the lattice. This finding agrees with several experimental observations, discussed in chapter 1, where small membrane structures with almost axial symmetry were found. These *protrusions* can not only take the form of bulges but also of buds, tubes and blebs.

Since these protrusion shapes exceed, in general, the weak-bending approximation, used for our previous analytical description, we introduce in this chapter another membrane model. Again, we define a periodic square lattice as the underlying planar structure. However, now the membrane is attached entirely along the lattice edges and each unit lattice element is occupied by an axisymmetric protrusion. The suggested picture allows a two-step modeling of the anchored membrane: First, we study the shape and mechanical properties of an isolated axisymmetric membrane protrusion. Second, we couple the protrusions by allowing a lipid exchange until their surface tensions are equilibrated. Based on this equilibrium condition, we find stability diagrams for the distribution of excess area

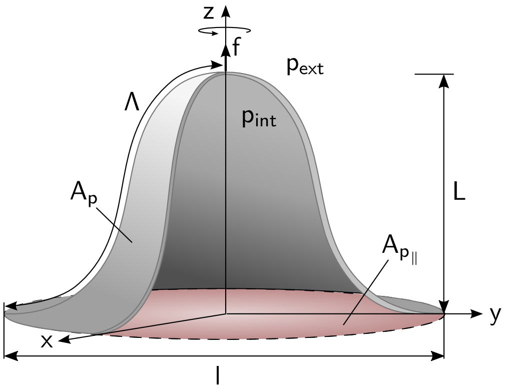

Figure 3.1 | Illustration of a membrane protrusion with axial symmetry. A_p is here the membrane area of the protrusion, $A_{p_{||}}$ the basal projection, Λ the contour length, L the elongation in z-direction and $p_{int} - p_{ext}$ the pressure difference across the membrane.

among the protrusions, determined by the two parameters excess area and pressure difference. In the stable state excess area is distributed homogeneously among the protrusions, in the unstable state one protrusion gains excess area while the others lose it, resulting in the formation of a bleb. We study this for both protrusions with and without a point force perturbation and extend our findings to an analytical description of a membrane with only partial force perturbation. For this case we find a shape diagram which predicts a possible coexistence of unperturbed bulges and elongated tubes.

3.1 | Shape equations for axisymmetric membrane protrusions

A schematic of a membrane protrusion as considered here is shown in Figure 3.1. It has *axial symmetry* with respect to the z-axis. Hence, the two-dimensional surface can uniquely be described by the one-dimensional curve of the *contour line*, which can be parameterized by its arc length, as introduced in section 1.3.3. Furthermore, a pressure difference $\Delta p = p_{\text{int}} - p_{\text{ext}} > 0$ across the membrane of the protrusion is taken into account, equivalently to this introduced in chapter 2.

Also the effective protrusion surface area is assumed to be constant again so that the condition

$$\int dA_{\mathrm{p}} \equiv A_{\mathrm{p}} \overset{!}{=} \text{const.} \tag{3.1}$$

determines the surface tension. New in this chapter is the addition of a constant point force f, which is exerted on the tip of the protrusion.

The protrusion boundary is located at a radius $\rho = l/2$ and a height $z = 0$, and the transition to the adjacent membrane shall be smooth, *i.e.*, the tangent along the borderline is parallel to the x-y-plane. From this a number of constraint conditions for the functions $\rho(u)$, $h(u)$ and $\psi(u)$ of the arc length parameterization follow. The radius $\rho(u)$ is fixed at both ends of the contour line and takes the values $l/2$ at $u = 0$ and 0 at $u = 1$, respectively. The height $h(u)$ is only fixed at one end, namely at the border of the protrusion at $u = 0$. The other end at $u = 1$ remains free. That is why the elongation in z-direction of the protrusion is *ex ante* unknown and results from the calculated equilibrium shape. The angle $\psi(u)$ has to be zero at both ends to prevent the formation of kinks in the overall membrane shape. All together this leads to five boundary conditions:

$$\begin{gathered} \rho(0) = l/2, \quad \rho(1) = 0, \\ h(0) = 0, \\ \psi(0) = 0, \quad \psi(1) = 0\,. \end{gathered} \tag{3.2}$$

In fact, the freedom of the protrusion elongation gives rise to a sixth condition, originating from the boundary terms (1.24) on page 38 of the variation. Five of them vanish immediately due to (3.2), since $\delta\rho(0) = \delta\rho(1) = 0$, $\delta h(0) = 0$ and $\delta\psi(0) = \delta\psi(1) = 0$. Only $\delta h(1)$ does not vanish. We can then conclude from (1.24) and (1.25) on page 38 that

$$\nu(1) = 0. \tag{3.3}$$

The shape equations in the arc length parameterization (1.18) – (1.23) on page 37 lead to six integration constants in total. Hence, they are fully determined by the six boundary conditions (3.2) and (3.3). We describe in appendix B.3 how the shape equations can then be simplified and rewritten in the following form:

$$\rho(u) = \frac{l}{2} - \frac{\Lambda}{2}\int_0^u du' \cos\psi(u'), \tag{3.4}$$

$$h(u) = \frac{\Lambda}{2}\int_0^u du' \sin\psi(u'), \tag{3.5}$$

and

$$0 = f_\psi^{(1)} + \gamma f_\psi^{(2)} + \mu_0 f_\psi^{(3)}, \tag{3.6}$$

$$0 = f_\Lambda^{(1)} + \gamma f_\Lambda^{(2)} + \mu_0 f_\Lambda^{(3)} \tag{3.7}$$

with

$$\begin{aligned}
f_\psi^{(1)} =& \frac{1}{4}\Bigg(\frac{(4\pi\kappa\psi_{|u} - f\Lambda)}{\pi}\cos\psi - \Delta p\Lambda\rho^2\cos\psi \\
& \quad -\frac{8\kappa}{\Lambda}\rho\,\psi_{|uu} + \kappa\Lambda\frac{\sin 2\psi}{\rho} - 2\Lambda\mu_{\text{int}}\sin\psi\Bigg), \\
f_\psi^{(2)} =& -\frac{1}{4}\Lambda^2 u\sin\psi, \\
f_\psi^{(3)} =& -\frac{1}{2}\Lambda\sin\psi, \\
f_\Lambda^{(1)} =& \frac{1}{2}\int_0^1 du\,\Bigg[C_0^2\kappa\rho + \frac{(2\pi C_0\kappa - f)}{\pi}\sin\psi - \Delta p\rho^2\sin\psi \\
& \quad -\frac{4\kappa}{\Lambda^2}\rho\psi_{|u}^2 + \kappa\frac{\sin^2\psi}{\rho} + 2\mu_{\text{int}}\cos\psi\Bigg],
\end{aligned}$$

$$
\begin{aligned}
f_\Lambda^{(2)} &= \int_0^1 du \left[\rho + \frac{\Lambda}{2} u \cos\psi\right], \\
f_\Lambda^{(3)} &= \int_0^1 du \cos\psi,
\end{aligned}
\tag{3.8}
$$

and

$$
\begin{aligned}
\mu_{\text{int}}(u) = \frac{1}{4}\int_0^u du' \Big[& C_0\kappa\left(4\psi_{|u'} + \Lambda C_0\right) - 2\Delta p \Lambda \rho \sin\psi \\
& -\kappa\Lambda\frac{\sin^2\psi}{\rho^2} + \frac{4\kappa}{\Lambda}\psi_{|u'}^2 \Big].
\end{aligned}
\tag{3.9}
$$

The surface tension γ and the remaining integration constant μ_0 are determined by the conditions

$$A_{\text{p}} = \pi\Lambda \int_0^1 du\, \rho(u), \tag{3.10}$$

$$l = \Lambda \int_0^1 du \cos\psi(u). \tag{3.11}$$

Whereas the second condition arises from the boundary conditions (3.2), the first only applies if, as we assume, the protrusion area is conserved.

As in chapter 2, we use normalized quantities in the following. The basal protrusion diameter l adopts the role of the previously used mesh size ξ. Then the normalized pressure difference $\overline{\Delta p}$, normalized point force $\overline{f}$, normalized spontaneous curvature $\overline{C}_0$ and normalized surface tension $\overline{\gamma}$ read as:

$$\overline{\Delta p} := \frac{l^3}{\kappa}\Delta p, \quad \overline{f} := \frac{l}{\kappa} f, \quad \overline{C}_0 := l\, C_0, \quad \overline{\gamma} := \frac{l^2}{\kappa}\gamma. \tag{3.12}$$

Furthermore, we replace the area A_{p} by the excess area Ω_{p} which states how much more membrane area is available than needed to cover the basal protrusion area $A_{\mathrm{p}_\|}$:

$$\Omega_{\mathrm{p}} := \frac{A_{\mathrm{p}}}{A_{\mathrm{p}_\|}} - 1 = \frac{4}{\pi l^2} A_{\mathrm{p}} - 1. \tag{3.13}$$

Also the energy and volume are normalized accordingly: $\overline{\mathcal{F}} := 4\mathcal{F}/\pi\kappa$, $\overline{V}_{\mathrm{p}} := 4V_{\mathrm{p}}/\pi l^3$. However, this does not affect the shape equations and the resulting equilibrium shape.

3.2 | Equilibrium shapes for constant surface area

The three shape equations (3.4), (3.6) and (3.7) are coupled with each other through the radius ρ, the angle ψ and the contour length Λ. Furthermore, they are subject to the constraint conditions (3.10) and (3.11). In general, it is necessary to use numerical techniques to solve these equations for the equilibrium shape. In this work we use a modified version of the *steepest descent method* to find such numerical solutions [185]. The principle of this method is to start with an initial guess ψ_{initial} and Λ_{initial} so that the boundary conditions (3.2) and the constraints (3.10) and (3.11) are satisfied. *A priori* this guess will not fulfill the shape equations. The non-vanishing right-hand sides of the shape equations can then be interpreted as forces exerted on the shape and can be used for a dynamic ansatz which evolves $\psi(t)$ and $\Lambda(t)$ until all forces vanish and the shape converges towards a stable equilibrium solution. Further details on the numerical procedure are discussed in appendix D.

3.2.1 | Equilibrium shapes for zero pressure difference

A few characteristic protrusion shapes, which we obtain numerically for zero point force, $\overline{f} = 0$, are shown in Figure 3.2. At zero pressure

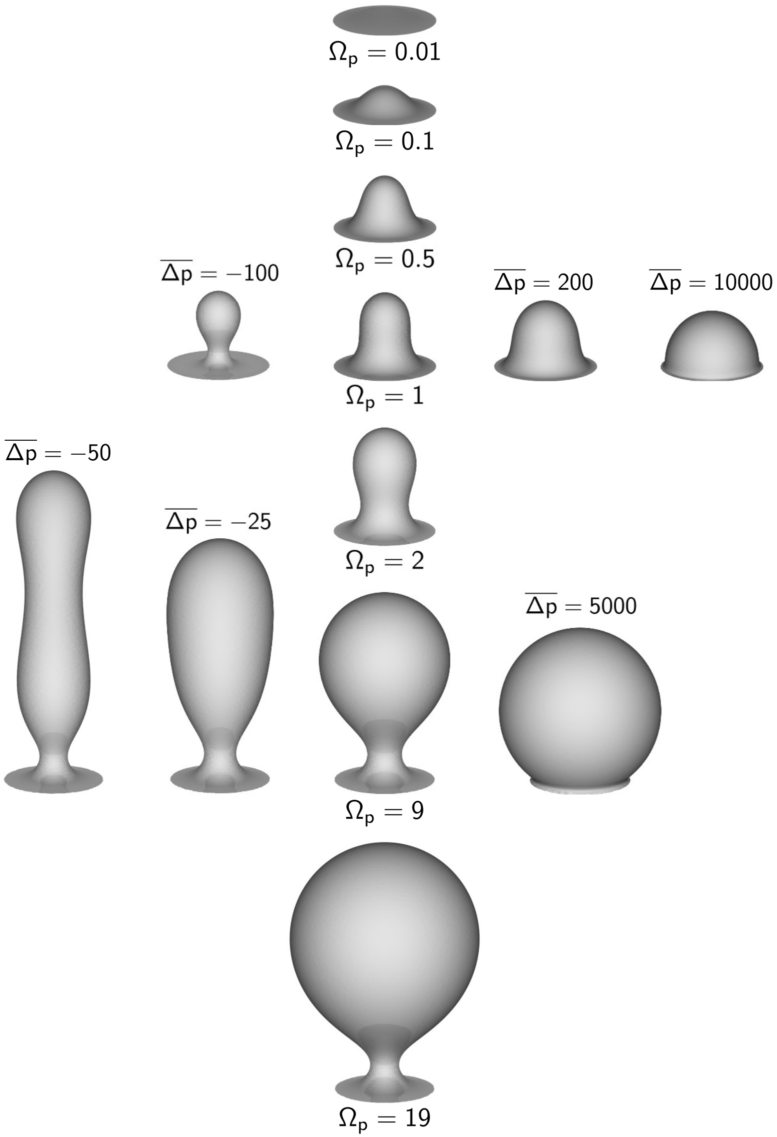
$\Omega_p = 0.01$
$\Omega_p = 0.1$
$\Omega_p = 0.5$
$\overline{\Delta p} = -100$
$\overline{\Delta p} = 200$
$\overline{\Delta p} = 10000$
$\Omega_p = 1$
$\overline{\Delta p} = -50$
$\overline{\Delta p} = -25$
$\Omega_p = 2$
$\overline{\Delta p} = 5000$
$\Omega_p = 9$
$\Omega_p = 19$

Figure 3.2 | **Equilibrium shapes of a membrane protrusion.** Plotted are the shapes, obtained numerically, for different excess areas Ω_p and normalized pressure differences $\overline{\Delta p}$ (middle column $\overline{\Delta p} = 0$). The spontaneous curvature $\overline{C}_0$ and point force $\overline{f}$ are zero. The used spatial resolution for the calculation is $\Delta u = 0.01$.

difference and for $\Omega_\mathrm{p} \to 0$ the protrusion shape approaches a flat disc with normalized diameter 1. When the excess area is increased the disc bulges out and the protrusion forms a bulge-like shape with the slope of the contour line being everywhere below an angle of $\pi/2$. Up to $\Omega_\mathrm{p} \approx 1$ also the Monge parameterization could be used but above it would break down because the slope of the contour line reaches an angle of $\pi/2$ and exceeds it for even larger excess areas where the bulge turns into a bud with a thin neck at the bottom ($\Omega_\mathrm{p} \geq 9$)[1]. Whether these equilibrium shapes correspond to a local or global minimum of the energy $\overline{\mathcal{F}}$ cannot be determined rigorously here. However, from consistency arguments we can deduce indirectly that they should correspond to global minima. This is because besides the flat disc at $\Omega_\mathrm{p} = 0$ and $\overline{\Delta p} = 0$ there is clearly no other solution so that it must be a global minimum of the energy. On the other hand, the buckled shapes for larger excess areas are presumably the simplest shapes with the smallest curvature emerging from the disc and should that is why also be associated to a global minimum.

3.2.2 | Equilibrium shapes for inflating pressure differences

For zero pressure difference the orientation of the protrusion, pointing parallel or antiparallel to the z-axis, is arbitrary. Therefore, at a given excess area, there are always two identical, symmetric solutions. However, if $\overline{\Delta p}$ becomes non-zero, this symmetry is broken so that two distinct classes of solutions occur. One class is given by protrusions which point upwards, parallel to the z-axis. As we chose $\overline{\Delta p} > 0$ those protrusions are *inflated.* The inflation triggers for increasing pressure differences the rounding of the shape towards spherical caps. This is shown for two example excess areas on the right-hand side of Figure 3.2. At $\Omega_\mathrm{p} = 1$ the situation is particularly special as the initial bud-like shape at $\overline{\Delta p} = 0$ becomes almost hemispherical for large pressure differences. This is because a spherical cap at $\Omega_\mathrm{p} = 1$ is exactly a hemisphere. That the shapes become spherical for large pressure differences is owed the fact that then the pressure term in the energy (1.6) dominates the others, in particular the bending term. This pressure term is, in turn, associated to Laplace's law and favors spherical shapes. This can be shown in the limit of a negligible bending rigidity, $\kappa = 0$, where the equilibrium solutions are exactly spherical caps (see appendix E.2) [147].

---

[1] The presented shapes are in good agreement with budded shapes, calculated similarly, in previous works [119, 170, 172, 186, 187].

3.2.3 | Equilibrium shapes for compressing pressure differences

The other class of solutions for non-vanishing pressure differences is downward pointing and is subject to a *compression*, *i.e.*, the surrounding pressure is larger than the inner. We can model this, for instance, by flipping the z-axis and assuming a negative pressure difference. Three results, obtained in this manner, are shown on the left-hand side of Figure 3.2. Contrarily to the previous class of solutions here two different characteristic states exist. First, for $\Omega_\mathrm{p} \gtrsim 1$ the neck of the protrusion is further squeezed so the bulge-like shape at $\Delta p = 0$ turns into a budded shape (Figure 3.2 for $\Omega_\mathrm{p} = 1$ and $\overline{\Delta p} = -100$). Above $\Omega_\mathrm{p} \gtrsim 3.5$ these buds turn into compressed waisted tubes (Figure 3.2 for $\Omega_\mathrm{p} = 9$ and from $\overline{\Delta p} = -25$ to $\overline{\Delta p} = -50$), where the occurring waists are due to the *pearling instability* [117,188,189]. The transition from compressed buds to tubes has been described recently in more detail in [175].

We find another interesting transition for compressed protrusions by studying their stability for an increasing pressure difference. In principle, compressed and inflated protrusions at a given excess area can coexist. The inflated shape has, however, always the lower

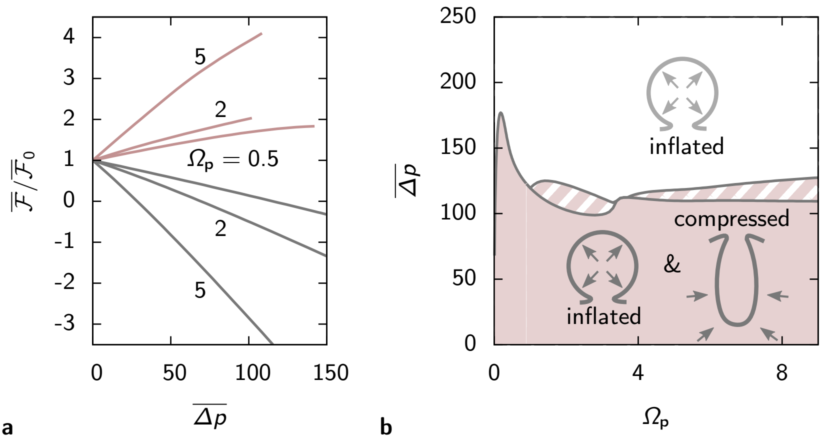

Figure 3.3 | Stability of compressed membrane protrusions. a shows the energy $\overline{\mathcal{F}}$ of inflated (gray) and compressed (red) membrane protrusions for three different excess areas as a function of the pressure difference $\overline{\Delta p}$, $\overline{\mathcal{F}}_0 = \overline{\mathcal{F}}(\overline{\Delta p} = 0)$. The energy for compressed potrusions is plotted up to the critical pressure difference shown in **b** as a function of the excess area. Above the critical pressure only inflated membrane protrusions exist. Below also compressed protrusions are possible. The hatched region indicates where our numerical simulation fails to give an exact prediction. The used spatial resolution is $\Delta u = 0.01$ for **a** and $\Delta u = 0.005$ for **b**. $\overline{C}_0 = 0$ and $\overline{f} = 0$.

energy state as shown in Figure 3.3a. That is, the compressed protrusions only correspond to a local energy minimum. We find that above a critical pressure difference, plotted in Figure 3.3b, this minimum disappears and the compressed solution becomes unstable. Starting from $\Omega_p \approx 0$ increasing the excess area also increases the critical pressure difference, before it decreases to an approximately constant value, meaning that compressed bulge-like shapes seem to be most stable with respect to the applied pressure.

The stability line in Figure 3.3b is obtained by increasing the negative pressure difference in our numerical calculation, starting from zero. At the critical pressure difference the compressed protrusion inverts to an inflated solution with opposite z-directionality[2]. However, above $\Omega_\mathrm{p} \approx 0.9$ the inversion process becomes numerically difficult so that in an intermediate pressure regime (hatched region in Figure 3.3b) no exact prediction can be made.

3.2.4 | Equilibrium shapes for an additional point force at the protrusion tip

For the following parts of this work we restrict our considerations to inflated protrusions. For these we now allow non-vanishing external point forces, $\overline{f} > 0$, which are exerted at the protrusion tip. This leads to an elongation of the protrusion in z-direction, as shown in Figure 3.4a for a protrusion with three different applied point forces. For relatively small loads the initially bud-like shape ($\overline{f} = 0$) establishes a cusp. For large enough loads it turns, eventually, into a thin membrane tube. This transformation can be studied more quantitatively, shown in Figure 3.4b, by plotting the elongation $\overline{L}$ of the protrusion tip as a function of the point force. Interestingly, the transition exhibits a characteristic inflection point where the first derivative of $\overline{L}(\overline{f})$ is maximal and can even become discontinuous above a certain pressure difference (see inset in Figure 3.4b). As we define all shapes above the inflection point as tubes, we can summarize the transition as a function of $\overline{f}$, $\overline{\Delta p}$ and Ω_p in three shape diagrams, shown in Figure 3.4c. A third region accounts there for the discontinuous transition where, in general, buds with a cusp and tubes can coexist[3]. The found shape diagrams will become import-

---

[2] To avoid confusions, it shall be mentioned that the two discussed protrusion classes behave antisymmetricely with respect to the sign of the pressure difference. For $\overline{\Delta p} > 0$ the upward pointing protrusion is inflated, for $\overline{\Delta p} < 0$ the downward pointing is inflated, both being identical apart from the orientation.

[3] Within the coexisting region tubes have a lower energy in close proximity to the pure tube region, further away buds are energetically preferential.

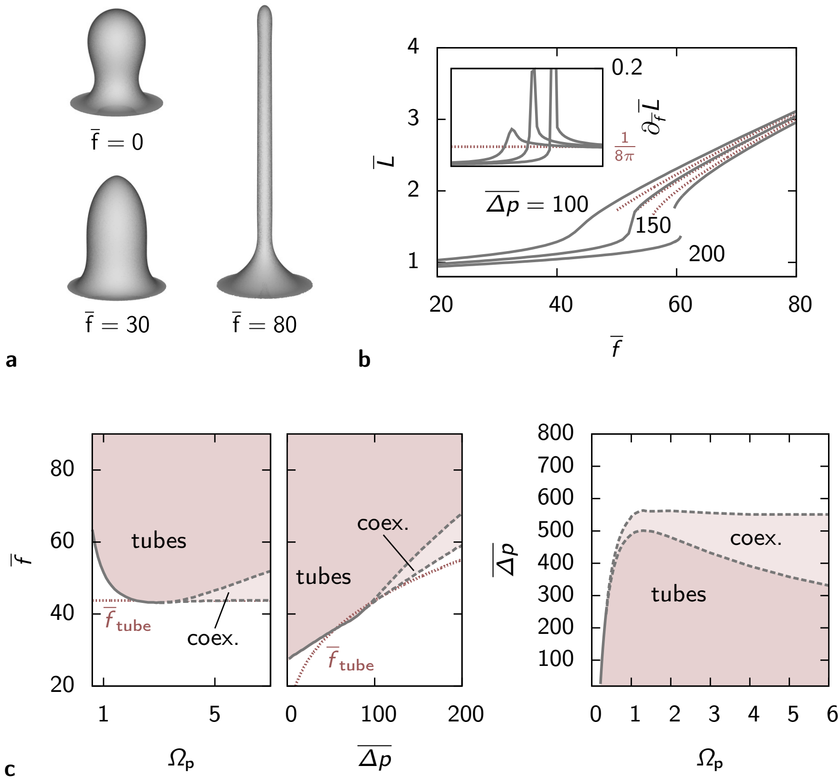

Figure 3.4 | **Formation of membrane tubes. a** shows three examples of equilibrium shapes of a membrane protrusion with different point forces applied at the tip of the protrusion. The excess area ($\Omega_p = 2$) and pressure difference ($\overline{\Delta p} = 100$) are identical for all three cases, moreover, $\bar{C}_0 = 0$ and $\Delta u = 0.005$ (numerical parameter). In **b** the change of the elongation $\bar{L}$ of the same protrusion as in **a** is plotted as a function of the point force $\bar{f}$ for three different pressure differences as indicated. The inset shows the first derivative of $\bar{L}$ with respect to $\bar{f}$. **c** emphasizes the parameter ranges where the applied point force leads to the formation of tubes (red shaded region). This is determined by the position of the inflection point in **b** (see text). The transition can either be continuous (solid line) or discontinuous (dashed line), associated with a coexistence region (light red shaded region). In the two left figures the point force is plotted over the excess area ($\overline{\Delta p} = 100$) and pressure difference ($\Omega_p = 4$), respectively, in the right plot the point force is kept constant at $\bar{f} = 100$. The red dotted lines indicate the analytical approximation in (3.14) and (3.15).

ant again in section 3.5 where we discuss the stability of protrusion collections.

The formation of tubes has already been studied previously both by experiments and theory and for both a discontinuous transition was found [116, 190]. However, in the previous description, which intended to describe isolated tethers pulled out of the membrane rather than many tubes pushed by cortical filaments, the tube was treated for constant surface tension and vanishing pressure difference. This seems to lead to two main differences compared to our findings where the tube area is constant and the pressure difference is non-zero. First, in our case the formation of tubes is not always discontinuous and, in particular, for $\overline{\Delta p} \to 0$ it is continuous. Second, after the tube has formed the force is not constant but increases linearly with further elongation (Figure 3.4b).

Some of these findings can be verified by a simple analytical model which extends the idea of treating a membrane tube as a thin cylinder [191] for non-vanishing pressure difference and constant tube area. We discuss the details in appendix E.3 where we find for the tube elongation

$$\overline{L} \simeq \frac{\Omega_\mathrm{p}}{48\pi} \frac{\overline{f}_\mathrm{tube}\sqrt{\overline{f}_\mathrm{tube}/\overline{f}}}{\sin\left[\frac{1}{3}\arcsin\sqrt{\left(\overline{f}_\mathrm{tube}/\overline{f}\right)^3}\right]} \tag{3.14}$$

with

$$\overline{f}_\mathrm{tube} = 3\pi\sqrt[3]{\overline{\Delta p}}\,. \tag{3.15}$$

This result does not cover all quantitative features of our numerical results, as is indicated by the red dashed lines in Figure 3.4b and (3.4c). However, it agrees qualitatively in some important aspects.

For instance, the leading order asymptotic behavior

$$\overline{L} \propto \frac{\Omega_{\mathrm{p}}}{16\pi}\overline{f} \quad \text{for} \quad f \to \infty \tag{3.16}$$

coincides for large forces. Furthermore, also (3.14) exhibits a pressure-dependent characteristic tube transition as it is only valid for $\overline{f} > \overline{f}_{\mathrm{tube}}$ and this does not depend on the excess area, what is also true for the numerical solution when the coexisting region is considered for tubes and $\Omega_{\mathrm{p}} > 1$.

3.3 | Mechanical properties for constant surface area

3.3.1 | Membrane surface tension

The protrusion shapes discussed in the previous sections were computed for a constant surface area. The surface tension acts then as a Lagrange multiplier, ensuring the area conservation. It is determined via the constraint conditions (3.10) and (3.11). As these are enclosed in the numerical calculation, described in appendix D, the surface tension is also a numerical result, shown for some example parameter sets in Figure 3.5. For zero pressure difference the surface tension starts at a negative value $\overline{\gamma} = 4\left(\min J_1^{-1}(0)\right)^2$ for $\Omega_{\mathrm{p}} = 0$, where $J_\alpha^{-1}(0)$ denotes the roots of the Bessel function of the first kind. This value can be obtained by comparison with an analytical description of a membrane protrusion, as discussed in appendices D and E.1. For increasing excess area the surface tension also increases and approaches $\overline{\gamma} = 0$ for $\Omega_{\mathrm{p}} \to \infty$. In case of a non-zero pressure difference the surface tension starts from infinity at $\Omega_{\mathrm{p}} = 0$ and goes to infinity for $\Omega_{\mathrm{p}} \to \infty$. In between it becomes minimal. The position of the minimum depends on $\overline{\Delta p}$ and approaches $\Omega_{\mathrm{p}} = 1$ for $\overline{\Delta p} \to \infty$. In addition, $\overline{\gamma}$ is proportional to $\overline{\Delta p}$ in this limit. More

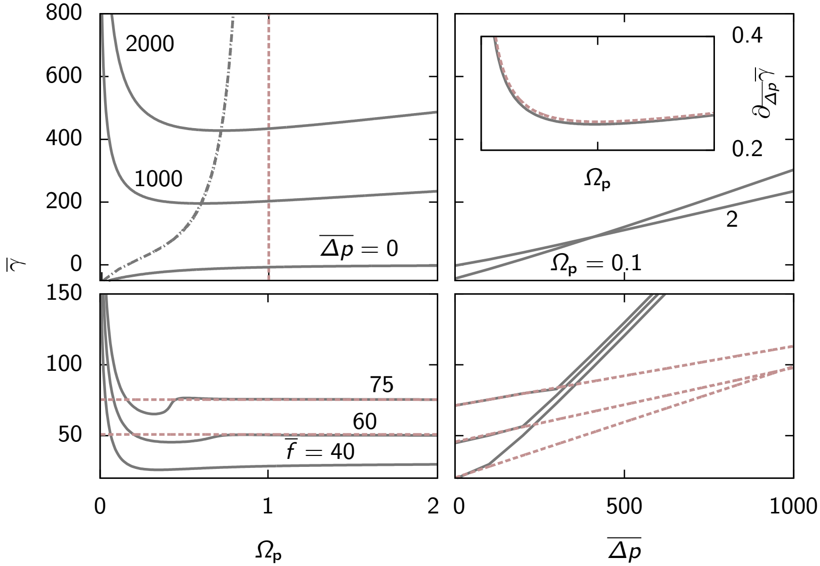

Figure 3.5 | Surface tension of a membrane protrusion. The normalized surface tension $\overline{\gamma}$ is plotted as a function of the excess area for three different pressure differences at $\overline{f} = 0$ (top left), for three different point forces at $\overline{\Delta p} = 100$ (bottom left) and as a function of the pressure difference for two different excess areas (top right) and three different point forces (bottom right). The left and right plots have identical values for $\overline{f}$. The dashed-dotted line (top left) marks the excess area where the surface tension is minimal. The inset (top right) shows the derivative $\partial_{\overline{\Delta p}}\overline{\gamma}$ in the asymptotic limit of a large pressure difference as a function of the excess area (scaling as on the left side). Asymptotic analytical results (see text) are shown by red dashed lines. The schematic in the upper left plot indicates the directionality of the surface tension. The remaining parameters are $\overline{C_0} = 0$ and $\Delta u = 0.01$.

precisely, we find

$$\overline{\gamma} \propto \underbrace{\frac{\Omega_p + 1}{8\sqrt{\Omega_p}}}_{\overline{r}/2} \overline{\Delta p} \quad \text{for} \quad \overline{\Delta p} \to \infty, \tag{3.17}$$

where the proportionality factor $\overline{r}$ is the normalized radius of a spherical cap (see appendix E.2). This agrees with our previous finding that membrane protrusions without point force perturbation converge to spherical caps for $\overline{\Delta p} \to \infty$.

If we allow a point force larger than zero, the surface tension changes significantly as soon as the protrusion enters, continuously or discontinuously, the tube region in Figure 3.4c. In this region it is weakly decaying to a constant value, independent of the excess area. This value can also be estimated analytically, here by the perviously used approximation of a thin cylinder (see appendix E.3). In this limit the value of the constant surface tension is also independent of the excess area and, in leading order, also of the pressure difference. The next smaller term includes a linear pressure dependency (see also (E.29) and (E.32) on page 190):

$$\overline{\gamma} \propto \frac{\overline{f}^2}{8\pi^2} + \frac{\pi\overline{\Delta p}}{\overline{f}} \quad \text{for} \quad \overline{f} \to \infty. \tag{3.18}$$

3.3.2 | Lateral membrane tension

For the later application to cells in chapter 4, besides the membrane surface tension, a second membrane tension is important, the *lateral membrane tension* $\overline{\gamma}_{||}$. It acts within the projected plane underneath the protrusion. To emphasize the difference to the surface tension, a schematic in Figure 3.5 (upper left plot) illustrates where $\overline{\gamma}$ applies and two schematics in Figure 3.6 (right plot) where $\overline{\gamma}_{||}$ applies. Formally, the lateral tension can be defined as (here without normalization)

$$\gamma_{||} := \frac{d\mathcal{F}}{dA_{\mathrm{p}_{||}}}. \tag{3.19}$$

In order to avoid the computational costs of integrating the energy terms and differentiating them afterwards, another explicit expres-

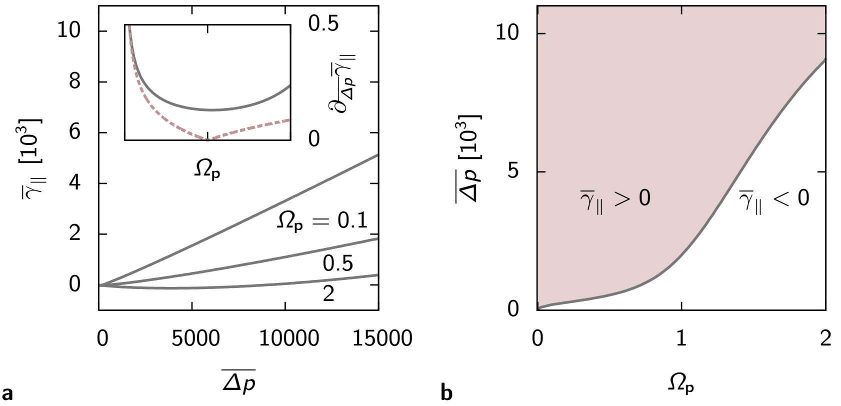

Figure 3.6 | Lateral tension of a membrane protrusion. The normalized lateral tension $\overline{\gamma}_{\|}$ is plotted as a function of the pressure difference for three different excess areas (left), its sign as a function of excess area and pressure difference (right). The inset plot shows the derivative $\partial_{\overline{\Delta p}}\overline{\gamma}_{\|}$ in the asymptotic limit of a large pressure difference as a function of the excess area (scaling as in **b**). The red dashed line indicates the analytical result in (3.22). The schematics in the right plot indicate the tension direction, depending on its sign. $\overline{C_0} = 0$ and $\Delta u = 0.01$.

sion can be deduced [192][4]:

$$\overline{\gamma}_{\|} = \left[\overline{\gamma} - \frac{1}{2}(2\overline{H}^2 - \overline{C}_0^2)\right]_{\rho=\frac{l}{2}} . \tag{3.20}$$

With (3.20) we can compute the lateral tension from the knowledge of $\overline{\gamma}$ and the equilibrium shape, contained in the mean curvature $\overline{H}$. The result is shown for three different excess areas, zero point force and as a function of the pressure difference in Figure 3.6 (left). As the surface tension, also the lateral tension is proportional to the pressure difference for $\overline{f} = 0$ and $\overline{\Delta p} \to \infty$. However, here the proportionality factor $\overline{r}_{\|}$ can only be expressed analytically by the spherical cap limit if $A_\mathrm{p} \to 1$, as can be seen in the inset of the left plot in Figure 3.6. Hence, we can conclude

---

[4] The derivation for a membrane protrusion can be found in appendix F.

$$\overline{\gamma}_\parallel \propto \frac{\overline{r}_\parallel}{2}\,\overline{\Delta p} \quad \text{for} \quad \overline{\Delta p} \to \infty \tag{3.21}$$

with

$$\overline{r}_\parallel = \underbrace{\overline{r}\cos\psi}_{\overline{r}-\overline{h}} = \frac{|1-\Omega_\mathrm{p}|}{4\sqrt{\Omega_\mathrm{p}}} \quad \text{for} \quad \Omega_\mathrm{p} \to 0. \tag{3.22}$$

Here ψ is the contact angle of the spherical cap to the underlying plane (see Figure E.2 on page 187) and $\overline{h}$ is the normalized height of the spherical cap. For $\Omega_\mathrm{p} = 1$ the analytical expression (3.22) results in zero lateral tension since the spherical cap becomes a hemisphere and no surface tension is projected into the basal plane. However, the full numerical solution still has a non-zero contribution, which arises from the second curvature related term in (3.20).

The right plot in Figure 3.6 shows the sign of $\overline{\gamma}_\parallel$, relevant for the superposition with other basal tensions such as the contractile tension of the cell cortex. In the red shaded region, where $\overline{\gamma}_\parallel > 0$, the lateral membrane tension leads to an contractile contribution, in the other, where $\overline{\gamma}_\parallel < 0$, to an expansile contribution. On the one hand, contractility is induced by an increase of the pressure difference and is dominated by surface tension, according to (3.20). On the other hand, expansibility is induced by excess area and dominated by bending rigidity.

For an applied point force $\overline{f} > 0$, $\overline{\gamma}_\parallel$ behaves qualitatively as $\overline{\gamma}$ (not shown here). Most importantly, it also undergoes a transition, continuous or discontinuous depending on the applied force, to a constant value, independent of the excess area. This can be explained by the fact that in addition to the surface tension also the tube radius is independent of the excess area (see (E.32) on page 190). Hence, also the mean curvature in (3.20) is approximately constant and therefore $\overline{\gamma}_\parallel$.

3.3.3 | Vertical protrusion force

Besides the tension $\overline{\gamma}_{\|}$, which acts laterally to the boundary line, an additional force is acting vertically in z-direction, perpendicular to the boundary line. It is initiated by the pressure difference and the applied point force $\overline{f}$ at the protrusion tip. Both would trigger a displacement of the protrusion in z-direction if it would not be fixed at the boundary. The force contribution from the pressure difference is given by the product of Δp with the area projected in the x-y-plane, facing towards the pressure difference. We can expect that this area is equivalent to the basal protrusion area $A_{\mathrm{p}_{\|}}$ (see Figure 3.1). This can be proven by computing

$$\int dA\, \mathbf{n} \cdot \mathbf{e}_z = \pi \rho^2 \Big|_0^{l/2} \equiv A_{\mathrm{p}_{\|}}. \tag{3.23}$$

Hence, the total vertical force along the circular boundary line reads as

$$\overline{f}_{\perp} := \overline{f} + \frac{\pi}{4} \overline{\Delta p}. \tag{3.24}$$

3.4 | Combining protrusions to a membrane

In chapter 2 we found that a membrane anchored along a square lattice forms nearly axisymmetric out-of-plane protrusions in each lattice element if excess area is available. This supports a membrane description, introduced earlier by Sens *et al.* [155], where the membrane is structured by a collection of disc-like patches, which can buckle into spherical caps. We extend this concept by using our more accurate results for membrane protrusions, including non-vanishing pressure differences and point-forces applied at the protrusion tips. Again, as introduced in chapter 2, we structure the membrane by a square lattice with identical unit elements, as sketched in Figu-

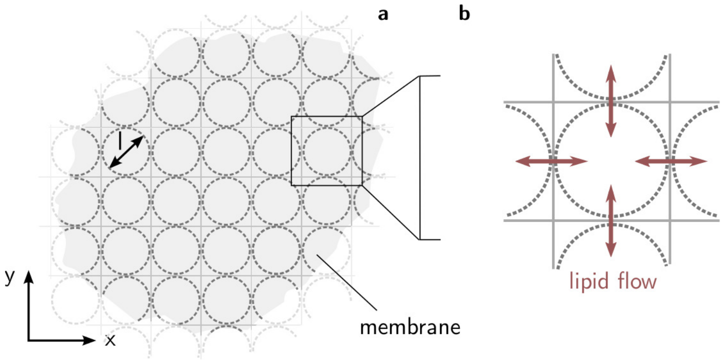

Figure 3.7 | Membrane structured as a collection of protrusions. a Top view of the membrane with one protrusion located in each element of a square lattice. The protrusions are anchored along a circle with diameter *l* (dashed lines). **b** magnifies one element of the lattice and its neighbors. It indicates the lipid flow between neighboring protrusions, which occurs when their surface tensions differ (see (3.27)).

re 3.7a. Each unit element hosts one axisymmetric protrusion with diameter l. Along the circumference the protrusion is tightly anchored to the underlying plane (dashed circles in Figure 3.7a), where this circular binding is the approximation of the actual binding along the square lattice. Locally, we characterize each protrusion by an area $A_{\mathrm{p}_{nm}}$, a point force f_{nm} and, in principle, also a spontaneous curvature $C_{0_{nm}}$ which we, however, set to zero here. The used indices n and m label the unit elements in x and y directions. Global membrane properties, that all protrusions share, are the pressure difference Δp, the bending rigidity κ and the surface tension γ [5]. Furthermore, the total area of the membrane can be written as

$$A = \sum_{n,m} \left[A_{\mathrm{p}_{nm}} + l^2 \left(1 - \frac{\pi}{4}\right)\right] \approx \sum_{n,m} A_{\mathrm{p}_{nm}} \tag{3.25}$$

---

[5] Whereas Δp can, indeed, be seen as a *global* quantity, κ could, in principle, be introduced *locally* for each protrusion to account, *e.g.*, for inhomogeneities in the lateral membrane composition.

or in case of $A \to \infty$ for an infinitely spread membrane (see for comparison (2.1) on page 46) the finite excess area

$$\Omega := \frac{A}{A_{\|}} - 1 = \frac{\pi}{4}\langle\Omega_{\mathrm{p}}\rangle \approx \langle\Omega_{\mathrm{p}}\rangle. \tag{3.26}$$

Here $A_{\|} = \sum l^2$ and $\langle\Omega_{\mathrm{p}}\rangle$ is the average excess area per protrusion. The approximations in (3.25) and (3.26), which we will use in the following, neglect contributions to the area coming from the corners of the square lattice which are not covered by the protrusion base[6].

3.4.1 | Flow equation for the lipid exchange between protrusions

In order to describe the equilibrium state of a membrane, made by a collection of protrusions, we assume that the lipid diffusion within one unit element is significantly faster than between different unit elements. One potential explanation for this could be the hop diffusion, reported previously (see section 1.1.2) [59, 66]. Then the equilibrium shape of a single protrusion is reached almost instantaneously compared to the global equilibrium shape of the membrane. Therefore, we can treat each protrusion at a given time point during the global equilibration *quasi-statically*, *i.e.*, as it would have a constant surface area $\Omega_{\mathrm{p}_{nm}}$ with an associated surface tension, as discussed in section 3.3.1. However, since we regard the surface tension as a global quantity of the membrane, only certain area values are possible. If we assume an initial non-equilibrium area distribution among the protrusions, this can lead to local differences in surface tensions. These differences, in turn, induce a lipid flow from regions with lower surface tensions to regions with larger surface tensions and, thereby, trigger an equilibration of the surface tension[7]. We describe this equilibration by the following linear dynamic ansatz:

---

[6] Choosing a hexagonal instead of a square lattice would further reduce the error made by neglecting the non-covered regions.

$$\frac{\alpha}{\langle \Omega_{\mathrm{p}} \rangle} \frac{d}{dt} \Omega_{\mathrm{p}_{nm}} = \sum_{i,k} \overline{\gamma}(\Omega_{\mathrm{p}_{nm}}) - \overline{\gamma}(\Omega_{\mathrm{p}_{n+i\,m+k}}), \tag{3.27}$$

where α is a friction coefficient and the summation runs over all neighbors of the lattice element at position n, m.

With the numerical results for $\overline{\gamma}$ from section 3.3.1, equation (3.27) forms a set of differential equations for the area distribution $\Omega_{\mathrm{p}_{nm}}$, which can be solved numerically. Starting from any non-equilibrium configuration, the limit $t \to \infty$ determines the equilibrium distribution. In the following work, we will always start from a *homogeneous* distribution, equivalently to the description in chapter 2, where each protrusion carries the same area $A_{\mathrm{p}_{nm}} = A_{\mathrm{p}}$ and $\langle \Omega_{\mathrm{p}} \rangle = \Omega_{\mathrm{p}} = \Omega$, respectively. This initial configuration is immediately an equilibrium state because the surface tension is *a priori* identical everywhere. Its value is determined by the pressure difference and the excess area. An example of such a membrane configuration with $\Omega = 0.2$ and $\overline{\Delta p} = 200$ is shown in Figure 3.8a[8].

3.5 | Equilibrium area distribution between coupled protrusions

If we start from an initially homogeneous area distribution, as described in the previous section, and add a small perturbation to the area of one protrusion, we find with (3.27) two different characteri-

---

[7] Strictly speaking, the flow of lipids is determined by the bare surface tension γ_{b}, introduced in section 1.3.2, for which we assumed here $\gamma_{\mathrm{b}} \simeq \gamma$. However, even without this assumption the flow is presumably determined by γ as fluctuations renormalize all effective tensions in the same way.

[8] For the numerical realization of (3.27) we use periodic boundary conditions.

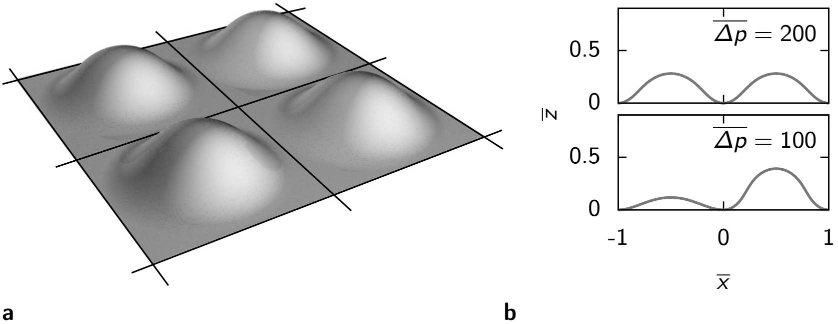

Figure 3.8 | Equilibrium shapes of coupled membrane protrusions. a shows one possible equilibrium shape of four neighboring protrusions, arranged on a square lattice and coupled via (3.27). The excess area is $\Omega = 0.2$ and the pressure difference $\overline{\Delta p} = 200$. **b** shows the equilibrium height profile for two protrusions with an average excess area $\langle \Omega_\mathrm{p} \rangle = 0.2$ and two different pressure differences $\overline{\Delta p}$. $\overline{C}_0 = 0$, $\Delta u = 0.01$.

stic equilibrium states when we keep the excess area constant but change the pressure difference. The symmetric homogeneous equilibrium state switches below a certain pressure difference to an asymmetric equilibrium state, *i.e.*, one protrusion assembles more area than the others (see example with two protrusions in Figure 3.8b). This suggests that, depending on the chosen parameters Ω and $\overline{\Delta p}$, the homogeneous state can, in fact, become an *unstable* equilibrium.

To understand this behavior more quantitatively, we study the linear stability of (3.27). We do this by using the fact that the right-hand side of (3.27) is equivalent to the discrete form of the Laplace operator (see appendix D and [185]), where the discretization step is given by the mesh size $\xi \equiv l$. Hence, we can write (3.27) approximately as

$$\alpha \frac{d}{dt} \Omega_{\mathrm{p}_{nm}} \approx -\overline{\triangle}_{\parallel} \overline{\gamma}(\Omega_{\mathrm{p}_{nm}}). \tag{3.28}$$

We then expand (3.28), including $\overline{\gamma}(\Omega_{\mathrm{p}_{nm}})$, around the homogeneous state $\Omega_{\mathrm{p}_{nm}} = \Omega_{\mathrm{p}} = \Omega$ what leads to a simple diffusion equation:

$$\frac{d\Omega}{dt} = D\overline{\triangle}_{\parallel}\,\Omega \quad \text{with} \quad D = -\frac{1}{\alpha}\frac{\partial\overline{\gamma}}{\partial\Omega}. \tag{3.29}$$

The area distribution among the protrusions is then defined by the sign of the diffusion constant D. For $D > 0$ the diffusion triggers a *spreading* so that the area is kept distributed homogeneously. $D < 0$ has the inverse effect, which leads to the observed instability. As the sign of D is defined by the sign of the derivative of $\overline{\gamma}$ with respect to Ω, we can conclude that

$$\frac{\partial\overline{\gamma}}{\partial A\Omega} < 0 \quad \Leftrightarrow \quad \text{homogeneous state stable.} \tag{3.30}$$

This finding implies that minima in $\overline{\gamma}(\Omega)$ separate stable from unstable homogeneous states. The surface tension of membrane protrusions and, hence, of a membrane made by those contain such minima, as discussed in section 3.3.1. That is why we can deduce from this surface tension stability diagrams depending on Ω, $\overline{\Delta p}$ and $\overline{f}$ [9]. Interestingly, the surface tension for the anchored membrane sheet in weak-bending approximation from chapter 2 does not exhibit such minima in the area dependency. Instead, its surface tension is always decaying monotonously in Ω and thus a homogeneous area distribution is always stable. In order to understand the reason for this significant difference between the two models we calculate in appendix E.1 the surface tension of an axisymmetric protrusion in the weak-bending approximation. We find that also in this case no minima occur, implying that the difference is not due to the different modeling of the anchoring but caused by the weak-bending approximation. We verify this in appendix D where we show that the weak-

---

[9] We do not include the effect of spontaneous curvature here, however, our model can account for it.

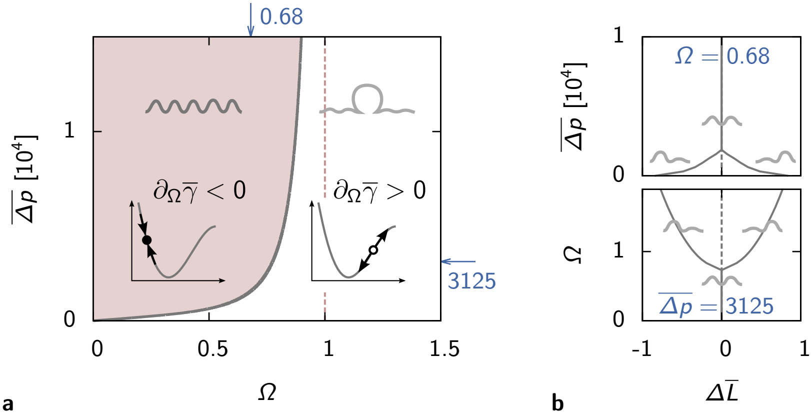

Figure 3.9 | Stability of a homogeneous excess area distribution for a collection of protrusions. **a** shows the stability of a homogeneous area distribution among membrane protrusions as a function of membrane excess area Ω and normalized pressure difference $\overline{\Delta p}$. The red shaded area corresponds to stable configurations. The inset plots show schematically the surface tension $\overline{\gamma}$ as a function of the area and the characteristic position of a stable and unstable point (see text). The red dashed line indicates the transition position for spherical caps, used as an analytical reference. **b** shows the transition from a homogeneous area distribution to a inhomogeneous distribution for two coupled protrusions (see also Figure 3.8b). As a measure for the equality the difference of tip elongations $\Delta \overline{L}$ is used. In the upper plot the transition line is crossed at constant Ω for changing $\overline{\Delta p}$, in the lower plot at constant $\overline{\Delta p}$ for changing Ω. Their positions within the stability diagram are indicated by blue arrows in **a**. $\overline{C}_0 = 0$, $\Delta u = 0.01$.

bending approximation, in fact, misses nonlinear terms important for the calculation of the surface tension.

3.5.1 | Equilibrium area distribution without force perturbations

For zero point force but variable excess area and pressure difference the surface tension of a protrusion collection contains one minimum in Ω (see Figure 3.5). The position of this minimum depends on $\overline{\Delta p}$ so that we can find a transition line $\overline{\Delta p}(\Omega)$ which gives rise to a stability diagram for a homogeneous area distribution shown in Figure 3.9a. The stable region, where excess area remains distributed homogeneously, widens with increasing pressure difference and shrinks with increasing excess area. The maximal excess area, for which a stable homogeneous distribution is still possible, can be found in the limit $\overline{\Delta p} \to \infty$ and is $\Omega = 1$. Above this value the homogeneous distribution is always unstable, independent of the pressure difference. This can be interpreted by the previously used spherical cap approximation, since at $\Omega = 1$ the surface tension of caps becomes minimal (see (3.17)). Furthermore, it can easily be shown that above this value a second asymmetric solution for the area distribution between caps occurs. This asymmetric solution agrees with our observation in Figure 3.8b for the full shape solution. In Figure 3.9b we quantify the transition between symmetric and asymmetric state by plotting the elongation difference between two protrusions for either varying Ω or $\overline{\Delta p}$. We find that the transition corresponds to a *supercritical pitchfork bifurcation* [193].

For more than two protrusions, located in the unstable region of Figure 3.9a, an initially homogeneous area distribution collapses into a relatively large bleb, in which most excess area is stored, with all other protrusions being relatively flat bulges. This type of bleb formation has been reported previously in a work by Sens *et al.* to explain membrane shedding of red blood cells [155], which we also discussed in section 1.4 and at the beginning of section 3.4. They find that the local buckling of membrane into an out-of-plane protrusion leads always to the formation of a bleb. However, they did not include a pressure difference across the membrane into their calculations. As we find, this is required to stabilize the homogeneous area distribution and prevent blebbing, as described here.

3.5.2 | Equilibrium area distribution with point force perturbations

Compared to the previous section, as soon as a non-vanishing point force $\overline{f}$ is applied to all protrusions more than two equilibrium states for the area distribution are possible. All possibilities are summarized in the shape diagram in Figure 3.10a. For pressure differences above the maximal possible for tube formation (see section 3.2.4) the stability behavior is mostly comparable to the case with zero point force. Below $\Omega \approx 1$ the occurring buds are stable, above unstable, related to bleb formation. However, for pressure differences where tubes can form several stability regions occur as then the area dependency of the surface tension exhibits more than one minimum (see section 3.3.1 and Figure 3.4c). Besides the two stable regions for buds and tubes with homogeneous area distributions, two unstable regions occur. One lies in-between the stable regions, and one at larger excess areas.

The alternation of stable and unstable regions has an interesting implication, namely that, in principle, tubes and bulges can coexist and, at the same time, bleb growth can be limited. This can happen when the increasing difference of excess area, triggered by the instability, shifts some of the protrusions into the stable tube state. There the surface tension is larger than for bulges so that lipids flow towards the tubes until the bulges have reached an excess area associated with the same surface tension as the one of tubes. The final equilibrium state would be inhomogeneous, bulges would have a different excess area than tubes. The exact final configuration depends on the initial value of Ω as well as of $\overline{\Delta p}$, $\overline{f}$ and the total number of protrusions. Hence, a more quantitative analysis could give rise to an extended shape diagram where more membrane states are distinguishable.

3.5.3 | Equilibrium area distribution with partial point force perturbations

Another possibility how both membrane bulges and tubes can occur at the same time is the partial perturbation by a point force $\overline{f}$, *i.e.*, $\overline{f}$ is applied to only some bulges. In this case, for an initially homogeneous area distribution the surface tensions do not need to be identical *a priori*, since they depend differently on Ω for different point forces, as discussed in section 3.3.1. Consequently, a stable homogeneous area distribution exists at the intersection points of all surface tensions, *i.e.*, in general, only for discrete values of Ω. However, also other, inhomogeneous, equilibrium configurations, triggered by the flow equation (3.27), can allow coexisting tubes and bulges, similarly to what we discussed at the end of the previous section.

Here we study the possible coexistence of such a mixture by using the analytical limits of spherical caps and cylindrical tubes, as introduced before[10]. We assume that all tubes are subject to the same point force $\overline{f}$ and both tubes and bulges have the same initial excess area $\Omega_{\mathrm{tube}_0} = \Omega_{\mathrm{cap}_0} =: \Omega_0$. Since the surface tension of cylindrical tubes does not depend on the excess area (see, *e.g.*, (3.18)), only the surface tension of caps changes as the equilibrium state is reached and only there stable and unstable regions can be identified. As the inset of Figure 3.10b illustrates, then two equilibrium points, where $\gamma_{\mathrm{tube}} = \gamma_{\mathrm{cap}}$, exist, namely

$$\Omega_{\pm} = 2\left(\frac{\overline{\Delta p}_{\mathrm{max}}}{\overline{\Delta p}}\right)^2 \left[1 \pm \sqrt{1 - \left(\frac{\overline{\Delta p}}{\overline{\Delta p}_{\mathrm{max}}}\right)^2}\,\right] - 1 \tag{3.31}$$

---

[10] The respective surface tensions can be found in (E.24) on page 188 and in (E.37) on page 192.

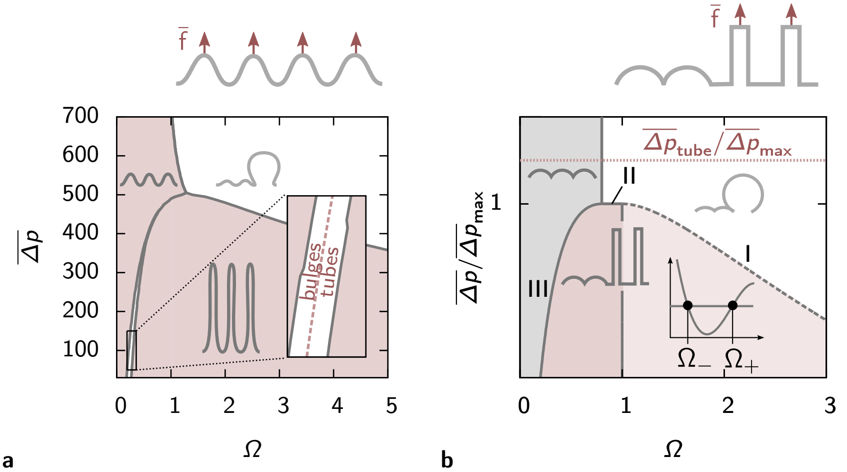

Figure 3.10 | Shape states for a collection of protrusions perturbed by local point forces. **a** shows the stability for membrane protrusions to which an external point force $\overline{f} = 100$ is applied (top left schematic) as a function of the excess area Ω and pressure difference $\overline{\Delta p}$. The red shaded area corresponds to the stable region. The inset magnifies the unstable region in the left part of the diagram. The red dashed line marks the transition line from non-tubular to tubular protrusions according to Figure 3.4c. $\overline{C}_0 = 0$ and $\Delta u = 0.01$. **b** shows the stability for a membrane consisting of a mixture of caps and cylindrical tubes with point force (top right schematic) as a function of the pressure difference $\overline{\Delta p}$ and the initial excess area Ω_0. The y-axis is normalized according to (3.32). The red shaded region corresponds to a stable coexistence of tubes and caps, where the light shaded part indicates a conditional stability (see text). In the gray shaded region only caps can be persist. In the white region blebs occur and absorb all area from tubes. The red dotted line indicates the critical pressure difference needed to form a tube (see (3.15)) and the numbers correspond to the stability conditions of (3.34) – (3.36). The inset sketches the surface tensions of both protrusion types as a function of the excess area and their intersection points. The chosen value for the cap fraction is $q = 0.8$.

with

$$\overline{\Delta p}_{\mathrm{max}} = \frac{\overline{f}^2}{2\pi^2}. \tag{3.32}$$

Assuming a homogeneous area distribution, the equilibrium excess area of a cap and a tube, respectively, reads as

$$\Omega_{\mathrm{cap}_\infty} = \Omega_\pm, \quad \Omega_{\mathrm{tube}_\infty} = \frac{q\Omega_\pm - \Omega_0}{q-1}, \tag{3.33}$$

where q is the fraction of caps on the total number of lattice elements. From (3.31) and (3.33), we can deduce that tubes only occur in the final equilibrium state if the following three conditions are satisfied:

$$\text{I:} \qquad \Omega_0 \overset{!}{<} \Omega_+, \tag{3.34}$$

$$\text{II:} \qquad \overline{\Delta p} \overset{!}{<} \overline{\Delta p}_{\text{max}}, \tag{3.35}$$

$$\text{III:} \qquad \Omega_0 \overset{!}{>} q(\Omega_- - 1) + 1. \tag{3.36}$$

The first condition accounts for the stability of caps with respect to each other. For $\Omega_0 < 1$ they are stable and, thus, reach Ω_- in equilibrium. For $1 \leq \Omega_0 < \Omega_+$, caps are unstable and a bleb forms. However, their final state depends on the exact configuration of caps and tubes. One possibility is, since their surface tension is then smaller than that of tubes, that they also equilibrate to Ω_- before the bleb can grow larger than Ω_+. Otherwise, if the bleb can reach Ω_+ or if $\Omega_0 > \Omega_+$, the occurring bleb *absorbs* all area from the tubes. In the context of Figure 3.10a absorption means that they collapse to non-tubular buds, here it simply means that they have no excess area in the final state. The same happens if the two other conditions, (3.35) and (3.36), are violated. In the first case, *i.e.*, if $\overline{\Delta p} > \overline{\Delta p}_{\text{max}}$, the surface tension of caps is always larger than that of tubes, which also causes the full absorption of tubes. In the opposed case to (3.36), caps absorb all tube area as they approach the equilibrium point Ω_-.

We summarize the conditions (3.34) – (3.36) in a shape diagram, shown in Figure 3.10b. It reveals that, indeed, for a small enough pressure difference, $\overline{\Delta p} < \overline{f}^2/2\pi^2$, and for sufficiently small excess area, $\Omega \lesssim 1$, caps can coexist with tubes. However, as discussed above, an increasing pressure difference triggers the formation of blebs where tubes disappear.

APPLICATIONS TO CELL BIOPHYSICS 4

Summary: From the general case of a membrane anchored to a substrate, as modeled in the previous chapters 2 and 3, in this chapter we focus on the cell membrane. In this case the membrane is anchored to the underlying contractile polymeric cell cortex which affects the membrane description in two important ways: First, the anchoring, maintained by linker proteins, can rupture and, thus, the membrane can detach. Second, the pressure difference $\Delta p = p_{\text{int}} - p_{\text{ext}}$ between the inside and the outside of the cell, previously used as a free parameter, is now coupled to the contractile tension within the cell cortex.

We use our findings from chapter 3 to describe the cell membrane as a collection of protrusions. Based on this picture, we introduce a closed system of equations for the membrane surface tension and shape, the pressure difference across the membrane and the cell radius, depending on subcellular parameters for the cell cortex and membrane and on the cell osmolarity. We can conclude from this description that the membrane buckles into out-of-plane protrusions due to the contractility of the cell cortex. We further discuss the implications of this buckling under different experimental conditions. First, we show that an increase of the external osmolarity can trigger the formation of blebs and tubes as described in the previous chapter. In addition, we study the formation of blebs due to

a local detachment of the membrane from the cell cortex. In the last part of this chapter we study the membrane behavior during cytokinesis. We use our membrane model to describe the buckling of membrane experimentally observed during cell pole oscillations. We derive an equation for the flow of membrane through the cleavage furrow, triggered by these oscillation. From a preliminary comparison to experimentally measured fluorescence data of the membrane we estimate the buckling state of the membrane prior pole oscillations. Moreover, we show that the cell membrane itself could also influence the oscillations by introducing a surface elasticity, arising from the local membrane buckling.

4.1 | The cell membrane as a collection of protrusions

In this chapter we consider the cell membrane as a lipid bilayer, enclosing the biological cell, anchored to the underlying cell cortex via linker proteins. It is subject to a pressure difference Δp between cell inside and outside and can locally be exerted into tubular structures by a force f induced by *spiking* cortical filaments pushing against the membrane. The filamentous structure of the cortex compartmentalizes the membrane as it attaches to it by multiple linker proteins and forms a fence-like structure (see section 1.1.2 for further details on the cell membrane). We assume here, for simplicity, that this compartmentalization can be idealized by a square lattice with equally sized unit elements as shown in Figure 4.1a.

Based on these assumptions we follow our work in chapter 3 by treating the membrane in each lattice element as an axisymmetric protrusion. Each protrusion has the same diameter l_p which is equal to the mesh size ξ of the lattice. We always start in the following from a homogeneous area distribution, *i.e.*, the excess area of each protrusion is identical to the overall cell membrane excess area, $\Omega_\mathrm{p} \equiv$

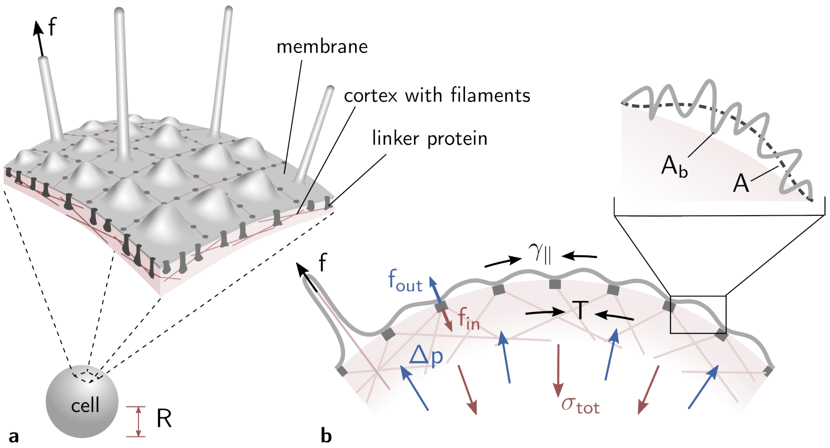

Figure 4.1 | The cell membrane as a regular mesh of protrusions with axial symmetry. a shows a sketch of the simplified structure of the cell membrane shape as assumed here. In **b** the different occurring physical forces are summarized: The lateral membrane tension $\gamma_{\|}$ and the active contractile tension T in the cell cortex sum to an overall (contractile) tension which is balanced by the pressure difference Δp. As a consequence, at each linker between membrane and cortex a force dipole is induced, as already discussed in chapter 2 (see also Figure 2.2 on page 48 for comparison). In addition, cortical filaments can locally exert a force f on the membrane which can then form a thin tube. The magnified region emphasizes the relation between the absolute membrane area A_b, stored in fluctuations, and the effective area A (see also section 1.3.2).

Ω. The apparent surface area $S = 4\pi R^2$ of the cell, with R being the cell radius, is assumed to be approximately equal to the sum of all basal protrusion areas (see approximation (3.26) on page 81). Furthermore, we assume a protrusion size that is small compared to the cell size, *i.e.*,

$$\frac{l}{R} \ll 1. \tag{4.1}$$

Then the cell curvature is negligible for individual protrusions.

With (4.1) we can use, in good approximation, our results from chapter 3 for a flat anchored membrane, modeled as a collection of protrusions. This includes, in particular, the surface tension γ and lateral tension $\gamma_{\|}$, which we obtained by solving the shape equations (3.6) and (3.7) on page 64 at a constant protrusion area and then allowed the equilibration of γ to a global value among all protrusions via lipid exchange according to (3.27) on page 82. As we found, γ and $\gamma_{\|}$ only depend on l_{p}, A_{p}, Δp and f. In the following we change the variables from

$$l_{\mathrm{p}}, A_{\mathrm{p}} \quad \rightarrow \quad R, A \tag{4.2}$$

by using the relations[1]

$$A \simeq N_{\mathrm{p}} A_{\mathrm{p}}, \quad R \simeq \frac{\sqrt{N_{\mathrm{p}}}}{4} l_{\mathrm{p}}. \tag{4.3}$$

Here N_{p} is the number of protrusions which we assume to be fixed for a given cell, determined by the mesh of the cell cortex.

4.2 | Cell mechanics based on the membrane-cortex interplay

4.2.1 | Closed description of the membrane-cortex interplay

As the cell membrane is anchored to the contractile cell cortex we expect a mechanical interaction between both and therewith a feedback on the overall cell mechanics. In order to describe this interaction we propose here a closed system of equations which combines six fundamental relations for the geometrical and mechanical state of membrane and cortex.

The first relation is given by (1.10) on page 32. It states how much total membrane area A_{b}, stored in fluctuations, is visible as the effective, accessible, membrane area A (see Figure 4.1b). This depends on the surface tension γ of the membrane and reads as

---

[1] We ignore here the area contributions coming from the corners of the square lattice which are not covered by the protrusion base (see section 3.4 for details).

$$A = A(\gamma, N_\mathrm{l}) = N_\mathrm{l}\pi\rho_\mathrm{l}^2 \left[\frac{k_\mathrm{B}\mathcal{T}}{8\pi\kappa}\log\left(\frac{\kappa q_\mathrm{max}^2+\gamma}{\kappa q_\mathrm{min}^2+\gamma}\right)+1\right]^{-1}. \qquad (4.4)$$

Here N_l is the number of lipids inside the membrane, which we assume to be fixed. The lipid number is related to A_b via the characteristic lipid surface radius ρ_l as $N_\mathrm{l} = A_\mathrm{b}/\pi\rho_\mathrm{l}^2$. For the minimal and maximal fluctuation modes in (4.4) we assume $q_\mathrm{min} = \pi/l_\mathrm{mem} \sim 2\pi\,\mu\mathrm{m}^{-1}$ and $q_\mathrm{max} = \pi/l_\mathrm{mic} \sim 200\pi\,\mu\mathrm{m}^{-1}$, where we have used $l_\mathrm{mic} \sim 5\,\mathrm{nm}$ (the characteristic length scale of the membrane, *e.g.*, its thickness) and $l_\mathrm{mem} \sim 500\,\mathrm{nm}$ (the characteristic mesh size of the cell cortex, see section 1.1.1)[2].

The second relation follows by taking into account the balance of chemical potential of water between cell inside and outside. Then the pressure difference Δp is equival to the osmotic pressure difference $\Pi_\mathrm{int} - \Pi_\mathrm{ext}$. With the help of *Van't Hoff's relation* [194, 195] we can rewrite the internal osmotic pressure of the cell Π_int by the ratio of solute molecules in the cell N_int to the total cell volume[3]. Hence, we find the relation

$$\Delta p = \Delta p(R, V_\mathrm{p}, N_\mathrm{p}, N_\mathrm{int}, \Pi_\mathrm{ext}) = k_\mathrm{B}\mathcal{T}\frac{N_\mathrm{int}}{\frac{4}{3}\pi R^3 + N_\mathrm{p}V_\mathrm{p}} - \Pi_\mathrm{ext} \qquad (4.5)$$

Here the total cell volume is the sum of the volume enclosed by the cell cortex at radius R and the volume underneath each protrusion V_p, where the latter we assume to be identical for all protrusions (see section 4.1).

The third relation is given by the force balance between outward pointing pressure difference Δp and the inward pointing stress

---

[2] In fact, the minimal mode depends on the basal diameter of each protrusion and thus on R. For simplicity, we ignore this here.

[3] Van't Hoff's relation reads as $\Pi = k_\mathrm{B}\mathcal{T}\frac{N}{V}$.

σ_{tot} at the cell surface (see Figure 4.1b). This inward pointing stress we obtain by superposing the active contractile cortex tension T with the lateral membrane tension $\gamma_{\|}$. The result read as

$$\Delta p = \Delta p(R, \gamma_{\|}, T) = \underbrace{2\frac{T + \gamma_{\|}}{R}}_{\sigma_{\mathrm{tot}}}, \tag{4.6}$$

where the right-hand side is the extension of Laplace's law (see (1.2) on page 27). The active tension T is generated by motor proteins in the cell cortex, which exert local forces on the polymeric network. In a very simple model, as stated in (1.1) on page 22, it can be assumed that $T \propto c_{\mathrm{m}}$, where c_{m} is the concentration of myosin motors.

All three relations (4.4) – (4.6) contain information on the buckling state of the membrane, (4.4) via the surface tension γ, (4.5) via the volume enclosed by a membrane protrusion V_{p} and (4.6) via the lateral membrane tension $\gamma_{\|}$. To express the quantities γ, $\gamma_{\|}$ and V_{p} we use our results from chapter 3 where we computed them numerically by solving the shape equations (3.6) and (3.7) on page 64 for axisymmetric protrusions[4]. From this we can deduce three more relations for the membrane-cortex description, determining the mechanics and geometry of membrane buckling. In general terms we can write them as

$$V_{\mathrm{p}} = V_{\mathrm{p}}(R, A, \Delta p, f, N_{\mathrm{p}}), \tag{4.7}$$

$$\gamma = \gamma(R, A, \Delta p, f, N_{\mathrm{p}}), \tag{4.8}$$

$$\gamma_{\|} = \gamma_{\|}(R, A, \Delta p, f, N_{\mathrm{p}}). \tag{4.9}$$

We now assume that the parameters N_{l}, N_{p}, N_{int}, Π_{ext}, T

---

[4] The surface tension γ is computed simultaneously with the equilibrium shape via (3.10) on page 65, $\gamma_{\|}$ from (3.20) on page 77 and V_{p} from the volume formula in Table B.1 on page 150.

and f are known. Here N_l, N_p, T and f are those parameters describing the state of the coupled membrane-cortex layer. Moreover, the latter three contain, implicitly, further details on the cell cortex configuration itself, *e.g.*, its network geometry and local force generations, which are, in turn, related to the number and activity of other molecules, for instance of actin, myosin and cross-linker proteins. With this knowledge, the six relations (4.4) – (4.9) become a closed system of equations for the four geometrical quantities cell radius, membrane area, cell volume and protrusion volume, and the three mechanical quantities, pressure difference, surface tension and lateral tension:

$$N_\mathrm{l}, N_\mathrm{p}, N_\mathrm{int}, \Pi_\mathrm{ext}, T, f \quad \overset{(4.4)\,-\,(4.9)}{\Longrightarrow} \quad R, V, A, \Delta p, \gamma, \gamma_{||}, V_\mathrm{p}. \tag{4.10}$$

Thus, the closed equation system determines the mechanical and geometrical state of the cell self-consistently by underlying subcellular parameters of the cytoskeleton and the membrane and by the cell osmolarity. In particular it determines the pressure difference Δp, the membrane area A and the protrusion diameter l_p, which we used as free parameters in the previous chapters. Also the radius R, which marks the position of the cell cortex, is here no longer a free parameter[5]. Furthermore, we assume the following approximate values for the subcellular parameters on the left-hand side of (4.10): The tension T is of the order of $100\,\mathrm{pN}/\mu\mathrm{m}$ [16, 24]. The local point force f is of the order of $10\,\mathrm{pN}/\mu\mathrm{m}$ [196, 197]. The external osmotic pressure Π_ext is of the order of 10^6 Pa for typical osmolarities (molar concentrations) in biological solutions [198]. With an assumed cell radius of $R \sim 5\,\mu\mathrm{m}$ this implies $N_\mathrm{int} \sim 10^{11}$. N_l and N_p can be estimated from the cell radius, the respective apparent cell surface area S, the radius of a lipid, $\rho_\mathrm{l} \sim 0.5\,\mathrm{nm}$ [9], and the membrane anchoring mesh size, $\xi \sim 500\,\mathrm{nm}$, respectively. Then $N_\mathrm{l} \sim 10^6$ and $N_\mathrm{p} \sim 1000$.

---

[5] We here consider the cell to be at steady-state so that the cell cortex has already adopted this radius.

The proposed self-consistent description of the coupled membrane-cortex layer is, to our best knowledge, the first that connects the global mechanical and geometrical state of a cell to subcellular parameters. Although other mechanical models for cells, based on cortical tension superposed with the membrane surface tension, have been proposed before (*e.g.*, in [154]), our approach includes, for the first time, the out-of-plane shape, and the resulting buckling mechanics, of the membrane.

4.2.2 | Self-consistent solution for the membrane-cortex interplay

To solve the closed system of equations (4.4) – (4.9), we ignore for now the effect of cortical filaments pushing against the membrane, *i.e.*, we assume $f = 0$. At the same time, we ignore local forces that apply to individual anchoring points between membrane and cortex. Furthermore, we neglect effects arising from the flow between protrusions (see section 3.4) and consider all protrusions to be identical, with the same basal diameter and excess area. We will discuss the effects of local forces exerted to the membrane and membrane flow in the context of bleb and tube formation in section 4.3.

For a vanishing cortical tension, $T = 0$, the closed system of equations (4.4) – (4.9) can be solved analytically, as we show in appendix G. The result is a round cell shape with the membrane being tightly attached to the underlying cell cortex. This implies the following relations:

$$A_0 = 4\pi R_0^2, \quad V_0 = \frac{4}{3}\pi R_0^3, \quad \Delta p_0 = 2\frac{\gamma_0}{R_0}. \tag{4.11}$$

Furthermore, γ_0 can be expressed as a function of R_0:

$$\gamma_0 = \frac{3k_\mathrm{B}\mathcal{T}N_\mathrm{int} - 4\pi R_0^3\,\Pi_\mathrm{ext}}{8\pi R_0^2} \tag{4.12}$$

and R_0 itself is defined via the implicit relation

$$\frac{N_\mathrm{l}\rho_\mathrm{l}^2}{4R_0^2} = 1 + \frac{k_\mathrm{B}\mathcal{T}}{8\pi\kappa}\log\left[\frac{3k_\mathrm{B}\mathcal{T}N_\mathrm{int} + 8\pi\kappa q_\mathrm{max}^2 R_0^2 - 4\pi\Pi_\mathrm{ext}R_0^3}{3k_\mathrm{B}\mathcal{T}N_\mathrm{int} + 8\pi\kappa q_\mathrm{min}^2 R_0^2 - 4\pi\Pi_\mathrm{ext}R_0^3}\right]. \tag{4.13}$$

Hence, the value of R_0 depends on two effects, the pressure difference arising from the number of solute molecules inside the cell N_int and the outer osmotic pressure Π_ext and the membrane area stored in fluctuations. In the limit of $N_\mathrm{int} \to \infty$, with a finite value of Π_ext, all fluctuations disappear and $R_0 \to \rho_\mathrm{l}\sqrt{N_\mathrm{l}}/2$. Whereas R_0 remains strictly positive for any values of N_int and Π_ext, γ_0 and therewith Δp_0 can become negative. The biological implications of both, a negative surface tension and a negative pressure difference, are not fully understood yet. However, there is evidence that for most conditions negative surface tensions destabilize the persistent membrane shape leading to spontaneous membrane shedding [199–201]. Small negative pressure differences might be resisted by inverted membrane buckling and the corresponding energy cost due to curvature but likely lead to a collapse of the cell above a critical value. That is why, and since we only studied the membrane mechanics for $\Delta p > 0$ in the previous chapters, we only consider positive pressure differences in the following. To ensure $\Delta p > 0$ we choose the initial ratio of N_int and Π_ext for $T = 0$ with the help of (4.12) accordingly.

For non-vanishing contractile cortex tensions, $T > 0$ the equation system (4.4) – (4.9) can, in general, only be solved numerically, as described in appendix G. The results for the above discussed parameter values are shown in Figure 4.2. The first interesting result is that the pressure difference Δp differs significantly from the term

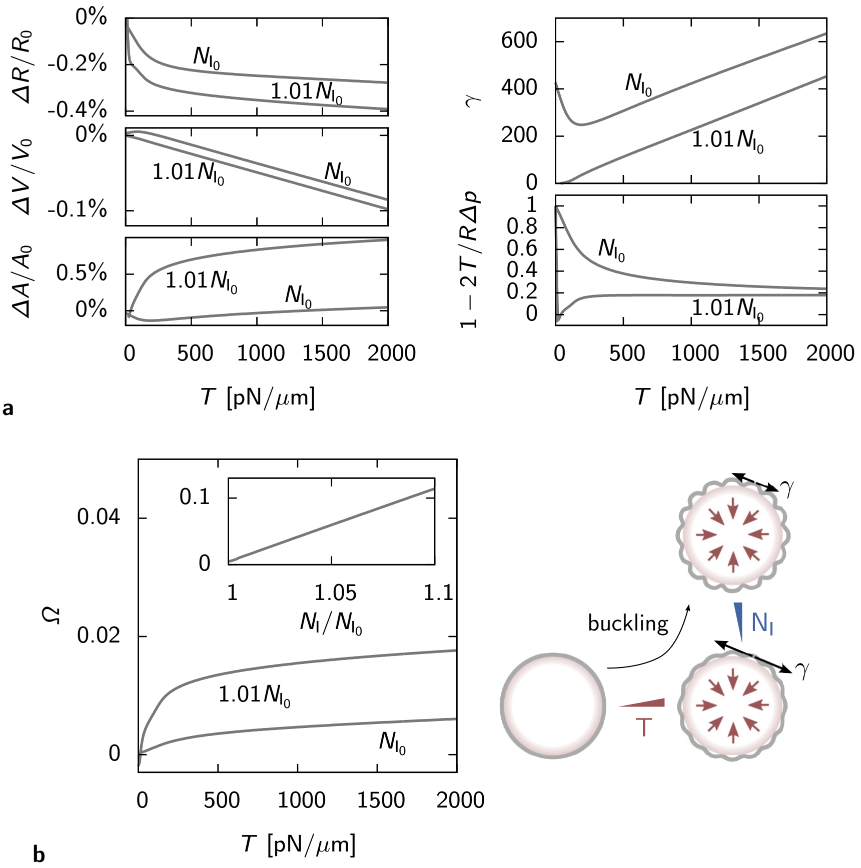

Figure 4.2 | Global cell parameters determined through the interplay of cell membrane and cell cortex. The left plots in **a** show the numerical results for the relative changes of cell radius R, volume V and area A upon change of cortex tension T. R_0, V_0 and A_0 are the reference values at $T = 0$ (see (4.11) and (4.13)). The right plots in **a** show the surface tension γ and the ratio of Laplace's law $2T/R$ with the full pressure difference Δp as a function of T. **b** shows the increase of excess area due to membrane buckling for increasing tension and increasing lipid number (inset plot). All plots are shown for two different lipid numbers, $N_{l_0} = 1.6 \cdot 10^9$. The other parameters are chosen as $\Pi_{\text{ext}} = 10^6$ Pa, $N_{\text{int}} = 1.29 \cdot 10^{11}$, $q_{\text{min}} = 2\pi\,\mu\text{m}^{-1}$, $q_{\text{max}} = 200\pi\,\mu\text{m}^{-1}$, $\kappa = 20\,k_{\text{B}}T$, $\rho_l = 0.25\,$nm, $N_p = 1000$, $f = 0$. The schematic on the lower right illustrates how membrane buckling is affected by an increase of cortex tension and lipid number, respectively.

$2T/R$, coming from the cortex tension (Figure 4.2a). At $T = 0$ the deviation is maximal as Δp is fully determined by the surface tension γ_0. For larger T the deviation decreases. However, even for relatively large tensions ($T = 2000\,\mathrm{pN}/\mu\mathrm{m}$) it differs by approximately 20 %. This indicates that the contribution from the lateral membrane tension to the force balance (4.6) is not negligible for the mechanics of a cell. The found order of magnitude for the contribution agrees with previous experimental estimates [166, 202]. That the contribution does not vanish even for large cortex tensions is due to the fact that we assume a constant bare membrane area A_b so that γ itself is a function of Δp. If we recall the approximate analytical result for this relation from our membrane model in chapter 3, $\gamma \sim \Delta p$, (see (3.21) on page 78), we find the asymptotic relation

$$\Delta p \propto \underbrace{\left[1 - \frac{4}{\sqrt{N_\mathrm{p}}}\bar{r}_\parallel\right]^{-1}}_{\geq 1} \frac{2T}{R} \quad \text{for} \quad T \to \infty. \tag{4.14}$$

The second important observation we can deduce from Figure 4.2b is the buckling of membrane. Whereas for $T = 0$ the membrane is tightly attached to the spherical cell cortex, it starts to form small out-of-plane protrusions for $T > 0$, associated with an increasing excess area of the cell. Since a sphere and only a sphere has minimal surface area for a given volume [203] the observed buckling, starting from a spherical shape, requires a finite volume or surface area elasticity. We have accounted for both elasticities by including (4.4) and (4.5) to our description. We can estimate the magnitude of these elasticities by linearizing (4.4) and (4.5) around the spherical state at $T = 0$:

$$\gamma \approx \gamma_0 + K_A \frac{A - A_0}{A_0}, \tag{4.15}$$

$$\Delta p \approx \Delta p_0 + K_V \frac{V - V_0}{V_0}. \tag{4.16}$$

Here K_A is the surface area elasticity and K_V the volume elasticity whose expressions we provide in appendix G. For the parameters used in Figure 4.2 and $N_\mathrm{l} = N_{\mathrm{l}_0} = 1.6 \cdot 10^9$ we find $K_A \approx 3.2 \cdot 10^6\,\mathrm{pN}/\mu\mathrm{m}$ and $K_V \approx -1.3 \cdot 10^7\,\mathrm{Pa}$. The different signs of both constants imply that both an increase of the surface tension, $\gamma > \gamma_0$, and an increase of the pressure difference, $\Delta p > \Delta p_0$, induces excess area because in the first case the effective membrane area increases, $A > A_0$, and in the second case the cell volume decreases, $V < V_0$. Hence, also an increasing cortex tension induces excess area, as it increases Δp according to (4.6) and also indirectly γ. However, the magnitudes of K_A and K_V are relatively large in comparison to typical values of $\gamma \sim 100\,\mathrm{pN}/\mu\mathrm{m}$ and $\Delta p \sim 100\,\mathrm{Pa}$ in cells [166,202]. That is why the relative changes of V and A are with a value of approximately 0.1 % very small for the chosen parameters (Figure 4.2a) and only little excess area is stored in membrane protrusions (Figure 4.2b). Interestingly, the buckling effect becomes more significant when the bare membrane area is slightly increased by adding more lipids to the membrane (inset of Figure 4.2b). For choosing $N_\mathrm{l} = 1.01 N_{\mathrm{l}_0}$, the area elasticity drops to $K_A \approx 2.0\,\mathrm{pN}/\mu\mathrm{m}$. This elasticity decrease can be understood by the fact that more membrane area encloses a larger volume so that for a fixed number of solute molecules N_int the pressure difference decreases[6]. This, in turn, leads to a decrease of surface tension and thus more membrane stored in fluctuations.

The discussed relation between membrane surface tension and membrane buckling could provide a better understanding of how the membrane actually regulates its surface tension. More precisely, our findings indicate that the membrane buckling could be a mechanism for the cell to reduce its surface tension and, at the same time, provide membrane excess area that can be used to buffer spontaneous cell shape changes.

---

[6] Similarly, Δp would decrease for a constant lipid number but reduced solute molecule number.

4.3 | Membrane blebs and tubes

With the help of the self-consistent description for the interplay of cell membrane and cortex, introduced in the previous section, we can make predictions under which conditions a cell membrane exhibits characteristic out-of-plane structures, namely membrane tubes, invaginations and blebs. We can do this because the self-consistent description links subcellular cell properties (left-hand side of (4.10)) via the mechanical cell state, mainly determined by Δp and γ, to the underlying mechanisms, causing these out-of-plane structures.

4.3.1 | Blebbing and tubulation caused by cortical filaments and lipid flow

We ignored for the self-consistent solution in section 4.2.2 the membrane flow and a possible point force at protrusion tips coming from cortical filaments pushing locally against the membrane. However, as we showed in section 3.5, these two effects trigger the formation of membrane blebs and membrane tubes (microvilli). Tubes form when the force is large enough to elongate a protrusion bulge, blebs when the membrane surface tension promotes an accumulation of lipids in one protrusion, destabilizing a homogeneous area distribution. We found that the position of the different transitions is defined by the three parameters membrane excess area Ω, normalized pressure difference $\overline{\Delta p}$ and normalized point force $\overline{f}$ (see Figure 3.9a on page 85 and Figure 3.10a on page 89). As introduced in the beginning of chapter 3, the normalizations of the pressure difference Δp and of the force f contain the protrusion diameter l_p. This, in turn, depends on the cell radius R via (4.3). Hence, for given cell radius and point force, the formation of the considered tubes and blebs is fully determined by Ω and Δp. However, in experiments there is usually no direct control of these two quantities. Instead common control parameters are the external osmotic pressure Π_ext and the cortex tension T [7].

Qualitatively, according to our findings in section 4.2.2, we expect that T mainly affects Δp, whereas Ω is mostly influenced by Π_ext. Ω also increases with increasing T, as we discussed, however, for a given contractile tension $T > 0$ deswelling the cell has a larger effect. This can be achieved by either increasing the bare membrane area, as discussed in section 4.2.2, or by increasing Π_ext, as discussed here. Quantitatively, we relate the computed values for Ω and Δp where the transitions to tubes and blebs occur to values for T and Π_ext by the following procedure: First, we calculate R as a function of Ω, Δp and f. It is given implicitly by the fluctuation relation (4.4) where we replace γ by (4.8). Second, having R, we solve (4.5) and (4.6) for Π_ext and T, respectively. The obtained relations

$$\Pi_\mathrm{ext} = \frac{\sqrt{N_\mathrm{p}}}{320\pi R^3}\left[\frac{12 N_\mathrm{int}}{\sqrt{N_\mathrm{p}} + 12 V_\mathrm{p}} - 5\pi\Delta p\,\kappa N_\mathrm{p}\right], \tag{4.17}$$

$$T = \frac{\kappa\, N_\mathrm{p}}{128 R^2}\left[\Delta p\sqrt{N_\mathrm{p}} - 8\gamma_{\|}\right] \tag{4.18}$$

depend only on given subcellular parameters and via R, V_p and $\gamma_{\|}$ on Ω, Δp and f. Here V_p and $\gamma_{\|}$ are determined by our membrane model, according to (4.7) and (4.9). Hence, (4.17) and (4.18) directly map the transition from Ω and Δp values to Π_ext and T values, assuming a fixed point force f. The resulting transition lines (lines i and iii) are shown in the shape diagrams of Figure 4.3 for $f = 0\,\mathrm{pN}$ and $f = 20\,\mathrm{pN}$.

---

[7] The cortex tension can be modified by myosin inhibitors as *e.g. Blebbistatin* [204]

For a potential experimental comparison the most important result is that for a constant tension an increase of the external osmolarity, *i.e.*, the deswelling of the vesicle, can trigger the formation of blebs, on the one hand, and of cortex driven tubes on the other hand. The latter transition, however, occurs only for small enough cortex tensions below $T \approx 1000\,\mathrm{pN}/\mu\mathrm{m}$. This limiting tension is of the order of typical tensions in biological cells (see section 1.1.1) so that, in principle, it should be possible to observe the transition experimentally. Furthermore, we find that an increase of tension can stop blebbing if the external osmotic pressure is small enough, here $\Pi_{\mathrm{ext}} \approx 2 \cdot 10^7\,\mathrm{Pa}$. Both the prevention of tubes and blebs towards larger tensions seems to be counterintuitive at a first glance. Indeed, above a critical value tension can also cause blebbing, namely by local membrane detachment from the cortex (transition line ii in Figure 4.3), as we will discuss in the next section. However, the blebbing mechanism discussed here, caused by membrane flow, is stabilized by tension. In case of tubes our finding is owed the fact that we assume the force f of one cortical filament to be uncorrelated to the tension and therefore to the concentration of motor proteins. If we would impose a relation between f and T, likely, the tube region in Figure 4.3b would extend towards increasing tensions.

To visualize the relation between Ω, Δp and T, Π_{ext}, we added to Figure 4.3a dotted lines indicating the position of constant excess areas and constant pressure differences. The excess area scales, as expected, in good approximation linearly with the external osmotic pressure. The pressure difference, on the other hand, depends on both T and Π_{ext} for most values. In the limit $T \to 0$ it only depends on Π_{ext}, according to (4.12) and can be both positive and negative as also the surface tension can be (red dashed line in Figure 4.3a).

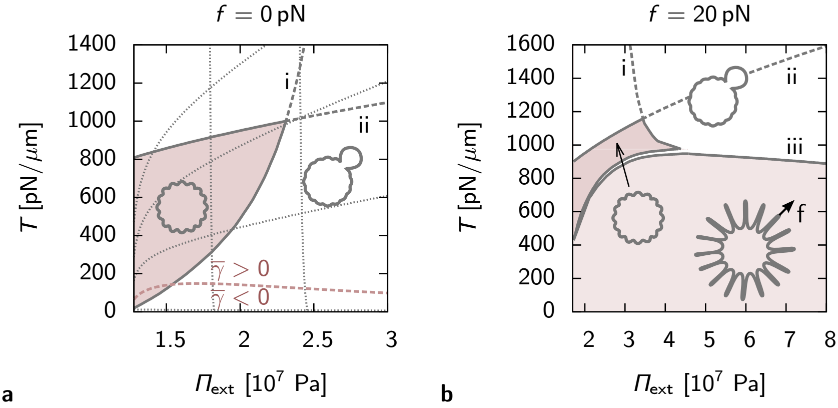

Figure 4.3 | Theoretical prediction for cell blebbing and cortex driven tubulation. **a** shows the formation of blebs as a function of external osmotic pressure Π_{ext} and cortex tension T. The red shaded region corresponds to a stable area distribution (see section 3.5). In the white region blebs can occur due to two different effects: The transition line i marks blebbing due to membrane flow, as discussed in section 4.3.1. The transition line ii marks blebbing due to local membrane detachment, as described in section 4.3.2. The assumed rupturing force is $f_{\mathrm{r}} = 20\,\mathrm{pN}$ and the number of anchors per protrusion $n_{\mathrm{a}} = 5$. The red dashed line indicates where the surface tension γ changes its sign. The thin dotted lines correspond to constant pressures (from bottom to top: $\Delta p = 0$, 400, 800, 1200) and constant excess areas (from left to right: $\Omega = 0$, 0.3, 0.6), respectively. In **b** an additional point force, generated by cortical filaments pushing against the protrusions tips from the cell inside, is included. The additional region, where tubes form (transition line iii), is shaded light red. The other parameters for **a** and **b** are chosen as in Figure 4.2 with $N_{\mathrm{l}} = 1.6 \cdot 10^9$.

Then also the excess area does not depend on Π_{ext} any longer, since the cell is perfectly spherical with $\Omega = 0$.

4.3.2 | Blebbing and tubulation caused by the discrete membrane anchoring

Another aspect we ignored for the self-consistent solution in section 4.2.2 is the contractility-driven exertion of local forces at each anchoring point between cell cortex and cell membrane. The contractile stress $2T/R$ is *pulling* on the linker proteins, whereas the opposed positive pressure difference is *pushing* against the membrane, both together leading to force balance expressed by a *force dipole* as shown in Figure 4.1 (see also the discussions in sections 2.1, 2.3.2 and 3.3.3). The related resistive force per linker can be deduced from the protrusion force (3.24) on page 79:

$$f_\mathrm{a} = \frac{8\pi R T}{N_\mathrm{p} n_\mathrm{a}}, \tag{4.19}$$

where the pressure difference is here replaced by the active stress and $n_\mathrm{a} := N_\mathrm{a}/N_\mathrm{p}$ is the number of anchors per protrusion[8]. The force f_a gives rise to a second type of blebbing, besides the one presented in the previous section, caused by a local membrane detachment from the underlying cortex. This can happen when f_a exceeds a critical rupturing force [149, 165]

$$f_\mathrm{r} = \text{const.}\,, \tag{4.20}$$

which we assume to be constant and determined by protein binding interactions. For cells f_r is typically of the order of tens of piconewton [149, 205].

Alternatively to the detachment, the membrane can also invaginate locally into the cell, a process that could be associated to endosome formation [206]. We expect this to happen when, first, a cortical filament is anchored almost perpendicular to the membrane and, second, when the filament pulls with a force large enough to buckle the membrane inwards and to form a tube. A first order approximation for the force required to pull such a tube is given by the force needed to maintain a tube (see (3.18) on page 76):

---

[8] n_a is identical to $2q + 1$ anchors per lattice element as introduced in chapter 2.

$$f_\mathrm{t} \approx 2\pi\sqrt{2\kappa\gamma}\,. \tag{4.21}$$

By combining the two effects, membrane detachment and invagination, we can distinguish the following four regimes:

$$\begin{aligned} \text{I:} &\qquad f_\mathrm{a}< f_\mathrm{t} \quad \& \quad f_\mathrm{a} < f_\mathrm{r}, \qquad (4.22)\\ \text{II:} &\qquad f_\mathrm{a}> f_\mathrm{t} \quad \& \quad f_\mathrm{a} < f_\mathrm{r}, \qquad (4.23)\\ \text{III:} &\qquad f_\mathrm{a}> f_\mathrm{t} \quad \& \quad f_\mathrm{a} > f_\mathrm{r}, \qquad (4.24)\\ \text{IV:} &\qquad f_\mathrm{a}< f_\mathrm{t} \quad \& \quad f_\mathrm{a} > f_\mathrm{r}. \qquad (4.25) \end{aligned}$$

For condition I we expect the membrane to remain anchored to the underlying cortex as described before. In case of condition II the membrane forms tubular invaginations and in case of condition III and IV blebs, caused by detachment from the cortex. The transition lines, which separate these regions, can be found by setting $f_\mathrm{a} = f_\mathrm{r}$ and $f_\mathrm{a} = f_\mathrm{t}$. We solve both relations for the number of anchors per protrusion

$$n_\mathrm{a}^{(r)} = \frac{8\pi R T}{N_\mathrm{p} f_\mathrm{r}}, \tag{4.26}$$

$$n_\mathrm{a}^{(t)} = \frac{4 R T}{N_\mathrm{p}\sqrt{2\kappa\gamma}}. \tag{4.27}$$

Plugging our self-consistent solution from section 4.2.2 for $R(T)$ and $\gamma(T)$ into (4.26) and (4.27), we can express n_a as a function of T only. The inverse $T(n_\mathrm{a})$ gives the critical tension above which invaginations and detachment can occur. The resulting shape diagram is shown in Figure 4.4a, based on the parameters used in Figure 4.2 ($N_\mathrm{l} = 1.6 \cdot 10^9$) and for an assumed rupturing force $f_\mathrm{r} = 40\,\mathrm{pN}$. The shape diagram reveals that there is indeed a separate parameter range where, according to the conditions (4.22) – (4.25), only tubular invaginations can occur. On the one hand, the corresponding cortex tension lies between $T \approx 200\,\mathrm{pN}/\mu\mathrm{m}$ and $T \approx 1000\,\mathrm{pN}/\mu\mathrm{m}$ and is thus of the order of typical cellular values. On the other hand, for a given cortex tension, the corresponding range of anchors per protrusion for which invaginations can occur, is relatively narrow ($\Delta n_\mathrm{a} < 1$) and above a certain value invaginations cannot occur anymore. We find that the value of this upper limit is mainly defined by the rupturing force f_r and the excess area Ω of the membrane. It increases with both increasing f_r and increasing Ω. However, for values $f_\mathrm{r} \sim 10\,\mathrm{pN}$ and $\Omega \lesssim 0.01$ the upper limit appears at relatively small values, $n_\mathrm{a} \lesssim 5$ [9]. Based on these findings, we conclude that the described formation of tubular invagination is presumably rather a rare event in cells that requires a relatively low number of about five linker proteins per protrusion[10]. In contrast, the occurrence of blebs is much more dominant. It can happen, in principle, for any value of n_a above a critical tension (regions III and IV in Figure 4.4a). For a given value of n_a, this critical tension gives rise to an additional transition line (line ii) in the shape diagrams Figure 4.3a and Figure 4.3b, below which outward pointing tubes and blebs occur as discussed in the previous section and above which blebs caused by the described local detachment appear[11].

In a recent collaboration with the group of Andreas Bausch and there in particular with Etienne Loiseau[12] we used the force description above to characterize the blebbing observed in a novel type

---

[9] See for visualization of this anchoring number Figure 2.2 on page 48 (q=2).

[10] This result suggests that other mechanisms that trigger endocytosis, such as spontaneous curvature induction, could be more efficient and thus more favorable for cells.

[11] Note that the transition line ii in Figure 4.3 depends on the external osmotic pressure Π_ext because the cell radius R, entering (4.19), changes with Π_ext.

[12] Biophyics Division, Faculty of Physics, Technische Universität München, Germany.

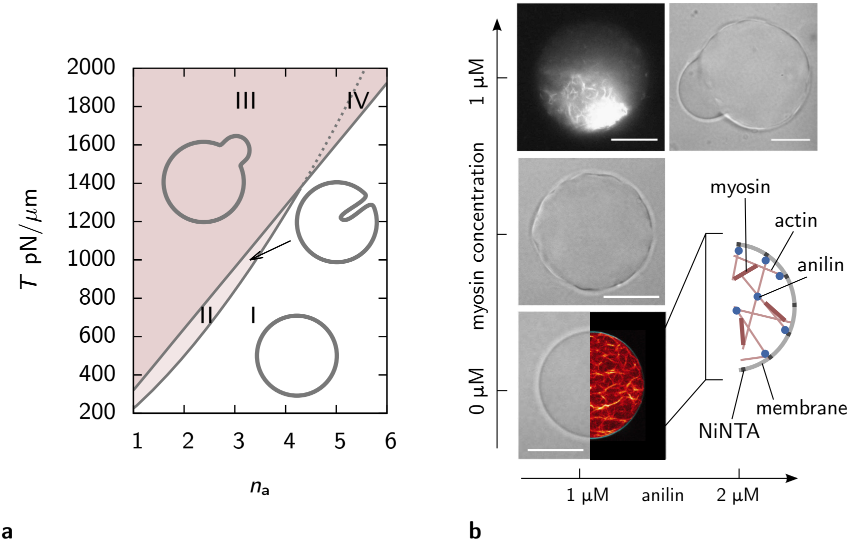

Figure 4.4 | Membrane perturbations caused by local anchoring forces. a shows the theoretical prediction of local membrane invaginations and bleb formation due to detachment of the membrane from the underlying cortex as a function of the contractile cortex tension T and anchor number per protrusion n_a. In the red shaded region blebs occur, in the light shaded region tubular invaginations occur, otherwise the vesicle shape is round, covered by small protrusions of equal excess area. The indicated numbers correspond to the regions introduced in (4.22) – (4.25). The theoretical lines are calculated according to the self-consistent solution in section 4.2.2, with the same parameters as in Figure 4.2. The used rupturing force is $f_r = 40\,\mathrm{pN}$. **b** shows experimental images of an *in-vitro* active membrane vesicles for different amounts of myosin ($1\,\mu\mathrm{M} \approx 602\,\mathrm{particles}/\mu\mathrm{m}^3$) and anilin (further description see text). The other vesicle parameters are identical: actin concentration $c_{ac} = 10\,\mu\mathrm{M}$, NiNTA concentration 10 %.Images are taken with a bright-field and confocal microscope. Scale bar: $20\,\mu\mathrm{m}$. [Images provided by Etienne Loiseau, Technische Universität München].

of *in-vitro* membrane vesicles [207]. These vesicles are filled with a cross-linked *actin* network which is put under active stress via *myosin* motor filaments. Moreover, the network is bound to the outer vesicle membrane via *anilin* proteins, which bind to *NiNTA* receptors, present in the membrane. A schematic as well as a confocal image of such a vesicle is provided in Figure 4.4b. Also shown there are vesicles at different myosin concentration ($0\,\mu$M, $0.5\,\mu$M, $1\,\mu$M) and anilin concentrations ($1\,\mu$M, $2\,\mu$M). An increase of the myosin concentration is associated to an increase of the active stress in the vesicle, an increase of the anilin concentration to a higher anchoring density between actin network and membrane. As the example vesicles in Figure 4.4b indicate, it systematic experimental analysis reveals that a change from intermediate myosin concentrations ($0.5\,\mu$M) to large myosin concentrations ($1\,\mu$M) induces bleb formation of the initially round vesicle, caused by a local detachment of the membrane from the actin network. For a low enough anchoring density this detachment leads, eventually, to a complete collapse of the contractile actin network (Figure 4.4b top left). For larger anchoring density the network does not collapse, only a localized bleb occurs (Figure 4.4b top right). These observations agree qualitatively with the dependency on n_a of the transition line shown in Figure 4.4a. As both conditions lead to blebbing the one with the larger anchoring density is closer to the transition line. This could explain the smaller bleb since we expect according to previous work that blebs can releases pressure [166] and thus can trigger a stabilization of the network-membrane anchoring, here by moving down in the shape diagram Figure 4.4a.

With the help of the discussed experimental observations we can give a quantitative estimate of the rupturing force magnitude in such vesicles. We do this by setting $f_\mathrm{r} = f_\mathrm{a}$ and replace in the expression (4.19) of f_a the contractile tension by and active stress $\sigma = 2T/R$ and furthermore the total anchor number by $N_\mathrm{a} = 4\pi R^2/l_\mathrm{a}^2$, where l_a is the mean distance between anchoring points. We then find

$$f_\mathrm{r} = 2\,\sigma l_\mathrm{a}^2. \tag{4.28}$$

We can estimate σ from the myosin concentration via the relation $\sigma \simeq f_{\mathrm{mf}} l_{\mathrm{mf}} c_{\mathrm{m}} / n_{\mathrm{mf}}$ (see section 1.1.1). The length of a myosin filament is approximately $l_{\mathrm{mf}} \approx 1\,\mu\mathrm{m}$ in the vesicle, with 100 motors participating in one filament. The force of a filament is of the order of $f_{\mathrm{mf}} \approx 20\,\mathrm{pN}$, *i.e.*, a myosin concentration of $1\,\mu\mathrm{M}$, as required for bleb initiation in vesicles, corresponds to a stress of about $\sigma \approx 120\,\mathrm{Pa}$. The mean anchor distance can be estimated experimentally by analyzing intensity profiles of the anilin distribution within the vesicle [207]. For vesicles with an anilin concentration $c_{\mathrm{an}} = 0.2\,\mu\mathrm{M}$ the distance is of the order of $l_{\mathrm{a}} \approx 36\,\mathrm{nm}$. Hence, we find $f_{\mathrm{r}} \approx 0.3\,\mathrm{pN}$, which is approximately two orders of magnitude smaller than the force measured in cells [149]. The reason for such a large difference could be that in cells the anchoring is achieved by a much more complex interplay of different linker proteins [45, 208] than in the vesicle. Cells might favor such strong binding in order to guarantee an intact connection between membrane and cortex for a large range of contractile tensions and to avoid a complete membrane detachment as observed for the described vesicles.

4.4 | Cell membrane mechanics during cytokinesis

4.4.1 | Membrane buckling due to cell pole contractions

As a consequence of Laplace's instability cell pole oscillations can occur during cytokinesis, the last stage of cell division (see section 1.2 and [26]). Recent observations of the cell membrane during these oscillations, presented in section 1.4, have revealed that the membrane buckles on the contracted pole and appears relatively flat on the expanded. A supporting illustration of this membrane out-of-plane structuring is shown in Figure 4.5. Experimentally it has been verified that the volume of the cell during cytokinesis is constant [26, 209]. Furthermore, also the surface area of the membrane

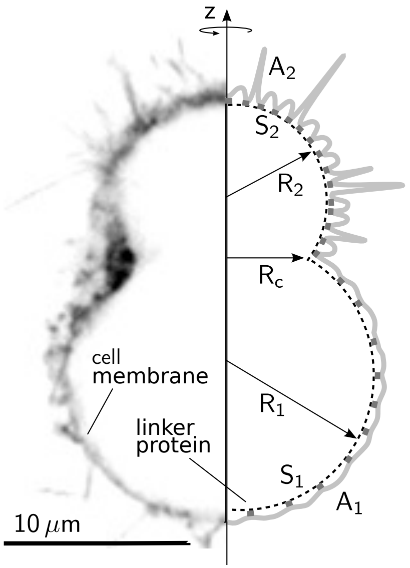

Figure 4.5 | Cross section of a cell during cytokinesis. The left side shows a part of Figure 1.6 (confocal image of the fluorescently labeled cell membrane, intensity inverted). The right part illustrates the expected shape of the membrane. R_1 and R_2, S_1 and S_2, A_1 and A_2 are the radii, apparent areas and membrane areas of the two cell poles, respectively. R_c is the radius of the cleavage furrow.

seems to be conserved, an observation we will further discuss in 4.4.2. With these two conservations, the remaining equations of the closed system of equations in section 4.2.1 are (4.6), (4.8) and (4.9). They imply that the Laplace pressure in (1.2) on page 27, driving the oscillations, must be extended by a contribution from the membrane. In general, we can write

$$\frac{\alpha}{V_\mathrm{s}}\frac{dV_1}{dt} = -\frac{\alpha}{V_\mathrm{s}}\frac{dV_2}{dt} \equiv \frac{\alpha}{2}\frac{d\tilde{V}_{12}}{dt} = -\Delta p_{12}, \tag{4.29}$$

where $\Delta p_{12} := \Delta p_1 - \Delta p_2$ and $\tilde{V}_{12} := (V_1 - V_2)/V_\mathrm{s}$ [13].

We can understand the observed buckling during cell pole oscillations in a first simple approach with the help of our membrane model of section 4.1 and the assumption that the membrane area of each pole remains constant, *i.e.*, the cleavage furrow acts as a diffusion barrier for lipids. The buckling is then simply caused by the contraction of the anchoring lattice, due to the decrease of the cell pole volume. We can estimate the effect of contraction by assuming the following further simplifications: First, the cell poles are approximately portions of spheres, which connect at the cleavage furrow with constant radius R_c (see Figure 4.5). Second, the geometry of the anchoring lattice remains unchanged, implying that the number of protrusions N_p is constant on each pole during oscillations. Then N_p can be computed by the mesh size ξ_i and the apparent surface area S_i on either pole via $N_\mathrm{p} = 4S_i/\pi\xi_i^2$. Last, the volume contribution coming from the protrusions is taken to be negligible compared to the total cell volume. Subsequently, R_i and ξ_i can be related as follows[14]:

---

[13] V_s is the pole volume in case of symmetric poles, as introduced before.

$$\xi_i = R_i\sqrt{\frac{8}{N_\mathrm{p}}\left(1+\sqrt{1-\frac{R_\mathrm{c}^2}{R_i^2}}\right)}. \tag{4.30}$$

Hence, with characteristic values for the furrow radius and radius R_s and mesh size ξ_s in case of symmetric poles we can estimate N_p and via (4.30) the change of excess area upon a contraction of one pole:

$$\Omega_i = (\xi_\mathrm{s}/\xi_i)^2\Omega_\mathrm{s}. \tag{4.31}$$

From electron microscopy images, *e.g.*, from Figure 1.6 on page 40 we estimate that $R_\mathrm{s} \approx 9\,\mu\mathrm{m}$, $R_\mathrm{c} \approx 5\,\mu\mathrm{m}$ and $\xi_\mathrm{s} \approx 0.8\,\mu\mathrm{m}$. From these values we can deduce $N_\mathrm{p} \approx 1900$. Furthermore, if we assume an initial excess area of $\Omega_{texts} \approx 0.1$, and consider a pole contraction to $R_i \approx 7\,\mu\mathrm{m}$, the excess area increases to $\Omega \approx 1$, associated to protrusions with almost hemispherical shape. This, in turn, could explain the formation of membrane tubes and blebs observed during cell pole oscillations (see Figure 1.6 on page 40), as according to our findings in section 3.5 an increase of excess area can trigger both bleb and tube formation.

---

[14] The geometrical relations for a spherical segment can be taken, *e.g.*, from the relations of a spherical cap in appendix E.2.

4.4.2 | Flow equation for lipid exchange across the cleavage furrow

For a constant membrane area on each cell pole, as assumed in the previous section, the maximal possible pole expansion would be limited by the initial excess area. This could, in practice, lead to very large membrane tensions and, potentially, a lysis of the membrane. One known mechanism to buffer such large tensions is the change of endocytosis and exocytosis rates and thus of the membrane area, as discussed in sections 1.1.2 and 4.2.2. However, we expect that this change is too slow for cell pole oscillations with typical periods of the order of a few minutes. On the other hand, there is experimental evidence that lipids can, in principle, exchanged between cell poles through the cleavage furrow (see schematic in Figure 4.6) [62]. Hence, a large increase of membrane tension in the expanding cell pole could be buffered by lipid flow from the contracting cell pole with available excess membrane area through the cleavage furrow. A preliminary experimental verification of this mechanism has been made recently by Ortrud Wartlick from Ewa Paluch's group[15]. She labeled the membrane as well as free lipids in the cytoplasm of a mouse fibroblast cell with a fluorescent marker and found that, indeed, the total membrane intensities of both poles can undergo oscillations, as shown for one example cell in Figure 4.6b (middle)[16]. Moreover, these oscillations are correlated to those of the cell pole volumes (Figure 4.6b bottom). The relative change of the membra-

---

[15] Medical research Council, Laboratory for Molecular Cell Biology, University College London, UK.

[16] Out of 12 cells 8 showed such persistent oscillations in the membrane signal.

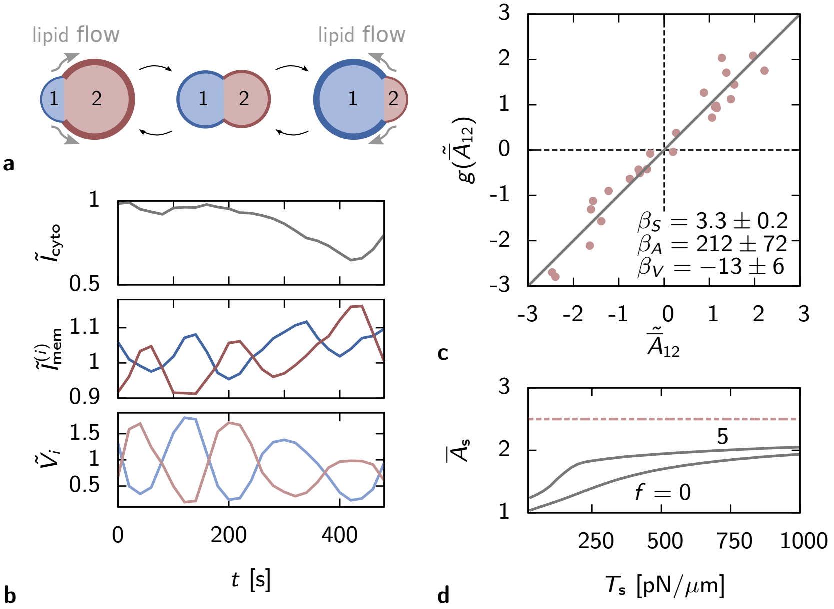

Figure 4.6 | **Membrane flow across the cleavage furrow. a** shows a schematic of the cell pole oscillations and the evolution of lipid intensity in the membrane (thickness circular boundaries). Colors as in **b** where experimental data of a L929 mouse fibroblast cell during cytokinesis is shown. Data obtained by stack analysis with a confocal microscope. Plotted is the time evolution of the total intensity of lipids in the cytoplasm (top) and in each pole membrane (middle), as well as the volume of each pole (bottom). All data is normalized by the initial symmetric values, intensities are corrected for bleaching [Data provided by Ortrud Wartlick, University College London]. **c** visualizes the fit result of the linearized flow equation (4.34) by plotting $g(\tilde{\bar{A}}_{12}) := -\beta_S \tilde{S}_{12} + \beta_A \partial_t \tilde{A}_{12} + \beta V \partial_t \tilde{V}_{12} \overset{!}{=} \tilde{\bar{A}}_{12}$ over $\tilde{\bar{A}}_{12}$, fit parameters with standard errors as stated in the plot, red dots data with $\tilde{A}_i = \tilde{I}^{(i)}_{\text{mem}}$, gray solid line theory. **d** Numerical solution of (4.36) for $\beta_S = 3$ and for two different filament pushing forces f (in pN/μm). Other parameters chosen as: $S_s = 750.7\,\mu\text{m}^2$ (from data), $N_p = 1900$, $\kappa = 20\,K_B\mathcal{T}$, $C_0 = 0$.

ne areas is of the order of 10 %. At the same time the total lipid intensity in the cytoplasm remains constant within an oscillation period (Figure 4.6b top), indicating that endocytosis and exocytosis seem to have a minor effect on the observed oscillations in membrane intensity. In contrast, on timescales of several oscillations, the cytoplasmic lipid intensity shows a significant decrease, associated to an increase of exocytosis. This could be a response of the cell to an overall membrane shortness and tension increase that cannot be buffered sufficently by the flow through the cleavage furrow.

We propose here that the observed flow of membrane through the cleavage furrow is directly triggered by a difference in surface tensions of the two pole membranes γ_1 and γ_2. This approach is comparable to our considerations from section 3.4 where we introduced a flow equation between membrane protrusions triggered by a relative difference of membrane surface tension. For a dividing cell with two cell poles this translates to the following linear flow ansatz:

$$\frac{\alpha'}{A_\mathrm{s}}\frac{dA_1}{dt} = -\frac{\alpha'}{A_\mathrm{s}}\frac{dA_2}{dt} \equiv \frac{\alpha'}{2}\frac{d\tilde{A}_{12}}{dt} = \gamma_{12}, \tag{4.32}$$

where α' is a friction coefficient, A_s the pole membrane area in case of symmetric poles, $\gamma_{12} := \gamma_1 - \gamma_2$ and $\tilde{A}_{12} := (A_1 - A_2)/A_\mathrm{s}$. Since the surface tensions in (4.32) depend on the membrane area A_i, pressure difference Δp_i and apparent surface area S_i the flow equation (4.32) is a differential equation for A_i. Moreover, it depends via S_i and Δp_i on (4.29). On the other hand, (4.29) depends via the force balance (4.6) on the membrane tensions. Hence, (4.29) and (4.32) form a coupled system of differential equations for the time evolution of the geometrical state of the dividing cell, *i.e.*, for the membrane area distribution and the pole volumes. Both are determined by the mechanical state given by Δp_i and γ_i in each pole.

We can use the ansatz (4.32) to compare our membrane model, based on a collection of protrusions (see section 4.1), with experimental data. In order to do so we linearize the surface tensions on the right-hand side of (4.32) around the symmetric pole state:

$$\gamma_{12} \approx \overline{A}\frac{\partial\gamma}{\partial\overline{A}}\bigg|_{\mathrm{sym}}\tilde{\overline{A}}_{12} + S\,\frac{\partial\gamma}{\partial S}\bigg|_{\mathrm{sym}}\tilde{S}_{12} + \frac{\partial\gamma}{\partial\Delta p}\bigg|_{\mathrm{sym}}\Delta p_{12}, \tag{4.33}$$

where the derivatives are evaluated at the symmetry values, $\tilde{\overline{A}}_{12} := (\overline{A}_1 - \overline{A}_2)/\overline{A}_{\mathrm{s}}$, $\tilde{S}_{12} := (S_1 - S_2)/S_{\mathrm{s}}$ and the excess area in the form $\overline{A}_i := \Omega_i + 1 \equiv A_i/S_i$. We expand γ in terms of the excess area, instead of the membrane area A itself, because we think that the amount of membrane in excess drives membrane flow rather than the absolute area. Moreover, the analytical expression of γ for spherical caps (see (3.17) on page 75) takes the simplest form for the variable set $\overline{A}$, S and Δp. The point force f does not enter the expansion (4.33) because we assume that it is, in good approximation, independent of the myosin concentration and thus remains constant in each cell pole. In a next step we replace the occurring pressure difference Δp_{12} by (4.29) and divide by the prefactor in front of $\tilde{\overline{A}}_{12}$ in (4.33). Hence, the flow equation (4.33) can be written in the linearized form

$$\tilde{\overline{A}}_{12} = -\beta_S\tilde{S}_{12} + \beta_A\frac{d\tilde{A}_{12}}{dt} + \beta_V\frac{d\tilde{V}_{12}}{dt} \tag{4.34}$$

with

$$\beta_S := \frac{S}{\overline{A}}\frac{\partial_S\gamma}{\partial_{\overline{A}}\gamma}\bigg|_{\mathrm{sym}}, \quad \beta_A = \frac{\alpha'}{2\overline{A}}\frac{1}{\partial_{\overline{A}}\gamma}\bigg|_{\mathrm{sym}}, \quad \beta_V = \frac{\alpha}{2\overline{A}}\frac{\partial_{\Delta p}\gamma}{\partial_{\overline{A}}\gamma}\bigg|_{\mathrm{sym}}. \tag{4.35}$$

By assuming that the measured total membrane intensities (Figure 4.6b) are proportional to the membrane areas, we can conclude that the quantities normalized by their symmetric values are identical, *i.e.*, $\tilde{A}_i = \tilde{I}^{(i)}_{\mathrm{mem}}$. Then we can plug into (4.34) the measured experimental data, namely the apparent pole areas, the pole volumes and the membrane intensities, and apply a multidimensional least square fit to obtain the parameters β_S, β_A and β_V. The result for the example cell in Figure 4.6b is shown in Figure 4.6c. The obtained errors for β_A and β_V are with 34 % and 46 %, respectively, relatively large. This could be due to the fact that the experimental data does not provide enough oscillations. Also the number of data points per oscillation is with nine relatively small. However, we can draw two preliminary conclusions from the fit result. First, we find that the terms related to $\tilde{S}_{12}$ and $\tilde{\overline{A}}_{12}$ in (4.34) cancel each other in good approximation, meaning that the membrane buckling is predominantly determined by the change of apparent surface area (section 4.4.1). This is in agreement with the small area flow across the cleavage furrow, discussed above. Hence, (4.34) roughly simplifies to $\tilde{A}_{12} \sim \tilde{V}_{12}$.

The second conclusion from the fit is related to the result for β_S. Since this parameter does not depend on the friction coefficients α and α' it can directly be related to our membrane model from section 4.1. We can numerically evaluate the derivatives of the surface tension $\gamma(\overline{A}, S, \Delta p, f)$ (see Figure 3.5 on 75) with respect to S and $\overline{A}$ and then solve

$$\beta_S = \frac{S}{\overline{A}} \frac{\partial_S \gamma}{\partial_{\overline{A}} \gamma}\bigg|_{\mathrm{sym}} \quad \Rightarrow \quad \overline{A}_{\mathrm{s}} = \overline{A}_{\mathrm{s}}(T_{\mathrm{s}}, S_{\mathrm{s}}, f, \beta_S) \overset{T_{\mathrm{s}} \to \infty}{\propto} \frac{2\beta_S - 1}{\beta_S - 1} \qquad (4.36)$$

for the membrane excess area $\overline{A}_{\mathrm{s}}$ in the symmetric pole state. The dependency of γ on the pressure difference Δp is replaced by the cortex tension T via the force balance (4.6). The resulting excess area is plotted as a function of T_{s} in Figure 4.6d. It increases from $\overline{A}_{\mathrm{s}} \approx 1$ at $T_{\mathrm{s}} = 0$ to $\overline{A}_{\mathrm{s}} \approx 2$ for typical tensions in the cell cortex ($T_{\mathrm{s}} \sim 500\,\mathrm{pN}/\mu\mathrm{m}$, see section 1.1.1). In the limit of $T_{\mathrm{s}} \to \infty$ the excess area converges to $\overline{A}_{\mathrm{s}} = 2.5$, which is the analytical result in (4.36) for a membrane consisting of spherical caps.

The estimated range for the membrane excess area in the symmetric case suggests that a large part of the extra membrane needed to cover the expanding cell pole can be provided by this initial excess. We can estimate the value of the minimal excess area required for the observed cell pole deformations from the typical magnitude of the pole area expansions. This is of the order of $50\,\%$ [26]. Subtracting $10\,\%$ provided by lipid flow through the cleavage furrow, a remaining $40\,\%$ must be buffered by unfolding initially buckled membrane. Hence, we have $\overline{A}_\mathrm{s} \gtrsim 1.4$ which agrees with our estimate in Figure 4.6d.

In future work we want to compare the estimated values for the membrane excess to a quantitative analysis of membrane out-of-plane structures during cell pole oscillations, observed with electron microscopy pictures as shown in Figure 1.6 on page 40. In this context we also want to further investigate the role of membrane tubes (microvilli) initiated by cortical filaments ($f > 0$) which occur during pole oscillations. So far we only included small pushing forces to the surface tension in (4.36). These are, however, not large enough to induce such membrane tubes (see section 3.2.4).

4.4.3 | Membrane buckling as a contribution for cell elasticity during cytokinesis

Via (4.29) the buckling of membrane, which, as we argue, is driven by cell pole oscillations, could itself feedback onto these oscillations. This is because Δp_{12} depends on the lateral membrane tensions $\gamma_{\|_1}$ and $\gamma_{\|_2}$ as introduced in (4.6). These tensions, in turn, depend on the buckling state of the membrane and the present pressure difference. In general, Δp_{12} can then only be determined implicitly. We derive here an explicit expression by linearizing $\gamma_{\|_i}$ in a similar way as the surface tension γ_i in the previous section. In principle, also $\gamma_{\|_i}$

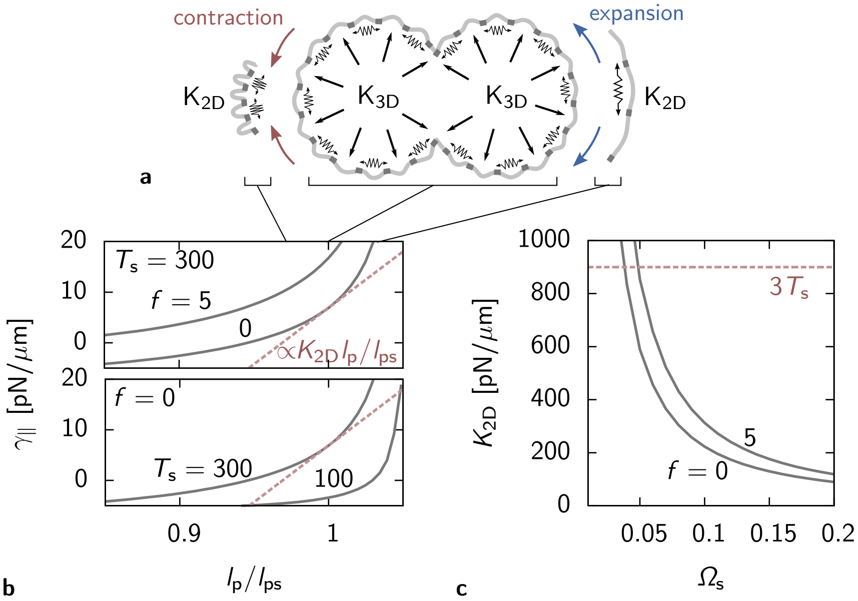

Figure 4.7 | **Surface elasticity caused by membrane buckling.** **a** illustrates the folding of the anchored membrane caused by pole contractions and expansions. **b** shows the lateral tension $\gamma_{\|}$ as a function of the anchoring mesh size $\xi \equiv l$ (gray solid lines) for two different cortex tensions T_s (in pN/μm, bottom plot) and two different filament forces f (in pN, top plot). The mesh size is normalized by $l_{ps} = 2\sqrt{S_s/\pi N_p} \approx 0.7\,\mu$m, where $S_s \approx 750.7\,\mu\text{m}^2$ is taken from the cell data used for Figure 4.6. The membrane area is constant and chosen as $A_s = 1.1\,S_s$. The red dashed line indicates the linear expansion around l_{ps}. **c** shows the surface elasticity K_{2D} as a function of the initial excess area $\Omega_s = A_s/S_s$ for $T_s = 300\,\text{pN}/\mu\text{m}$ and two different forces (pN). The red dashed line indicates condition (4.41). For both **b** and **c** we used the full numerical data from chapter 3. $\kappa = 20\,K_B T$, $C_0 = 0$ and $f = 0$.

depends on the three quantities membrane area A_i, apparent pole area S_i and pressure difference Δp_i. However, the dependency on A_i we ignore here due to the relatively small membrane flow through the cleavage furrow which implies $A_1 \approx A_2$. The pressure difference only causes a renormalization of the friction coefficient α in (4.29) so that the only dependency we include is that of S_i. We express it in terms of a change of the mesh size $\xi_i \equiv l_{\mathrm{p}_i}$ (Figure 4.7b). Plugging this into the force balance (4.6) we find for Δp_{12} of (4.29) the approximation

$$\Delta p_{12} \approx 2\left[\frac{T_1+\gamma_{\|\mathrm{s}}}{R_1}-\frac{T_2+\gamma_{\|\mathrm{s}}}{R_2}\right]+\frac{K_{2\mathrm{D}}}{R_{\mathrm{s}} l_{\mathrm{p}_{\mathrm{s}}}}\left(l_{\mathrm{p}_1}-l_{\mathrm{p}_2}\right). \tag{4.37}$$

Here $\gamma_{\|\mathrm{s}}$ is the lateral tension in the symmetric state and

$$K_{2\mathrm{D}} := l_{\mathrm{p}} \left.\frac{\partial \gamma_{\|}}{\partial l_{\mathrm{p}}}\right|_{\mathrm{sym}} \tag{4.38}$$

plays the role of a surface elasticity due to the buckling of membrane. It is plotted in Figure 4.7c. By relating, in linear order, the change of the mesh sizes to the change of volumes of the spherical portions we can rewrite (4.37) to

$$\Delta p_{12} \approx \Delta p_{\mathrm{Laplace}}+\frac{K_{3\mathrm{D}}}{V_{\mathrm{s}}}\left(V_1-V_2\right). \tag{4.39}$$

With this we can deduce the following constitutive expression for the bulk elasticity $K_{3\mathrm{D}}$, which originally has been introduced as a generic cell property in (1.2) on page 27 [26]:

$$K_{3\mathrm{D}}=\frac{K_{2\mathrm{D}}}{3R_{\mathrm{s}}}\left[1-4\frac{R_{\mathrm{c}}^2}{l_{\mathrm{p}_{\mathrm{s}}}^2 N_{\mathrm{p}}}\right]\left[1+8\frac{R_{\mathrm{c}}^2}{l_{\mathrm{p}_{\mathrm{s}}}^2 N_{\mathrm{p}}}\right] \overset{R_{\mathrm{c}}\to 0}{\propto} \frac{K_{2\mathrm{D}}}{3R_{\mathrm{s}}}. \tag{4.40}$$

Qualitatively, this result suggests that the bulk elasticity found for cells during cytokinesis is, at least partly, generated by the surface elasticity coming from the buckling of the cell membrane. To estimate the contribution quantitatively we can compare (4.40) with the characteristic value of $K_{3\mathrm{D}}$ needed to stabilize cell division. According to (1.4) on page 28 this is the case if $K_{3\mathrm{D}} \approx T_{\mathrm{s}}/R_{\mathrm{s}}$. That is, with (4.40) the condition

$$K_{\mathrm{2D}} \overset{!}{\approx} 3\,T_{\mathrm{s}} \tag{4.41}$$

must be satisfied so that the buckling elasticity can have an impact on the stabilization of cell division. For reasonable cell parameters (Figure 4.7c) we find that K_{2D} can, indeed, be of the right order of magnitude, if the excess area in the symmetric pole state is $\Omega_{\mathrm{s}} \approx 0.005$. This is smaller than the excess area we estimated in the previous section. Thus, a further investigation is needed to verify the buckling of membrane in the symmetric state of oscillating cells. As pointed out in the previous section, the quantification of electron microscopy images will help to clarify this. On top of that, the impact of membrane tubes on K_{2D}, which occur for $f \gg 1$, needs to be explored further.

However, already the fact that we find the membrane to be able to generate a sufficiently large elastic response under certain conditions is striking as the cell membrane is usually regarded as relatively flexible ($\kappa = 20\,\mathrm{k_B}\mathcal{T}$). The reason for such a strong elastic response is the buckling on relatively small length scales of less than a micrometer. This shows that membrane buckling is not only triggered by the volume change but can, in principle, also feedback to the volume change. In this spirit, the discussed membrane behavior during cytokinesis is a demonstrative example for the coupled mechanics of cell membrane and cortex, introduced by our self-consistent description in section 4.2.1.

CONCLUSIONS AND OUTLOOK 5

With the work presented in the last chapters we provide a relatively simple theoretical description of the interplay between cell membrane and cortex. For the actual anchoring of the membrane to the cortex we introduced two different approaches. One treated the membrane as a relatively flat sheet attached via discrete anchoring points to a square lattice. The other treated the membrane as a collection of axisymmetric protrusions also arranged on a square lattice. These approaches allowed us to relate the buckling of the anchored membrane to its shape and, via its surface tension, to its mechanical state. Interestingly, we found that the description in the weak-bending approximation is neglecting significant terms for the surface tension of the membrane, indicating that this approximation, often used in previous work, could be inappropriate for a mechanical analysis of the membrane. For our work this became important because only with the full description we could predict bleb formation due to membrane flow, as reported earlier [155]. With this finding and a further analysis of bleb formation due to a local detachment from the cortex, the analysis of invaginated membrane tubes and the analysis of filament induced extrusion of microvilli we found shape diagrams which determine the conditions under which these structures should occur in cells.

We used our results for the mechanics of a buckled, anchored membrane to propose a closed system of equations for the interplay of cell membrane and cortex. It enables us to relate subcellular properties of the cell to global cell properties. Most importantly, we can relate the contractility of the cell cortex, generated by active motor proteins, to the equilibrium radius of the cell, the cell pressure difference compared to the outside, the membrane surface tension and to the shape of the anchored membrane. A striking result of this new description is that the membrane is buckling, *i.e.*, it is not tightly attached to the cortex, as usually assumed in the past, but is naturally deformed into small bulges, even in absence of curvature modulating proteins. This buckling is induced by the contractility in the cortex. Moreover, local expansions and contractions of the cortex can trigger a redistribution of membrane area among the bulges, leading to a further enhancement of the buckling in the contracted and a depletion in the expanded parts. We studied this phenomenon for dividing cells that exhibit persistent cell pole oscillations. We demonstrated how the membrane area redistribution is self-regulated by the membrane as it equilibrates its surface tension by membrane flow through the cleavage furrow of the dividing cell. Furthermore, we showed that the change of buckling during the redistribution gives rise to an effective elastic response of the membrane, due to the change of curvature energy, large enough to have a significant impact on the overall cell elasticity. These findings give, on the one hand, a new insight into how mechanics regulate the membrane, in particular, the buffering of fast occurring excess area. On the other hand, they suggest that the membrane not only reacts to other (actively driven) mechanical processes inside the cell but could itself feedback mechanically through its buckling state.

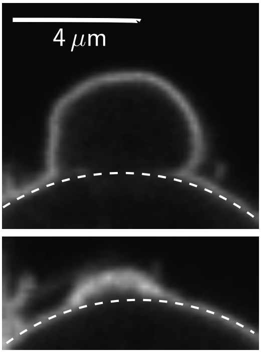

Figure 5.1 | Membrane buckling during bleb retraction. The images show a bleb of a L929 mouse fibroblast cell during cytokinesis, immediately after formation (top) and at the end of retraction (bottom). The images have been taken with a confocal microscope. The intensity is proportional to the used membrane marker CAAX. The dashed line indicates the position of the cell cortex. [Raw images provided by Andrea Pereira, University College London.]

Further applications to cell biology

In chapter 4 we already discussed some connections between our theoretical findings and experimental observations. We estimated the critical force needed to detach the membrane from the contractile actin meshwork of a novel *in-planevitro* vesicle. Furthermore, by introducing a flow equation for the lipid exchange through the cleavage furrow of a dividing cell we could give a first quantitative explanation for the fast membrane area redistribution observed with confocal microscopy for cell pole oscillations during cytokinesis. In a next step, three more applications would be especially interesting. The first application would be related to the retraction of blebs. We think that this can be modeled with the same dynamic ansatz as the cell pole oscillations of a dividing cell (see section 1.2 and [26]) because it is also driven by a contraction of the reassembling cortex inside the bleb. Interestingly, also an enhanced buckling of the membrane can be observed (see Figure 5.1), indicating that here the elasticity in the model could have the same origin as we propose for the pole oscillations. The second application would be related to the composition of membrane into buds and microvilli. Preliminary observations with electron microscopy suggest that this composition is changing during one period of the cell pole oscillation, more precisely,

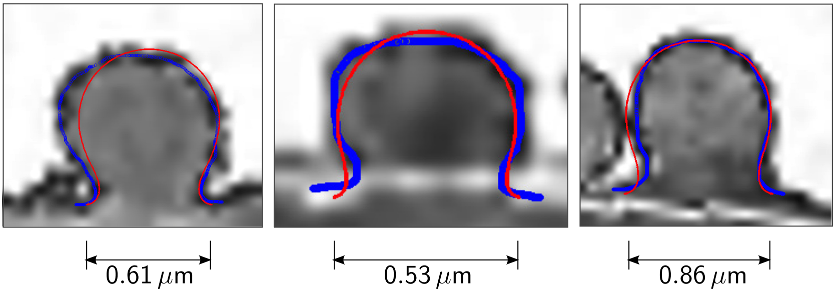

Figure 5.2 | Experimentally measured membrane protrusions fitted by theoretical shapes. Overlaid are the experimental contour lines (blue) and the contour obtained by a theoretical fit (red) on top of images taken by an electron microscope. Same cell type as in Figure 5.1. [Raw images provided by Ortrud Wartlick, University College London.]

the fraction of tubes covering the cell is varying. We should be able, in principle, to localize the position of these cells within our shape diagrams and, thus, explain this variation. A third application, which we recently started to explore, uses single protrusion images (Figure 5.2), also obtained from electron microscopy, to fit their contour line by the contour of our theoretical shapes from section 3.2[1]. As we fix the bending rigidity ($\kappa = 20\,k_\mathrm{B}\mathcal{T}$), we can estimate the surface area A_p of the protrusion and the pressure difference Δp from the fit. Therewith, we can calculate the surface tension γ and the lateral tension $\gamma_{||}$ of the membrane. The results could be compared, for instance, with separate measurements of Δp and γ.

Possible extensions of the presented concepts

In order to perform more quantitative comparisons with experimental observations it might be necessary to further extend our theoretical concepts and thus make the modeling more realistic. We think

---

[1] Similar studies have been reported recently for endosome formation [206].

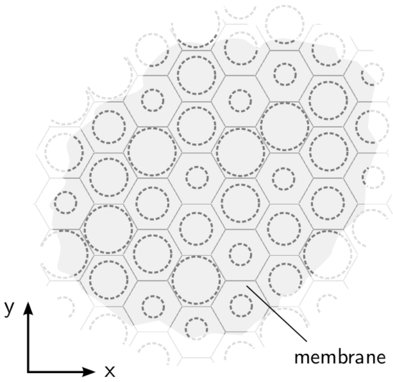

Figure 5.3 | Membrane sheet bound to a hexagonal lattice. The dashed circles illustrate the basal area of membrane protrusions, here with different diameters.

for future work especially two such extensions would be important, namely to consider integral membrane proteins and a heterogeneous anchoring mesh. The latter could be implemented by keeping the introduced square lattice at fixed mesh size ξ but to allow each protrusion to have a different basal diameter $l_{\mathrm{p}_{nm}}$, as illustrated in Figure 5.3. As a consequence of this heterogeneity, in equilibrium, each protrusion would carry a different excess area what could give rise to new interesting shape states. Similarly, also integral proteins could modify the distribution of excess area. Reason for this is their prohibited diffusion across the anchoring sites, in contrast to lipid diffusion. This would lead to unbalanced protein concentrations among protrusions and could induce an entropic tension that modifies the actual surface tension.

On top of this, a few further extensions could be considered for our work. For example, protrusions without axial symmetry could be included. To account for the spherical geometry of the cell, their boundary condition at the base could be changed as (compare to conditions (3.2) on page 63)

$$\psi(0) = 0 \quad \rightarrow \quad \psi(0) = \arcsin \frac{l}{2R}. \tag{5.1}$$

Furthermore, instead of a square lattice, a hexagonal lattice, as illustrated in Figure 5.3, would fit more accurately to an axisymmetric protrusion. Finally, in addition to the flow equation, the effect of endocytosis and exocytosis for the membrane description during cell pole oscillations could be included by separate equations, modeling the lipid exchange between membrane and cytoplasm.

A very interesting theoretical aspect, which we faced througout our work, however, did not study any further until now, is to understand the underlying mechanisms for the formation and persistence of the anchoring lattice. We argued along the line of the fences model, introduced in the past [59, 66], *i.e.*, that the characteristic mesh size is determined by the meshwork size of the cell cortex. However, this remains a hypothesis. An experimental analysis of this would be interesting. Another approach, which could lead to a different mesh size than the one purely dictated by the cortex, would involve a minimization of the membrane energy $\mathcal{F}$ also with respect to the linker diameter. According to its definition (3.19) on page 76, the lateral tension is always zero then and the minimization returns an additional relation (see derivation of the shape equations in appendix B.3)

$$\delta\rho(0) \neq 0 \quad \Rightarrow \quad l = l(A, \Delta p, f). \tag{5.2}$$

Independently of how the lattice size is determined, in either case another important question is how it is maintained. This question is relevant because on long enough timescales the viscous properties of the cortex dominate (see section 1.1.1), suggesting that then membrane anchors can slide in lateral direction. The consecutive question is whether a homogeneous structuring of the membrane into protrusion can then be stable at all. This can be checked in the same way as the stability of a homogeneous area distribution. Following the derivation of (3.29) on page 84, the stability of the anchoring lattice is defined by the derivative[2]

$$\frac{\partial \gamma_{\|}}{\partial l} > 0 \quad \Rightarrow \quad \text{stable homogeneous lattice.} \tag{5.3}$$

Otherwise a small perturbation would lead to a contineous growth of one protrusion base until, eventually, the entire membrane is mostly detached from the cortex. As Figure 4.7b on page 121 shows, according to our membrane model a positive slope of $\gamma_{\|}(l)$ is possible, indicating that the protrusion structure is stable even on timescales where the cortex becomes viscous.

---

[2] Note that here the sign is the opposite to the sign for the membrane flow because a locally larger lateral tension tends to reduce the respective protrusion diameter.

APPENDIX A

DIFFERENTIAL GEOMETRY OF SURFACES

Differential geometry is the mathematical framework which describes the geometrical shape of any n-dimensional object [210]. It is used for *coordinate transformations* between different coordinate systems suitable for different geometries, mostly in the context of curved spaces or surfaces.

The main concepts of differential geometry can be seen as a generalization of what is known from linear algebra and vector analysis. An arbitrary vector $\mathbf{a}$ can be expressed by basis vectors $\mathbf{g}_i$ as [210][1]:

$$\mathbf{a} = a^i \, \mathbf{g}_i, \tag{A.1}$$

where a^i are the components of $\mathbf{a}$. Here the components and basis vectors are defined *locally*, *i.e.*, they depend on the spatial position. Furthermore, the basis vectors are in general not normalized and not orthogonal. In cartesian coordinates, where $\mathbf{g}_i$ is equal to the cartesian unit vector $\mathbf{e}_i$, they form a constant orthonormal basis. The scalar product of two vectors $\mathbf{a}$ and $\mathbf{b}$

$$\mathbf{a} \cdot \mathbf{b} = a^i b^j \mathbf{g}_i \cdot \mathbf{g}_j \equiv a^i b^j g_{ij} \tag{A.2}$$

---

[1] Here *Einstein's summation convention* $\sum_i a_i b^i \equiv a_i b^i$ is used.

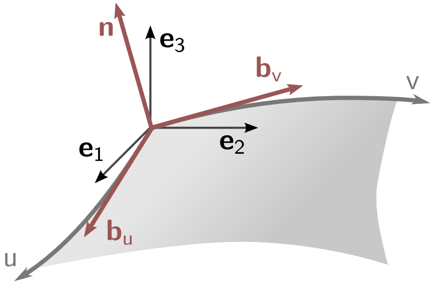

Figure A.1 | **Schematic of a parameterized curved surface.** $\mathbf{b}_u$ and $\mathbf{b}_v$ are the tangential vectors, $\mathbf{n}$ the normal vector. $\mathbf{e}_i$ are the cartesian unit vectors.

defines the *metric* or *metric tensor* g_{ij}. It determines the geometry, *i.e.*, the distances and angles in the coordinate space. The metric is symmetric and becomes diagonal for orthogonal coordinate systems. For the cartesian coordinate system g_{ij} is equal to the *Kronecker symbol* δ_{ij}. Either the metric or the scalar product itself are also called the *first fundamental form* of differential geometry.

Often the first fundamental form is defined via the squared *line element*

$$ds^2 \equiv \mathbf{dr} \cdot \mathbf{dr} = g_{ij} dx^i dx^j. \tag{A.3}$$

It provides a relatively simple way to compute the transformation behavior of the metric under a change of coordinates since any infinitesimal coordinate displacement can be expressed in new coordinates with the help of the total differential. It follows:

$$ds^2 = g_{ij} dx^i dx^j = g_{ij} \frac{\partial x^i}{\partial x'^n} \frac{\partial x^j}{\partial x'^m} dx'^n dx'^m \equiv g'_{nm} dx'^n dx'^m, \tag{A.4}$$

where the prime denotes the new coordinates. According to (A.4) the basis transformation reads

$$\mathbf{g}'_i = \frac{\partial x^i}{\partial x'^j} \mathbf{g}_j. \tag{A.5}$$

The basis vectors tangential to the coordinate lines are then defined by

$$\mathbf{b}_i = \frac{\partial \mathbf{r}}{\partial x'^i}, \tag{A.6}$$

where $\mathbf{r}$ is the position vector.

The position of a surface in a three-dimensional space is characterized by two independent parameters, *e.g.*, $x'^1 = u$ and $x'^2 = v$ [120, 211]. In this case the vectors $\mathbf{b}_1$ and $\mathbf{b}_2$ are tangential to this surface in each point (Figure A.1) and define locally a *tangential plane*. A third independent basis vector is the *normal vector*

$$\mathbf{n} = \frac{\mathbf{b}_1 \times \mathbf{b}_2}{\|\mathbf{b}_1 \times \mathbf{b}_2\|} \tag{A.7}$$

with the norm $\|\mathbf{a}\| := \sqrt{\mathbf{a} \cdot \mathbf{a}}$.

With the basis vectors $\mathbf{b}_1$, $\mathbf{b}_2$, $\mathbf{n}$ several geometric quantities of a two-dimensional curved surface can be calculated. A first important is the infinitesimal area element. As known from algebra the norm of the cross-product of two vectors is equal to the area of the rhombus spanned by the two vectors. Hence, the area element is given by

$$\mathbf{dA} = \mathbf{b}_1 \times \mathbf{b}_2 \, dx^1 dx^2 = \mathbf{n} \, dA = \mathbf{n}\sqrt{g} \, dx^1 dx^2, \tag{A.8}$$

where $g := \det g_{ij}$ is the determinant of the metric tensor, which is here generated by the two tangential vectors and has thus four components[2]. A similar argument as for area element and cross-product holds for the infinitesimal volume element and the triple product. The latter sets the volume of a rhombohedron spanned by three vectors. Hence, the volume element reads as follows:

$$dV = \|\mathbf{b}_3 \cdot (\mathbf{b}_1 \times \mathbf{b}_2)\| dx^1 dx^2 dx^3. \tag{A.9}$$

---

[2] Following (A.5), g_{ij} should carry here a prime, which is, however, neglected for simplicity.

A third important geometrical quantity is the curvature of the surface. It can be defined as the second spatial derivative of the position vector $\mathbf{r}$. In two dimensions this is summarized in the *curvature tensor*

$$C^i_j = -\mathbf{n} \cdot g'^{ik} \frac{\partial}{\partial x'^j} \frac{\partial}{\partial x'^k} \mathbf{r} \,, \tag{A.10}$$

where g'^{ik} is the dual or conjugate metric to g'_{ik}. Both are coupled to each other via the relation $g'_{in} g'^{nk} = \delta^k_i$. That is, g'^{ik} is the inverse of g'_{ik}.

The curvature tensor (A.10) can also be interpreted as a measure for how much the tangential plane in a certain point is changing its orientation in a small vicinity. Therefore, the curvature tensor gives rise to two principal axes on the surface, which correspond to the two invariant scalar *principal curvatures* C_1 and C_2. A more natural choice for such a pair of curvature invariants is given by the *mean curvature* H and *Gaussian curvature* $\mathcal{K}$, because they can directly be extracted from C^i_j by its trace $2H = \operatorname{tr} C^i_j$ and determinant $K = \det C^i_j$, respectively. Due to this and the fact that C^i_j is symmetric, each pair can be calculated by the other via the relations $H = (C_1 + C_2)/2$ and $K = C_1 C_2$.

APPENDIX

VARIATIONAL PRINCIPLE AND THE SHAPE EQUATIONS

B

B.1 | Variation calculus

With the *calculus of variation* extrema of *functionals*, which depend on variables that themselves depend on space or time, can be calculated. The *variation* of the functional G, which depends on the function $f(\xi)$, where ξ is a not further specified set of variables, is defined as [140, 212]

$$\delta G[f] := \lim_{\delta f \to 0} \left\{ G[f + \delta f] - G[f] \right\}. \tag{B.1}$$

The functional is the equivalent to the differential or more precisely the *total differential* of a function, depending on a number of variables [212]. It can be shown that the functional obeys a generalized relation of the total differential

$$\delta G[f] = \int d\xi \frac{\delta G}{\delta f} \delta f \tag{B.2}$$

or if G depends on several functions as

$$\delta G[f_1, f_2, \dots] = \int d\xi \left\{ \frac{\delta G}{\delta f_1} \delta f_1 + \frac{\delta G}{\delta f_2} \delta f_2 + \dots \right\}. \tag{B.3}$$

Relations (B.2) and (B.3) act as a definition for the *functional derivative* $\delta G/\delta f$. As in basic analysis the vanishing of the functional derivative is a necessary condition for finding extrema. However, here the extrema are functions instead of single parameters. That is why the functional derivative leads, in principle, to a differential equation, from which the extremal function can be determined.

If the function G appears in the form

$$G[f_1, f_2, \dots] = \int d\xi \, \mathcal{L}[f_1, f_2, \dots]. \tag{B.4}$$

the variation of G leads directly to a variation of the integrant $\mathcal{L}$, which can be expanded up to linear order in $\delta f_1, \delta f_2, \dots$. If G also depends on derivatives of $f_1, f_2, \dots$, a partial integration is necessary in order to bring the variation in the form (B.4). The occurring boundary terms have to vanish identically. This is either automatically guaranteed by existing boundary conditions or leads to additional boundary conditions. The resulting expressions for the functional derivatives are called *Euler-Lagrange equations* as they are set to zero.

In the following the variational principle is used to calculate the shape equations for a membrane, described by the energy (see also (1.6) on page 30)

$$\mathcal{F} = \frac{\kappa}{2} \oint dA (2H - C_0)^2 + \gamma \Xi - \Delta p \int dV - f \int dL \tag{B.5}$$

with

$$\Xi := \begin{cases} \oint dA & \gamma = \text{const.}, \\ \oint dA - A & A = \text{const.} \end{cases} \tag{B.6}$$

Two special parameterizations are used for the variation, the *Monge parameterization* and the *arc length parameterization.* For the first, the force term in (B.5) will be neglected ($f = 0$).

B.2 | Shape equations in Monge parameterization

The Monge parameterization describes the position of a two-dimensional surface by a height function h with respect to a reference plane. The two special cases, used in this work, are the cartesian reference frame $(h(x,y))$ and a cylindrical reference plane $(h(\rho,\varphi))$. A schematic illustration can be found in Figure 1.5a on page 35.

Monge parameterization $h(x,y)$

In order to derive the shape equations expressed by $h(x,y)$, first, the area element dA, the volume element dV and the mean curvature H in the energy (B.5) need to be rewritten explicitly. An overview of their explicit expressions is given in Table B.1 at the end of this section. The energy can then be written as[1]

$$\mathcal{F} = \int dx\, dy\, \mathcal{L}(h, h_{|x}, h_{|y}, h_{|xy}, h_{|xx}, h_{|yy}) \tag{B.7}$$

with

$$\begin{aligned} \mathcal{L} = &- \Delta p\, h + \gamma \sqrt{g} \\ &+ \frac{\kappa}{2} \sqrt{g} \left(\frac{2 h_{|x} h_{|y} h_{|xy} - h_{|xx} g^{(y)} - h_{|yy} g^{(x)}}{\sqrt{g}^3} - C_0 \right)^2 . \end{aligned} \tag{B.8}$$

The used notation $h_{|x} := \frac{\partial h}{\partial x}$ is used for simplicity. From (B.7) the variation $\delta\mathcal{F}$ (B.1) yields

$$\begin{aligned} \delta\mathcal{F} = \int dxdy \Bigg[&\frac{\partial \mathcal{L}}{\partial h} \delta h + \frac{\partial \mathcal{L}}{\partial h_{|x}} \delta h_{|x} + \frac{\partial \mathcal{L}}{\partial h_{|y}} \delta h_{|y} \\ &+ \frac{\partial \mathcal{L}}{\partial h_{|xy}} \delta h_{|xy} + \frac{\partial \mathcal{L}}{\partial h_{|xx}} \delta h_{|xx} + \frac{\partial \mathcal{L}}{\partial h_{|yy}} \delta h_{|yy} \Bigg] . \end{aligned} \tag{B.9}$$

---

[1] Here and in the following the constant energy term $-\gamma A$, which might occur according to (B.5) for a constant surface area, is skipped.

By interchanging the partial with the functional derivative, $\delta h_{|x} = \partial_x \delta h$, (B.9) can be rewritten with the help of partial integrations in such a way that all bulk terms contain the variation δh:

$$
\begin{aligned}
\delta\mathcal{F} = \int dx\, dy\, \Bigg[& \frac{\partial\mathcal{L}}{\partial h} - \frac{\partial}{\partial x}\frac{\partial\mathcal{L}}{\partial h_{|x}} - \frac{\partial}{\partial y}\frac{\partial\mathcal{L}}{\partial h_{|y}} \\
& + \frac{\partial^2}{\partial x\partial y}\frac{\partial^2\mathcal{L}}{\partial h_{|xy}} + \frac{\partial^2}{\partial x^2}\frac{\partial^2\mathcal{L}}{\partial h_{|xx}} + \frac{\partial^2}{\partial y^2}\frac{\partial^2\mathcal{L}}{\partial h_{|yy}} \Bigg] \delta h \\
& + \int dx \left[\frac{\partial\mathcal{L}}{\partial h_{|y}} - \frac{\partial}{\partial y}\frac{\partial\mathcal{L}}{\partial h_{|yy}} - \frac{\partial}{\partial y}\frac{\partial\mathcal{L}}{\partial h_{|xy}} \right] \delta h \Bigg|_{y_1}^{y_2} \\
& + \int dy \left[\frac{\partial\mathcal{L}}{\partial h_{|x}} - \frac{\partial}{\partial x}\frac{\partial\mathcal{L}}{\partial h_{|xx}} - \frac{\partial}{\partial x}\frac{\partial\mathcal{L}}{\partial h_{|xy}} \right] \delta h \Bigg|_{x_1}^{x_2} \\
& + \int dx \left[\frac{\partial\mathcal{L}}{\partial h_{|yy}} \right] \delta h_{|y} \Bigg|_{y_1}^{y_2} + \int dy \left[\frac{\partial\mathcal{L}}{\partial h_{|xx}} \right] \delta h_{|x} \Bigg|_{x_1}^{x_2} \\
& + \left. \frac{\partial\mathcal{L}}{\partial h_{|xy}\delta h} \right|_{x_1,y_1} + \left. \frac{\partial\mathcal{L}}{\partial h_{|xy}\delta h} \right|_{x_2,y_2} \\
& - \left. \frac{\partial\mathcal{L}}{\partial h_{|xy}\delta h} \right|_{x_1,y_2} - \left. \frac{\partial\mathcal{L}}{\partial h_{|xy}\delta h} \right|_{x_2,y_1} .
\end{aligned}
\tag{B.10}
$$

The boundary terms in the Monge parameterization can often immediately be neglected due to periodic boundary conditions. In this case the values of $h(x, y)$ and its derivatives will be equal at the boundaries $x = x_1$ and $x = x_2$ and $y = y_1$ and $y = y_2$, respectively. The integrand $\mathcal{L}$ will then also take the same values there and the boundary terms cancel each other. The bulk term in (B.10) leads for $\delta\mathcal{F} \overset{!}{=} 0$ to the Euler-Lagrange equation for the specific problem (B.7). The full evaluation for the given $\mathcal{L}$ in (B.10) leads to a relatively complicated nonlinear partial differential equation for the equilibrium shape. A simpler expression of the shape equation can be obtained with the help of the *weak-bending approximation*, where $\partial h/\partial x \approx \partial h/\partial y \approx 0$. A more detailed explanation is provided in paragraph 1.3.3 on page 34. With this approximation the integrand (B.8) can be expanded up to the first nontrivial order:

$$\begin{aligned}\mathcal{L} \approx &(\gamma + \frac{\kappa}{2}C_0^2 - \Delta p\, h) + C_0\kappa\left(h_{|xx} + h_{|yy}\right)\\ &+ \frac{\kappa}{2}\left(h_{|xx}^2 + h_{|yy}^2 + 2h_{|xx}h_{|yy}\right)\\ &+ \frac{1}{2}\left(\gamma + \frac{\kappa}{2}C_0^2\right)\left(h_{|x}^2 + h_{|y}^2\right).\end{aligned} \tag{B.11}$$

Computing the bulk term of (B.10) based on (B.11) leads to the shape equation in weak bending approximation:

$$\triangle_{\|}^2 h(x,y) - \frac{\gamma^*}{\kappa}\triangle_{\|} h(x,y) = \frac{\Delta p}{\kappa} \tag{B.12}$$

with

$$\gamma^* := \gamma + \frac{\kappa}{2}C_0^2. \tag{B.13}$$

Monge parameterization $h(\rho)$

In general, an equivalent choice for the height function $h(x,y)$ is the height function $h(\rho,\varphi)$ with the cylindrical coordinates ρ and φ. Especially for disc-like membrane sheets it has advantages compared to the cartesian Monge parameterization. This becomes most obvious for the special case where this disc has axial symmetry. Then the cylindrical Monge parameterization simplifies to an effective one-dimensional problem described by $h(\rho)$.

Also for the axisymmetric case with $h(\rho)$ the geometrical quantities are summarized in Table B.1 at the end of this section. The energy (B.5) then reads as

$$\mathcal{F} = 2\pi \int d\rho \, \mathcal{L}(\rho; h, h_{|\rho}, h_{|\rho\rho}) \tag{B.14}$$

with

$$\begin{aligned}\mathcal{L} =& -\Delta p \, \rho \, h + \gamma \rho \sqrt{g} \\ &+ \frac{\kappa}{2} \rho \sqrt{g} \left(\frac{\rho h_{|\rho\rho} + h_{|\rho}^3 + h_{|\rho}}{\rho \sqrt{g}^3} + C_0 \right)^2 .\end{aligned} \tag{B.15}$$

The variation follows as

$$\begin{aligned}\delta\mathcal{F} =& 2\pi \int d\rho \left[\frac{\partial \mathcal{L}}{\partial h} - \frac{d}{d\rho} \frac{\partial \mathcal{L}}{\partial h_{|\rho}} + \frac{d^2}{d\rho^2} \frac{\partial \mathcal{L}}{\partial h_{|\rho\rho}} \right] \delta h \\ &+ \frac{\partial \mathcal{L}}{\partial h_{|\rho}} \delta h \bigg|_{\rho_1}^{\rho_2} + \frac{\partial \mathcal{L}}{\partial h_{|\rho\rho}} \delta h_{|\rho} \bigg|_{\rho_1}^{\rho_2} - \frac{d}{d\rho} \frac{\partial \mathcal{L}}{\partial h_{|\rho\rho}} \delta h \bigg|_{\rho_1}^{\rho_2} .\end{aligned} \tag{B.16}$$

For this work the boundary terms are negligible due to the imposed boundary conditions imposed. The shape equation, obtained from the bulk term, reads as

$$f_h^{(1)} + \gamma \, f_h^{(2)} = 0 \tag{B.17}$$

with

$$\begin{aligned}f_h^{(1)} =& \frac{\kappa}{2\rho^2 \sqrt{g}^9} \left[h_{|\rho} \left(1 - \rho^2 C_0^2\right) g^4 \right. \\ &+ \left(h_{|\rho} + \rho h_{|\rho\rho} - \rho^3 C_0^2 h_{|\rho\rho} \right) g^3 \\ &+ \rho \left(-3 h_{|\rho\rho} + 4\rho h_{|\rho\rho\rho} + 2\rho^2 h_{|\rho\rho\rho\rho} \right) g^2 \\ &- 4\rho^2 C_0 h_{|\rho} h_{|\rho\rho} \sqrt{g}^5 \\ &+ 5\rho^2 h_{|\rho\rho} \left(6\rho h_{|\rho\rho}^2 - 3 h_{|\rho} h_{|\rho\rho} - 4\rho h_{|\rho} h_{|\rho\rho\rho} \right) g\end{aligned}$$

$$-35\rho^3 h^3_{|\rho\rho}\Big] - \Delta p \rho,$$

$$f_h^{(2)} = -\,\frac{\left(g\,h_{|\rho} + \rho\,h_{|\rho\rho}\right)}{\sqrt{g}^3}. \tag{B.18}$$

Also here the weak-bending approximation $dh/d\rho \approx 0$ can be used to linearize the shape equations. The integrand (B.15) becomes then

$$\begin{aligned} L \approx{}& \frac{\rho}{2}\left(C_0^2\kappa + \kappa h_{\rho\rho}\left(2C_0 + h_{|\rho\rho}\right) + 2\gamma\right) - \Delta p\,\rho\,h \\ &+ \frac{h^2_{|\rho}}{4\rho}\left(C_0^2\kappa\rho^2 + 2\kappa + 2\rho^2\gamma\right) + \kappa h_\rho\left(C_0 + h_{|\rho\rho}\right) \end{aligned} \tag{B.19}$$

and, thus, the shape equation

$$\begin{aligned} &\kappa\left(\frac{1}{\rho^2} - \frac{\gamma}{\kappa}\right) h_{|\rho} - \kappa\rho\left(\frac{1}{\rho^2} + \frac{\gamma}{\kappa}\right) h_{|\rho\rho} \\ &\qquad\qquad + 2\kappa h_{|\rho\rho\rho} + \kappa\rho h_{|\rho\rho\rho\rho} = \Delta p \rho. \end{aligned} \tag{B.20}$$

B.3 | Shape equations in arc length parameterization

The Monge parameterization $h(\rho)$, discussed in the previous section, cannot be used for surfaces with height gradients above an angle of $\pi/2$ as then uniqueness of the height function is violated. In these cases the arc length parameterization can be used instead. It allows for arbitrary height gradients and can for axial symmetry. The used parameters are the arc length s along the *contour line* of the surface (see Figure 1.5b on 35) and the polar angle φ. The corresponding coordinate transformation for axisymmetric surfaces and the resulting geometrical quantities are listed in Table B.1 at the end of this section. They yet contain two shape functions $\rho(s)$ and $h(s)$. They can be replaced by a single shape function $\psi(s)$ via the following relations:

$$\frac{\partial \rho}{\partial s} = -\cos\psi, \quad \frac{\partial h}{\partial s} = \sin\psi. \tag{B.21}$$

$\psi(s)$ is the tilt angle between the tangent of the contour line and the ρ-axis. Due to these two relations, as discussed in section 1.3.3, the energy (B.5) needs to be extended by two Lagrange terms in order to ensure that the relations are conserved while the variation is performed. Thus the energy reads as

$$\mathcal{F}^* = \mathcal{F} + \mu(s)\left(\frac{\partial \rho}{\partial s} + \cos\psi\right) + \nu(s)\left(\frac{\partial h}{\partial s} - \sin\psi\right) \tag{B.22}$$

with $\mu(s)$ and $\nu(s)$ being two Lagrange multiplier. Using the angle ψ changes the area element, volume element and mean curvature from Table B.1 in the following way:

$$\begin{aligned} dA &= \rho\, d\varphi\, ds, \\ dV &= \rho\, d\varphi\, d\rho\, ds \sin\psi, \\ H &= \frac{1}{2}\left(\frac{\sin\psi}{\rho} - \psi_{|s}\right). \end{aligned} \tag{B.23}$$

The energy (B.22) then deduces to

$$\mathcal{F}^* = 2\pi \int ds \mathcal{L}(\psi, \psi_{|s}, \rho, \rho_{|s}, h, h_{|s}, \mu, \nu) \tag{B.24}$$

with

$$\begin{aligned} \mathcal{L} =& \frac{1}{2}\kappa\rho\left(\frac{\sin\psi}{\rho} - \psi_{|s} - C_0\right)^2 - \frac{1}{2}\Delta p\, \rho^2 \sin\psi + \gamma\rho \\ &+ \mu\left(\rho_{|s} + \cos\psi\right) + \nu\left(h_{|s} - \sin\psi\right) - \frac{f}{2\pi}\sin\psi. \end{aligned} \tag{B.25}$$

Here a new term, compared to the two integrands (B.8) and (B.15) from the previous sections, appears, associated with the point force

f. It arises from the term fL of the energy (B.5) which was not considered before. L is the elevation of the membrane above a fixed ground at the position where the perpendicular point force f is applied. For axisymmetric membranes the direction of this point force is collinear to the z-axis of the coordinate system and from the second relation of (B.21) the elevation can be deduced to

$$L \equiv h(s_2) - h(s_1) = \int_{s_1}^{s_2} ds \sin\psi. \tag{B.26}$$

The contour length Λ of the contour line, which is parameterized by the arc length, is in general not fixed. Therefore, it must be part of the variation $\delta\mathcal{F}^*$. One way to realize this, as reported in [148], is to directly include the integral boundaries s_1 and s_2 to the variation. An equivalent realization, used here, uses a normalized arc length u, normalized by the contour length as $u := 2s/\Lambda$. If furthermore the integral boundaries are chosen such that $s_1 = 0$ the following transformation rules apply:

$$\int_0^{\frac{\Lambda}{2}} ds \to \int_0^1 \frac{\Lambda}{2} du, \quad \frac{d}{ds} \to \frac{2}{\Lambda}\frac{d}{du}, \quad \mathcal{L} \to \mathcal{L}^* = \frac{\Lambda}{2}\mathcal{L}. \tag{B.27}$$

As Λ does not depend on u the variation of $\mathcal{F}^*$ with respect to Λ is simply given by the derivative

$$\frac{\partial\mathcal{F}^*}{\partial\Lambda} = 2\pi\int_0^1 du \frac{\partial\mathcal{L}^*}{\partial\Lambda}. \tag{B.28}$$

The variation of $\mathcal{F}^*$ is then given by

$$\begin{aligned}\delta\mathcal{F}^* = 2\pi\int_0^1 du \Bigg[&\left\{\frac{\partial\mathcal{L}^*}{\partial\psi} - \frac{d}{du}\frac{\partial\mathcal{L}^*}{\partial\psi_{|u}}\right\}\delta\psi + \left\{\frac{\partial\mathcal{L}^*}{\partial\rho} - \frac{d}{du}\frac{\partial\mathcal{L}^*}{\partial\rho_{|u}}\right\}\delta\rho \\ &+ \left\{\frac{\partial\mathcal{L}^*}{\partial h} - \frac{d}{du}\frac{\partial\mathcal{L}^*}{\partial h_{|u}}\right\}\delta h + \frac{\partial\mathcal{L}^*}{\partial\eta}\delta\eta + \frac{\partial\mathcal{L}^*}{\partial\nu}\delta\nu + 2\frac{\partial\mathcal{L}^*}{\partial\Lambda}\Bigg]\end{aligned}$$

$$+\frac{\partial\mathcal{L}^*}{\partial\psi_{|u}}\delta\psi\bigg|_0^1+\frac{\partial\mathcal{L}^*}{\partial\rho_{|s}}\delta\rho\bigg|_0^1+\frac{\partial\mathcal{L}^*}{\partial h_{|s}}\delta h\bigg|_0^1. \tag{B.29}$$

Evaluating the bulk terms of (B.29) leads to the following set of shape equations:

$$\begin{aligned}
0 =& -\Delta p\Lambda\rho^2\cos\psi-\frac{8\kappa}{\Lambda}\rho\psi_{|uu}+\kappa\Lambda\frac{\sin 2\psi}{\rho}\\
&+\frac{1}{\pi}\left(4\pi\kappa\psi_{|u}-f\Lambda-2\Lambda\pi\nu\right)\cos\psi-2\Lambda\mu\sin\psi, && \text{(B.30)}\\
0 =& \,2\gamma\Lambda+C_0^2\kappa\Lambda+4C_0\kappa\,\psi_{|u}-2\Delta p\Lambda\rho\sin\psi\\
&-\kappa\Lambda\frac{\sin^2\psi}{\rho^2}+\frac{4\kappa}{\Lambda}\psi_{|u}^2-4\mu_{|u}, && \text{(B.31)}\\
0 =& \,\nu_{|u}, && \text{(B.32)}\\
0 =& \,\frac{\Lambda}{2}\cos\psi+\rho_{|u}, && \text{(B.33)}\\
0 =& -\frac{\Lambda}{2}\sin\psi+h_{|u}, && \text{(B.34)}\\
0 =& \,2\pi\int_0^1 du\left[\rho\left(2\gamma+C_0^2\kappa-\frac{4\kappa}{\Lambda^2}\psi_{|u}^2\right)\right.\\
&-2C_0\kappa\sin\psi-\frac{f}{\pi}\sin\psi-\Delta p\rho^2\sin\psi\\
&\left.+\kappa\frac{\sin^2\psi}{\rho}+2\mu\cos\psi-2\nu\sin\psi\right]. && \text{(B.35)}
\end{aligned}$$

Note that the integrand of the last equation, or equivalently of (B.28), has a special meaning, as pointed out in [148]. It can be shown that

$$2\frac{\partial\mathcal{L}^*}{\partial\Lambda}\equiv-\mathcal{H}^* \tag{B.36}$$

with the *Hamilton function*

$$\mathcal{H}^*=-\mathcal{L}^*+\psi_{|u}\frac{\partial\mathcal{L}^*}{\partial\psi_{|u}}+\rho_{|u}\frac{\partial\mathcal{L}^*}{\partial\rho_{|u}}+h_{|u}\frac{\partial\mathcal{L}^*}{\partial h_{|u}}. \tag{B.37}$$

Arc length parameterization for smooth boundary conditions

In this work the arc length parameterization is used to describe axisymmetric membrane protrusions as shown in Figure 3.1 on page 62. They have a fixed basal diameter l and are subject to *smooth boundary conditions* which read according to (3.2) on page 63 as

$$\begin{gathered} h(u=0)=0, \quad \rho(u=0)=l/2, \quad \rho(u=1)=0, \\ \psi(u=0)=\psi(u=1)=0. \end{gathered} \tag{B.38}$$

From this the boundary terms in (B.29) (or rewritten for u as in (1.24) on page 38) can be evaluated immediately. The variations $\delta\psi$ and $\delta\rho$ vanish at both ends and, hence, the boundary terms as well. However, δh only vanishes for $u=0$. This gives rise to an additional boundary condition for ν:

$$\left.\frac{\partial\mathcal{L}^*}{\partial h_{|u}}\right|_{u=1} = \nu(u=1) = 0. \tag{B.39}$$

With this and (B.38) there are six conditions for six integration constants, arising from the integration of the shape equations (B.30) – (B.35).

Having the boundary conditions (B.38) and (B.39), three shape equations can be solved immediately. From (B.32) ν deduces to

$$\nu(s)=0. \tag{B.40}$$

With the help of (B.33) and (B.34), which are equivalent to the imposed relations (B.21), expressions for ρ and h can be found:

$$\rho(u)=\frac{l}{2}-\frac{\Lambda}{2}\int_0^u du'\cos\psi(u'), \tag{B.41}$$

$$h(u)=\frac{\Lambda}{2}\int_0^u du'\sin\psi(u'). \tag{B.42}$$

The remaining three shape equations need to be solved simultaneously, in principle, as they are coupled with each other. This requires the help of numerical methods as they are not solvable analytically. The method, used in this work, is discussed in appendix D. For this method it is convenient to reformulate these three equations. Firstly, (B.33) can be integrated once and then be written as

$$\mu(u) = \gamma\frac{\Lambda}{2}u + \mu_{\text{int}}(u) + \mu_0 \tag{B.43}$$

with

$$\begin{aligned}\mu_{\text{int}}(u) := \frac{1}{4}\int_0^u du' \Big[C_0\kappa\left(4\psi_{|u'} + \Lambda C_0\right) - 2\Delta p\Lambda\rho\sin\psi \\ -\kappa\Lambda\frac{\sin^2\psi}{\rho^2} + \frac{4\kappa}{\Lambda}\psi_{|u'}^2\Big]\end{aligned} \tag{B.44}$$

and μ_0 being an integration constant. This constant is set by the second boundary condition for the radius $\rho(1) = 0$. With the help of (B.41) this can be translated to the condition

$$l = \Lambda\int_0^1 du\cos\psi. \tag{B.45}$$

Finally, with (B.43) μ can be replaced in the two other equations (B.30) and (B.35), which then become

$$0 = f_\psi^{(1)} + \gamma f_\psi^{(2)} + \mu_0 f_\psi^{(3)}, \tag{B.46}$$

$$0 = f_\Lambda^{(1)} + \gamma f_\Lambda^{(2)} + \mu_0 f_\Lambda^{(3)} \tag{B.47}$$

with

$$f_\psi^{(1)} = \frac{\left(4\pi\kappa\psi_{|u} - f\Lambda\right)}{\pi}\cos\psi - \Delta p\Lambda\rho^2\cos\psi$$

$$
\begin{aligned}
&- \frac{8\kappa}{\Lambda}\rho\,\psi_{|uu} + \kappa\Lambda\frac{\sin 2\psi}{\rho} - 2\Lambda\mu_{\text{int}}\sin\psi,\\
f_{\psi}^{(2)} =& - \Lambda^2 u\sin\psi,\\
f_{\psi}^{(3)} =& - 2\Lambda\sin\psi,\\
f_{\Lambda}^{(1)} =& \frac{1}{2}\int_0^1 du\left[C_0^2\kappa\rho - \frac{(2\pi C_0\kappa + f)}{\pi}\sin\psi - \Delta p\rho^2\sin\psi\right.\\
&\left. - \frac{4\kappa}{\Lambda^2}\rho\psi_{|u}^2 + \kappa\frac{\sin^2\psi}{\rho} + 2\mu_{\text{int}}\cos\psi\right],\\
f_{\Lambda}^{(2)} =& \int_0^1 du\left[\rho + \frac{\Lambda}{2}u\cos\psi\right],\\
f_{\Lambda}^{(3)} =& \int_0^1 du\cos\psi. \qquad \text{(B.48)}
\end{aligned}
$$

Solving (B.41), (B.46) and (B.47) simultaneously under the condition (B.45) gives the equilibrium shape of an axisymmetric membrane area with smooth boundary conditions, described by the energy (B.5). Note that $f_{\psi}^{(1)}$, $f_{\psi}^{(2)}$ and $f_{\psi}^{(3)}$ are still functions of u whereas $f_{\Lambda}^{(1)}$, $f_{\Lambda}^{(2)}$ and $f_{\Lambda}^{(3)}$ are independent of u due to the integration. Also note that here the surface tension γ is treated as an independent parameter. In section 3.1 and elsewhere in this work γ is determined by an additional constraint besides (B.45), arising from an imposed surface area A:

$$\text{const.} \equiv A = \pi\Lambda\int_0^1 du\,\rho\,. \qquad \text{(B.49)}$$

Table B.1 | Geometrical quantities expressed in special parameterizations. The coordinate order for the curvature tensor follows the order of appearance of the tangential vectors.

Cartesian Monge parameterization

coordinate transformation

$$x = u, \quad y = v, \quad z = h(u,v) \equiv h(x,y)$$

basis vectors

$$\mathbf{b}_x = \begin{pmatrix} 1 \\ 0 \\ h_{|x} \end{pmatrix}, \quad \mathbf{b}_y = \begin{pmatrix} 0 \\ 1 \\ h_{|y} \end{pmatrix}, \quad \mathbf{n} = \tfrac{1}{\sqrt{g}} \begin{pmatrix} -h_{|x} \\ -h_{|y} \\ 1 \end{pmatrix}$$

area element

$$dA = \sqrt{g}\, dx\, dy \quad \text{with} \quad g = 1 + h_{|x}^2 + h_{|y}^2$$

volume element

$$dV = h\, dx\, dy$$

curvature tensor

$$C^i_{\ j} = -\tfrac{1}{\sqrt{g}^3} \begin{pmatrix} (g - h_{|x}^2)h_{|xx} - h_{|x}h_{|y}h_{|xy} & (g - h_{|y}^2)h_{|xy} - h_{|x}h_{|y}h_{|xx} \\ (g - h_{|x}^2)h_{|xy} - h_{|x}h_{|y}h_{|yy} & (g - h_{|y}^2)h_{|yy} - h_{|x}h_{|y}h_{|xy} \end{pmatrix}$$

mean curvature

$$H = \tfrac{1}{2\sqrt{g}^3} \left(2h_{|x}\, h_{|y}\, h_{|xy} - h_{|xx}\, (g - h_{|x}^2) - h_{|yy}\, (g - h_{|y}^2) \right)$$

Cylindrical Monge parameterization with axisymmetry

coordinate transformation

$$x = \rho \cos\varphi, \quad y = \rho \sin\varphi, \quad z = h(\rho)$$

basis vectors

$$\mathbf{b}_\rho = \begin{pmatrix} \cos\varphi \\ \sin\varphi \\ h_{|\rho} \end{pmatrix}, \quad \mathbf{b}_\varphi = \begin{pmatrix} -\rho\sin\varphi \\ \rho\cos\varphi \\ 0 \end{pmatrix}, \quad \mathbf{n} = \tfrac{1}{\sqrt{g}} \begin{pmatrix} -\cos\varphi\, h_{|\rho} \\ -\sin\varphi\, h_{|\rho} \\ 1 \end{pmatrix}$$

area element

$$dA = \sqrt{g}\, d\varphi\, d\rho \quad \text{with} \quad g = \rho^2 (1 + h_{|\rho}^2)$$

volume element

$$dV = \rho\, d\varphi\, d\rho\, dh$$

curvature tensor

$$C^i_{\ j} = -\tfrac{1}{\sqrt{g}^3} \begin{pmatrix} \rho^3\, h_{|\rho\rho} & 0 \\ 0 & g\, h_{|\rho} \end{pmatrix}$$

mean curvature

$$H = \tfrac{1}{2\sqrt{g}^3} \left(g\, h_{|\rho} + \rho\, h_{|\rho\rho} \right)$$

Arc length parameterization with axisymmetry

coordinate transformation

$$x = \rho(s) \cos\varphi, \quad y = \rho(s) \sin\varphi, \quad z = h(s), \quad h_{|s}^2 + \rho_{|s}^2 = 1$$

basis vectors

$$\mathbf{b}_\varphi = \begin{pmatrix} -\rho \sin\varphi \\ \rho \cos\varphi \\ 0 \end{pmatrix}, \quad \mathbf{b}_s = \begin{pmatrix} \rho_{|s} \cos\varphi \\ \rho_{|s} \sin\varphi \\ h_{|s} \end{pmatrix}, \quad \mathbf{n} = \begin{pmatrix} h_{|s} \cos\varphi \\ h_{|s} \sin\varphi \\ -\rho_{|s} \end{pmatrix}$$

area element

$$dA = \rho\, d\varphi\, ds$$

volume element

$$dV = \rho\, d\varphi\, d\rho\, ds\, h_{|s}$$

curvature tensor

$$C^i_{\ j} = \begin{pmatrix} \rho^{-1} h_{|s} & 0 \\ 0 & \rho_{|s} h_{|ss} - \rho_{|ss} h_{|s} \end{pmatrix}$$

mean curvature

$$H = \tfrac{1}{2\rho} \left(\rho \rho_{|s} h_{|ss} + h_{|s} \left(-\rho \rho_{|ss} + 1 \right) \right)$$

APPENDIX

DERIVATION OF THE ANCHORED MEMBRANE SHEET SOLUTION

C

A special solution of the differential equation

$$\overline{\mathfrak{L}}\,\overline{h} = \overline{Q}, \tag{C.1}$$

where $\overline{\mathfrak{L}}$ is a differential operator and $\overline{Q}$ a inhomogeneity, can be computed from the associated *fundamental solution*[1]. This fundamental solution solves the reduced equation [182, 183]

$$\overline{\mathfrak{L}}\,\overline{h}_{\mathrm{f}} = \delta, \tag{C.2}$$

where δ is Dirac's delta distribution. The solution $\overline{h}$ is then given by the convolution of $\overline{h}_{\mathrm{f}}$ with $\overline{Q}$.

The fundamental solution can be computed with the help of the Fourier transformation. Applying it to (C.2) leads to an algebraic equation if the coefficients of $\overline{\mathfrak{L}}$ are constant. This equation can be then be solved for the unknown fundamental solution, which is finally obtained after evaluating the inverse Fourier transformation.

Let now $\overline{\mathfrak{L}}$ be the differential operator found in the shape equation of appendix B.2 on weakly undulated membrane sheets[2]:

---

[1] Often the fundamental solution is also called *Green's function*.

$$\overline{\mathfrak{L}} = \overline{\triangle_{\|}}^2 - \overline{\gamma}^* \overline{\triangle_{\|}} \tag{C.3}$$

and $\overline{h}$ the height profile of the sheet[3]. Furthermore, the two-dimensional Fourier transformation shall be defined in this work in the following way:

$$\overline{h}(\overline{x},\overline{y}) = \frac{1}{2\pi}\int d^2\overline{k}\,\hat{\overline{h}}(\overline{k}_x,\overline{k}_y)\,e^{\mathrm{i}\overline{\mathbf{k}}\cdot\overline{\mathbf{r}}}, \tag{C.4}$$

$$\hat{\overline{h}}(\overline{k}_x,\overline{k}_y) = \frac{1}{2\pi}\int d^2\overline{r}\,\overline{h}(\overline{x},\overline{y})\,e^{-\mathrm{i}\overline{\mathbf{k}}\cdot\overline{\mathbf{r}}}. \tag{C.5}$$

The corresponding fundamental solution can then be written as

$$\overline{h}_{\mathrm{f}}(x,y) = \frac{1}{(2\pi)^2}\int d^2\overline{k}\,\frac{e^{\mathrm{i}\overline{\mathbf{k}}\cdot\overline{\mathbf{r}}}}{\overline{k}^4 + \overline{\gamma}^*\overline{k}^2}, \tag{C.6}$$

where $\overline{k} \equiv \|\overline{\mathbf{k}}\|$ is the absolute value of the wave number vector. In many cases integrals of this type can be evaluated with the help of the *residue theorem*. However, for this work this is not explicitly necessary. Instead the full solution, given by convolution

$$\overline{h}(\overline{x},\overline{y}) = (\overline{Q} * \overline{h}_{\mathrm{f}})(\overline{x},\overline{y}) \tag{C.7}$$

$$\equiv \int d^2\overline{r}'\overline{Q}(x',y')\,\overline{h}_{\mathrm{f}}(\overline{x}-\overline{x}',\overline{y}-\overline{y}'), \tag{C.8}$$

is rewritten with the help of (C.6) to

$$\overline{h}(\overline{x},\overline{y}) = \frac{1}{2\pi}\int d^2\overline{k}\frac{\hat{\overline{Q}}(\overline{k}_x,\overline{k}_y)}{\overline{k}^4 + \overline{\gamma}^*\overline{k}^2}e^{\mathrm{i}\overline{\mathbf{k}}\cdot\overline{\mathbf{r}}}. \tag{C.9}$$

---

[2] See also (B.12) for comparison.

[3] We use in this section the normalizations as introduced in section 3.1: $\overline{\Delta p} := \frac{\xi^3}{\kappa}\Delta p$, $\overline{f} := \frac{\xi}{\kappa} f$ $\overline{C}_0 := \xi\, C_0$, $\overline{\gamma}^* := \frac{\xi^2}{\kappa}\gamma^*$, $\overline{\mathcal{F}} := \mathcal{F}/\kappa$.

This relation states that the Fourier transform of $\overline{h}(\overline{x},\overline{y})$ is equivalent to

$$\hat{\overline{h}}(\overline{k}_x,\overline{k}_y) \equiv \frac{\hat{\overline{Q}}(\overline{k}_x,\overline{k}_y)}{\overline{k}^4 + \overline{\gamma}^* \overline{k}^2}. \tag{C.10}$$

The result (C.10) can now be used to compute $\overline{h}(\overline{x},\overline{y})$ for the special inhomogeneity introduced in section 2.1 for a periodically anchored membrane (see (2.5) on page 48):

$$\overline{Q}(\overline{x},\overline{y}) = \overline{\Delta p} + \sum_{s=0}^{2q} \overline{f}_{\mathrm{a}}^{(s)} \sum_{n,m} \overline{G}_{mn;s} \tag{C.11}$$

with $\overline{G}_{mn;s}$ as in (2.2) on page 47:

$$\overline{G}_{mn;s} = \delta(\overline{x} - n - \overline{x}_s)\delta(\overline{y} - m - \overline{y}_s). \tag{C.12}$$

According to our definitions (C.4) and (C.5), the Fourier transformation of $\overline{Q}$ reads then as

$$\begin{aligned}\hat{\overline{Q}}(\overline{k}_x,\overline{k}_y) = 2\pi \Bigg[&\sum_{s=0}^{2q} \overline{f}_{\mathrm{a}}^{(s)} \, e^{-\mathrm{i}\mathbf{k}\cdot\overline{\mathbf{r}}_s} \sum_{n,m} \delta(\overline{k}_x - 2\pi n)\delta(\overline{k}_y - 2\pi m) \\ &+ \overline{\Delta p}\,\delta(\overline{k}_x)\delta(\overline{k}_y) \Bigg]. \end{aligned} \tag{C.13}$$

Evaluating the inverse transformation of (C.10) is then straight forward as every term contains a δ-distribution, which allows a direct evaluation of the Fourier integral. The only careful treatment is required for the δ-distribution at zeroth mode $\overline{k}_x = \overline{k}_y = 0$ as this would, in principle, lead to a divergent integral. However, here the relevant terms can be suppressed by ensuring the following condition:

$$\overline{\Delta p} + \sum_{s=0}^{2q} \overline{f}_{\mathrm{a}}^{(s)} \overset{!}{=} 0. \tag{C.14}$$

A physical interpretation of this relation is given in section 2.2.

If (C.14) is guaranteed, the Fourier transformation (C.4) of $\hat{h}$ can be evaluated:

$$\begin{aligned}\overline{h}(\overline{x},\overline{y}) &= \sum_{s=0}^{2q} \overline{f}_{\mathrm{a}}^{(s)} \int d^2\overline{k} \frac{e^{\mathrm{i}\overline{\mathbf{k}}\cdot(\overline{\mathbf{r}}-\overline{\mathbf{r}}_s)}}{\overline{k}^4 + \overline{\gamma}^* \overline{k}^2} \\ &\qquad \cdot \sum_{\substack{n,m \\ n=m\neq 0}} \delta(\overline{k}_x - 2\pi n)\delta(\overline{k}_y - 2\pi m) \\ &= \frac{1}{16\kappa\pi^4} \sum_{s=0}^{2q} \overline{f}_{\mathrm{a}}^{(s)} \sum_{\substack{n,m \\ n=m\neq 0}} \frac{e^{\mathrm{i}2\pi n(\overline{x}-\overline{x}_s)} e^{\mathrm{i}2\pi m(\overline{y}-\overline{y}_s)}}{(n^2+m^2)^2 + \frac{\overline{\gamma}^*}{4\pi^2}(n^2+m^2)} \\ &= \sum_{s=0}^{2q} \overline{f}_{\mathrm{a}}^{(s)} \overline{\Gamma}_{\overline{\gamma}^*}(\overline{x}-\overline{x}_s, \overline{y}-\overline{y}_s)\end{aligned} \tag{C.15}$$

with

$$\begin{aligned}\overline{\Gamma}_\alpha(\overline{x},\overline{y}) :=& \frac{1}{4\pi^4} \sum_{n,m\geq 1} \frac{\cos(2\pi n\overline{x})\cos(2\pi m\overline{y})}{(n^2+m^2)^2 + \frac{\alpha}{4\pi^2}(n^2+m^2)} \\ &+ \frac{1}{8\pi^4} \sum_{n\geq 1} \frac{\cos(2\pi n\overline{x}) + \cos(2\pi n\overline{y})}{n^4 + \frac{\alpha}{4\pi^2}n^2}.\end{aligned} \tag{C.16}$$

The remaining unknowns of (C.15) are the coefficients $\overline{f}_{\mathrm{a}}^{(s)}$, which have been introduced as resistive forces in section 2.1. In total there are $2q+1$ unknown coefficients. So equally many defining equations are needed to fully determine $\overline{h}(\overline{x},\overline{y})$. One of these conditions is the introduced relation (C.14). The others can be deduced by the fact that all anchoring points shall be localized at the same height. Hence, another $2q$ equations are defined by

$$\overline{h}(\overline{x}_0, \overline{y}_0) \overset{!}{=} \overline{h}(\overline{x}_1, \overline{y}_1) \overset{!}{=} \ldots \overset{!}{=} \overline{h}(\overline{x}_{2q+1}, \overline{y}_{2q+1}) \,. \tag{C.17}$$

Together with (C.14), equations (C.17) can be summarized into the following system of equations:

$$\begin{aligned}
\overline{\Delta p} &= \sum_0^{2q} \overline{f}_{\mathrm{a}}^{(s)}, \\
0 &= \sum_0^{2q} \left[\overline{\Gamma}_{\overline{\gamma}^*}(\overline{x}_1 - \overline{x}_s, \overline{y}_1 - \overline{y}_s) - \overline{\Gamma}_{\overline{\gamma}^*}(\overline{x}_0 - \overline{x}_s, \overline{y}_0 - \overline{y}_s)\right] \overline{f}_{\mathrm{a}}^{(s)}, \\
&\vdots \\
0 &= \sum_0^{2q} \left[\overline{\Gamma}_{\overline{\gamma}^*}(\overline{x}_{2q} - \overline{x}_s, \overline{y}_{2q} - \overline{y}_s) - \overline{\Gamma}_{\overline{\gamma}^*}(\overline{x}_0 - \overline{x}_s, \overline{y}_0 - \overline{y}_s)\right] \overline{f}_{\mathrm{a}}^{(s)}.
\end{aligned} \tag{C.18}$$

This can also be written in matrix form:

$$\sum_{s=0}^{2q} \overline{M}_{ls} \overline{f}_{\mathrm{a}}^{(s)} = \overline{N}_l, \tag{C.19}$$

where $\overline{M}$ is a square matrix with the entries

$$\overline{M}_{ls} = \begin{cases} 1 & \text{for } l = 0, \\ \overline{\Gamma}_{\overline{\gamma}^*}(\overline{x}_l - \overline{x}_s, \overline{y}_l - \overline{y}_s) & \\ \quad - \overline{\Gamma}_{\overline{\gamma}^*}(\overline{x}_0 - \overline{x}_s, \overline{y}_0 - \overline{y}_s) & \text{otherwise} \end{cases} \tag{C.20}$$

and $\overline{N}$ a vector with the entries:

$$\overline{N}_l = \begin{cases} -\overline{\Delta p} & \text{for } l = 0, \\ 0 & \text{otherwise.} \end{cases} \tag{C.21}$$

The system of equations (C.18) is solved as soon as the inverse matrix $\overline{M}^{-1}$ is found. This appears to be not manageable here as long as the number of anchors is unspecific. The anchor number needs to be set first.

What can be concluded from (C.18) is the explicit dependency of the coefficients $\overline{f}_{\mathrm{a}}^{(s)}$ on $\overline{\Delta p}$. This can be found by only taking a subsystem of (C.18), excluding the first equation. This subsystem is not complete as it consists of $2q$ equations for $2q+1$ unknowns. Nevertheless, since (C.18) is a linear system, $2q$ coefficients can be expressed by the one, which remains undetermined, *e.g.*, $\overline{f}_0$. In fact they are all proportional to $\overline{f}_0$, *i.e.*, $\overline{f}_1, \dots, \overline{f}_{2q} \sim \overline{f}_0$. Plugging this into the excluded first equation of (C.18) shows immediately that $\overline{\Delta p}$ is a linear prefactor of $\overline{f}_0$ and, hence, for all $\overline{f}_{\mathrm{a}}^{(s)}$. However, this does not mean that $\overline{f}_{\mathrm{a}}^{(s)} \sim \overline{\Delta p}$ as $\overline{f}_{\mathrm{a}}^{(s)}$ also depends on $\overline{\gamma}^*$, which itself can also depend on $\overline{\Delta p}$.

It should finally be mentioned that the system of equations (C.18) can be reduced to $q^* < 2q+1$ equations with

$$q^* = \begin{cases} \frac{q}{2} + 1 & \text{for } q \text{ even,} \\ \frac{q+1}{2} + 1 & \text{for } q \text{ odd.} \end{cases} \tag{C.22}$$

This is due to the symmetry of $\overline{\Gamma}_\alpha(\overline{x}, \overline{y})$, coming from the symmetry of the unit element introduced in section 2.1. The symmetry with respect to $\overline{x}$ and $\overline{y}$ reduces the number of independent equations by $-q$. The symmetry of the anchor arrangement with respect to each edge of the unit element reduces the number of independent equations by another $q/2$ or $(q-1)/2$, depending on whether q is even or odd.

Adjusting z-position of $h(x, y)$

As discussed, the solution $\overline{h}(\overline{x}, \overline{y})$ guarantees that all anchoring points are localized at the same z-position. However, the exact value is not further specified yet. Moreover, the position still depends on $\overline{\gamma}$ and the number of intermediate anchoring points ($q > 0$) as can be seen by computing $\overline{h}(0, 0)$ according to (C.15). In order to decouple the z-position of the anchors from the values of $\overline{\gamma}^*$ and q a suitable homogeneous solution $\overline{h}_0$ of the shape equation (2.5) on page 48 can be added to $\overline{h}$ (see the explanation at the beginning of section 2.2). Here it shall be choses as $\overline{h}_0 = \overline{h}(0, 0)$. The redefined height profile $\overline{h}(\overline{x}, \overline{y}) = \overline{h}_{\mathrm{old}} - \overline{h}_0$ is then given by

$$\overline{h}(\overline{x}, \overline{y}) = \sum_{s=0}^{2q} \overline{f}_{\mathrm{a}}^{(s)} \left[\overline{\Gamma}_{\overline{\gamma}^*}(\overline{x} - \overline{x}_s, \overline{y} - \overline{y}_s) - \overline{\Gamma}_{\overline{\gamma}^*}(\overline{x}_s, \overline{y}_s) \right] . \qquad \text{(C.23)}$$

From now on this expression is used instead of the previous definition (2.5).

Accuracy of the expanded solution

Although the result $\overline{h}(\overline{x}, \overline{y})$ is given in an exact analytical form, to our best knowledge there exists no exact expression of $\overline{\Gamma}_\alpha(\overline{x}, \overline{y})$ in terms of standard functions. It could be possible to find such an expression by solving the problem in one unit element only and construct the full sheet by piece-wise repetition of this solution in the other lattice elements. The challenging part here would be to impose proper boundary conditions in the single unit element.

Here (C.16) is seen as the defining relation for $\overline{\Gamma}_\alpha(\overline{x}, \overline{y})$ instead. In practice this limits the accuracy of $\overline{h}(\overline{x}, \overline{y})$ since only a finite number of summation terms can be taken into account for computations. In order to estimate the truncation error made by interrupting the

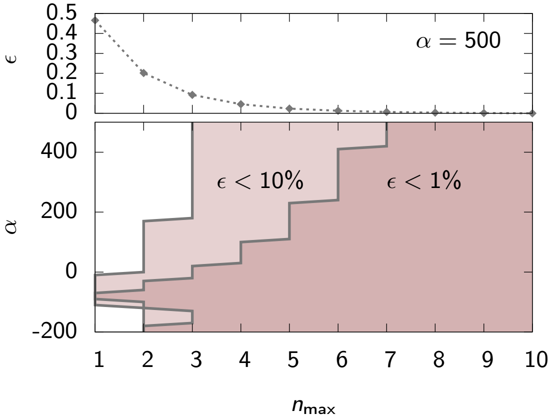

Figure C.1 | Truncation error of the function $\overline{\Gamma}_\alpha(\overline{x}, \overline{y})$. The upper plot shows the error (C.24) for one example value of α. The lower plot shows for different α the expansion order $n_{\max}$ needed to be taken into account to fall below an error of $\epsilon = 10\%$ and $\epsilon = 1\%$, respectively, with the expanded solution.

summation of both n and m in (C.16) at a maximum value $n_{\max}$ the following measure is used here:

$$\epsilon := \left| \frac{\langle \overline{\Gamma}_\alpha^2 \rangle_{n_{\max}} - \langle \overline{\Gamma}_\alpha^2 \rangle_\infty}{\langle \overline{\Gamma}_\alpha^2 \rangle_\infty} \right| \simeq \left| \frac{\langle \overline{\Gamma}_\alpha^2 \rangle_{n_{\max}} - \langle \overline{\Gamma}_\alpha^2 \rangle_{10}}{\langle \overline{\Gamma}_\alpha^2 \rangle_{10}} \right| \tag{C.24}$$

with

$$\langle \overline{\Gamma}_\alpha^2 \rangle_{n_{\max}} := \int_0^1 d\overline{x}\, d\overline{y}\, \overline{\Gamma}_\alpha(\overline{x}, \overline{y})^2. \tag{C.25}$$

The function $\langle \overline{\Gamma}_\alpha^2 \rangle$ is the continuous spatial average of $\overline{\Gamma}_\alpha^2$. That $\overline{\Gamma}_\alpha^2$ is taken here instead of $\overline{\Gamma}_\alpha$ itself is due to the fact that $\overline{\Gamma}_\alpha$ can become negative and thus also zero for certain values of α. This would lead to a divergence of the introduced error measure ϵ. The approximation $\langle \overline{\Gamma}_\alpha^2 \rangle_{10} \approx \langle \overline{\Gamma}_\alpha^2 \rangle_\infty$ appeared to be a reasonable choice as $\langle \overline{\Gamma}_\alpha^2 \rangle$ converged in good approximation to a constant value within this limit. A more accurate estimate of $\langle\overline{\Gamma}_\alpha^2\rangle_\infty$ could be achieved by using an (exponential) fit function for $\langle\overline{\Gamma}_\alpha^2\rangle_{n_{\max}}$.

The error measure (C.24) states how much the expanded solution differs from the converged solution. It decays with an increasing number of terms taken into account. Figure C.1 shows this for one example at $\alpha = 500$. In this case the error falls below 10% for an expansion order of $n_{\max} = 3$ and below 1% for $n_{\max} = 7$. This observation can be generalized for a range of values of α as shown in Figure C.1 (bottom). The plot shows up to which order $n_{\max}$ the function $\overline{\Gamma}_\alpha$ needs to be expanded so that the truncation error is less than 10% and 1%, respectively. In principle, it can be seen that for larger positive or negative α gradually more modes are needed. However, for negative values regions occur where the needed mode number drops down to a smaller value. A clear reasoning for this can not be given here. It could be related to the fact that $\overline{\Gamma}_\alpha$ becomes for certain negative surface tensions particularly simple with, potentially, less terms needed. This will be discussed in the following section.

Overall, from the results in Figure C.24 it can be concluded that choosing $n_{\max} = 5$, as used throughout this work, is sufficient for a large range of surface tensions to keep the truncation error below $\epsilon = 10\%$.

Imposing a constant surface area

In this work a constant surface area A of the membrane sheet is assumed. According to the discussion in section 2.1 the related constraint condition for the excess area Ω is given by (2.7) on page 49:

$$\Omega \equiv \frac{1}{2}\int_0^1 d\overline{x}d\overline{y}\,\overline{\nabla}_\parallel\,\overline{h}^2. \tag{C.26}$$

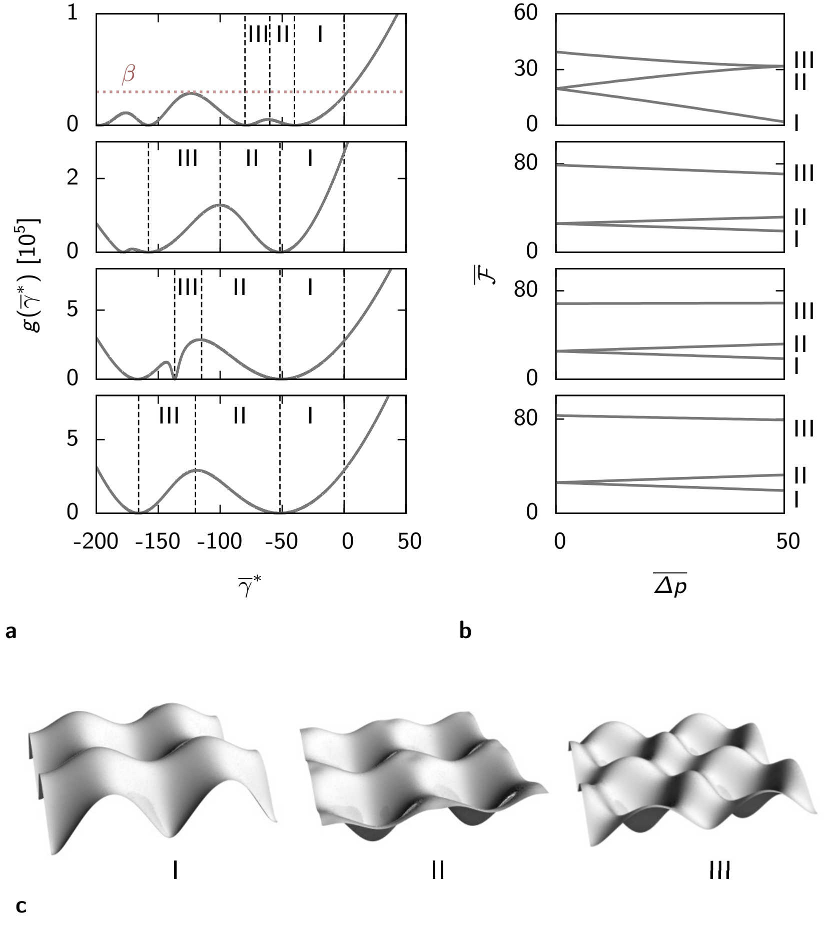

Figure C.2 | Higher order equilibrium solutions of an anchored membrane sheet. a shows the function $g(\overline{\gamma}^*)$ (see (C.28)) as a function of the surface tension for the four different anchoring configurations $q = 0$, $q = 1$, $q = 2$ and $q = 3$. Its intersection points with β (red dashed line) define the surface tension. The numbered intervals correspond to multiple solutions for the same value of β. Their energies $\overline{\mathcal{F}}$ (evaluated for one unit element) are plotted in **b** for fixed excess area $\Omega = 0.5$ and varying pressure difference. The shapes in **c** illustrate different solutions for the same value of β, $q = 0$, $\Omega = 0.5$ and $\overline{\Delta p} = 40$ is used.

Plugging (C.15) into (C.26) gives a defining equation for $\overline{\gamma}^*$. In general this equation can not be solved analytically, even if the series of $\overline{\Gamma}_\alpha$ could be expressed in terms of standard functions. Instead the built-in function `FindRoot` of MATHEMATICA is used to compute $\overline{\gamma}^*$ numerically. In order to do so, (C.26) can be rewritten, for convenience, in such a way that the terms containing the determining physical parameters, Ω and $\overline{\Delta p}$, are separated from those containing $\overline{\gamma}^*$. This can be done by recalling the fact that $\overline{f}_{\mathrm{a}}^{(s)}$ explicitly depends on $\overline{\Delta p}$ only by a linear prefactor and thus also $\overline{h}(\overline{x}, \overline{y})$. Then a height profile $\overline{h}^* := \overline{h}/\overline{\Delta p}$ can be introduced which does not explicitly depend on Δp and (C.26) becomes

$$g(\overline{\gamma}^*) \overset{!}{=} \beta \tag{C.27}$$

with

$$g(\overline{\gamma}^*) := \frac{2}{\int_0^1 d\overline{x} d\overline{y} \, \overline{\nabla}_{\|} \, \overline{h}^{*2}}, \quad \beta := \frac{\overline{\Delta p}^2}{\Omega}. \tag{C.28}$$

The function $g(\overline{\gamma}^*)$ is shown in Figure C.2a for four different anchoring configurations, $q = 0$, $q = 1$, $q = 2$ and $q = 3$. Computing the intersection of $g(\overline{\gamma}^*)$ with the horizontal line β defines the value of $\overline{\gamma}^*$, which is then a function of the physical quantities Ω and $\overline{\Delta p}$ and the anchor configuration, determined by q. On the one hand, this leads above a certain value of β to uniquely defined positive valued surface tensions. On the other hand, for small enough β several solutions for $\overline{\gamma}^*$ become possible since $g(\overline{\gamma}^*)$ exhibits multiple minima and maxima for $\overline{\gamma}^* < 0$. The minima are caused by poles of $\overline{\Gamma}_{\overline{\gamma}^*}$. They occur when the negative surface tension reaches a value where the two terms in at least one of the denominators of $\overline{\Gamma}_{\overline{\gamma}^*}$ cancel each other. As $\overline{\Gamma}_{\overline{\gamma}^*}$ diverges then, also $\overline{h}$ diverges and $g(\overline{\gamma}^*)$ becomes zero. Consequently, the minima are equal to roots of $g(\overline{\gamma}^*)$. The values $\overline{\gamma}_0^*$, where the minima occur, can directly be deduced for $q = 0$ by setting the denominators of $\overline{\Gamma}_{\overline{\gamma}^*}$ equal to zero. Then

$$\overline{\gamma}_0^* = 4\pi^2(n^2 + m^2), \quad n = 0, 1, \ldots \quad m = 1, 2, \ldots . \tag{C.29}$$

For $q > 0$ it seems not to be possible to derive an equivalently simple, analytical expression for the minima of $g(\overline{\gamma}^*)$. This is because in these cases also the force coefficients $\overline{f}_{\mathrm{a}}^{(s)}$ depend on $\overline{\gamma}^*$.

To get a better visual impression of the meaning of the different branches for $\overline{\gamma}^* < 0$, three example shapes at $q = 0$ are shown in Figure C.2c. The shape from branch III exhibits a higher degree of folding than that in I, indicating that higher branches correspond to a higher folding (wave) mode. Branch II is the *inverted* antagonist to branch I. It originates from the position of the minimum at $\overline{\gamma}_0^* = -4\pi^2$ where $\overline{\Delta p}$ is zero (for finite excess area) and, hence, both a folding upwards and downwards (inverted) is, in principle, equally likely. Whether branch II is at all a stable solution is not studied here in more detail[4]. Instead it is assumed from now on that branch I is the primary branch chosen by the membrane sheet. This is not only due to its always lower surface tension (in absolute values) compared to higher branches but also because of its always lower energy per unit element as shown in Figure C.2b[5]. Furthermore, branch I guarantees a continuos transition to the unique branch at positive surface tension. Hence, the final result of $\overline{\gamma}^*(\beta)$ can be computed as shown in Figure C.3.

A closer look at the primary branch of $g(\overline{\gamma}^*)$ allows a more detailed characterization of $\overline{\gamma}^*(\beta)$ in the limits $\beta \to 0$ and $\beta \to \infty$ and, furthermore, of the location of the root $\overline{\gamma}^* = 0$, which shall be denoted by β_0. In both limits of β the function $g(\overline{\gamma}^*)$ can be

---

[4] A further discussion of inverted membrane shapes can be found in section 3.2.3.

[5] The energy $\overline{\mathcal{F}}$ of the membrane, expressed in the Monge parameterization, is taken from appendix B.2, assuming a constant membrane surface area.

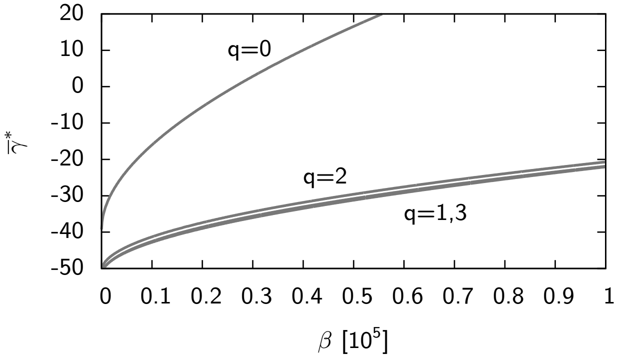

Figure C.3 | Surface tension of an anchored membrane sheet. Plotted as a function of the parameter β. The different values of *q* correspond to different anchor configurations.

approximated by a quadratic ansatz:

$$g(\overline{\gamma}^*) \propto \frac{1}{\overline{r}_0^{*2}} (\overline{\gamma}^* - \overline{\gamma}_0^*)^2 \quad \text{for} \quad \beta = 0, \tag{C.30}$$

$$g(\overline{\gamma}^*) \propto \frac{1}{\overline{r}^{*2}} \overline{\gamma}^{*2} \quad \text{for} \quad \beta \to \infty. \tag{C.31}$$

Based on this, it can be concluded that $\overline{\gamma}^*$ increases as $\sqrt{\beta}$ with different prefactors for small and large values of β. The values of the different constants $\overline{r}_0^*$, $\overline{r}^*$, γ_0 and β_0 are summarized in Table 2.1 on page 54 for the four different anchor configurations, up to the numerical precision provided by the expanded height profile $\overline{h}$.

Interestingly, with the help of the asymptotic behavior of $\overline{\gamma}^*$ near $\beta = 0$, the height profile $\overline{h}$, as defined in (C.15) and (C.23), can be simplified for $\overline{\Delta p} = 0$ and $q = 0$. Namely, it takes the form

$$\overline{h}(\overline{x}, \overline{y}) = \frac{\sqrt{\Omega}}{\pi\sqrt{2}} \left[2 - \cos(2\pi\overline{x}) - \cos(2\pi\overline{y})\right]. \tag{C.32}$$

This can be verified by replacing $\overline{\gamma}^*$ in $\overline{h}$ with the asymptotic approximation $\overline{\gamma}^* \propto -4\pi^2 + \overline{\Delta p}/\sqrt{2\pi^2\Omega}$ for $\overline{\Delta p} \approx 0$ as introduced in (C.30). Then all terms except one are in leading order proportional to $\overline{\Delta p}$. The exception occurs where the denominator satisfies (C.29) and, thus, $\overline{\Delta p}$ cancels. This term is equivalent to (C.32). In principle, also for $q > 0$ such a simple wave solution must exist, since they are solutions of the homogeneous problem of (B.12). This is briefly discussed in section 2.4.1. Their corresponding surface tensions can be estimated from the wave length required to match the linker distances: $\overline{\gamma}_0^* = 16\pi^2$ $(q = 1)$, $\overline{\gamma}_0^* = 36\pi^2$ $(q = 2)$ and $\overline{\gamma}_0^* = 64\pi^2$ $(q = 3)$. As for $q = 0$, these points correspond to minima of $g(\overline{\gamma}^*)$. The first, for $q = 1$, can be identified in Figure C.2a as the second minimum, counted from the right. The related minima for $q = 2$ and $q = 3$ are each located further left, outside the plotted range. Therewith, it becomes clear that the simple wave-like solutions for $q > 0$ are energetically less favorable than those solutions found for smaller negative surface tension.

APPENDIX

NUMERICAL SOLUTION FOR PROTRUSION SHAPES

D

In order to solve the coupled set of shape equations (B.41), (B.46) and (B.47) (or (3.4) – (3.7) on page 64) under the related boundary and constraint conditions for a membrane protrusion a *steepest descent method* is used here [185]. The idea of this method is to compute the equilibrium shape by iteratively evolving an initial guess of ψ and Λ until it reaches the equilibrium. This initial guess must satisfy the constraints but not the shape equations (B.46) and (B.47) itself.

Plugging a non-equilibrium solution into the shape equations leads to a non-vanishing left-hand side, which can formally be written according to the variation in $\overline{\delta\mathcal{F}}^*$ (B.29) as[1]

$$\overline{f}_\psi = \frac{\delta\overline{\mathcal{F}}^*}{\delta\psi} = \overline{f}_\psi^{(1)} + \overline{\gamma}\,\overline{f}_\psi^{(2)} + \overline{\mu}_0\overline{f}_\psi^{(3)}, \tag{D.1}$$

$$\overline{f}_{\overline{\Lambda}} = \frac{\partial\overline{\mathcal{F}}^*}{\partial\overline{\Lambda}} = \overline{f}_\Lambda^{(1)} + \overline{\gamma}\,\overline{f}_\Lambda^{(2)} + \overline{\mu}_0\overline{f}_\Lambda^{(3)}. \tag{D.2}$$

Here $\overline{f}_\psi$ and $\overline{f}_\Lambda$ are those forces exerted on the non-equilibrium initial shape that attempt to restore the equilibrium shape. By introducing the simple linear dynamical ansatz

---

[1] In this section normalized quantities are used as introduced in section 3.1 and mentioned in footnote 1.

$$-\alpha_{\psi}\frac{\partial\psi}{\partial t} = \overline{f}_{\psi}, \quad -\alpha_{\overline{\Lambda}}\frac{\partial\overline{\Lambda}}{\partial t} = \overline{f}_{\overline{\Lambda}} \tag{D.3}$$

with α_{ψ} and $\alpha_{\overline{\Lambda}}$ being arbitrary friction coefficients, these forces can relax as $\psi(t)$ and $\overline{\Lambda}(t)$ are changing. At the same time the overall energy $\overline{\mathcal{F}}^{*}$ decreases monotonously:

$$\begin{aligned}\frac{\partial\overline{\mathcal{F}}^{*}}{\partial t} &= \frac{\partial\overline{\mathcal{F}}^{*}}{\partial\overline{\Lambda}}\frac{\partial\overline{\Lambda}}{\partial t} + \int du\frac{\delta\overline{\mathcal{F}}^{*}}{\delta\psi}\frac{\partial\psi}{\partial t}\\ &= -\left[\alpha_{\overline{\Lambda}}\left(\frac{\partial\overline{\Lambda}}{\partial t}\right)^{2} + \int du\,\alpha_{\psi}\left(\frac{\partial\psi}{\partial t}\right)^{2}\right] < 0 \quad \forall t.\end{aligned} \tag{D.4}$$

In general, the dynamics of $\psi(t)$ and $\Lambda(t)$ do not reflect the real dynamics of the system. However, here only the equilibrium solutions are of interest, which are given by $\psi(t \to \infty)$ and $\Lambda(t \to \infty)$. Therefore, the time t can be rescaled, *e.g.*, by the average friction coefficient $\langle\alpha\rangle = (\alpha_{\psi} + \alpha_{\overline{\Lambda}})/2$. Then $\bar{t} := t/\langle\alpha\rangle$, $\overline{\alpha}_{\psi} := \alpha_{\psi}/\langle\alpha\rangle$ and $\overline{\alpha}_{\overline{\Lambda}} := \alpha_{\overline{\Lambda}}/\langle\alpha\rangle$.

The initial shape $\psi(u = 0)$, $\Lambda(u = 0)$ is chosen such that it satisfies the required constrained conditions. To ensure that the shape at any time point also satisfies these conditions the two parameters γ and μ_0 of the shape equations need to be continuously adjusted accordingly. The exact expressions for this adjustment can be derived by differentiating the constraint conditions (B.45) and (B.49) with respect to t. Obviously, these derivatives have to vanish:

$$0 \equiv \frac{\partial 1}{\partial\bar{t}} = \frac{\partial}{\partial\bar{t}}\left\{\overline{\Lambda}(t)\int_{0}^{1} \mathrm{d}u\cos(\psi(\bar{t}))\right\}, \tag{D.5}$$

$$0 \overset{!}{=} \frac{\partial A}{\partial \bar{t}} = 2\pi \frac{\partial}{\partial \bar{t}} \left\{ \overline{\Lambda}(\bar{t}) \int\limits_0^1 \mathrm{d}u \, \overline{\Lambda}(\bar{t}) \int\limits_0^u \mathrm{d}u \, \cos(\psi(\bar{t})) \right\} . \tag{D.6}$$

Carefully applying the chain rule to the right-hand sides, using (D.3) and sorting terms by $\overline{\gamma}$ and $\overline{\mu}_0$, as done before for the shape equations, leads to

$$0 = \bar{b}_1 + \overline{\gamma}\, \bar{b}_2 + \overline{\mu}_0 \, \bar{b}_3, \tag{D.7}$$

$$0 = \bar{b}_4 + \overline{\gamma}\, \bar{b}_5 + \overline{\mu}_0 \, \bar{b}_6 \tag{D.8}$$

with

$$\bar{b}_j = \frac{1}{2\overline{\alpha}_{\overline{\Lambda}}} \overline{f}^{(j)}_{\Lambda} - \frac{\overline{\Lambda}^2}{4\overline{\alpha}_\psi} \int\limits_0^1 \mathrm{d}u \, \overline{f}^{(j)}_{\psi}(u) \sin(\psi), \tag{D.9}$$

$$\bar{b}_{j+3} = \left(\frac{\Omega - \overline{\Lambda} + 1}{4\overline{\alpha}_{\overline{\Lambda}}} \right) \overline{f}^{(j)}_{\Lambda} \tag{D.10}$$

$$+ \frac{\overline{\Lambda}^3}{16\, \overline{\alpha}_\psi} \int\limits_0^1 \mathrm{d}u \left\{ \int\limits_0^u \mathrm{d}u' \overline{f}^{(j)}_{\psi}(u') \sin(\psi(u')) \right\} , \tag{D.11}$$

where $j = 1, 2, 3$. This gives a system of equations for $\overline{\gamma}$ and $\overline{\mu}_0$, which can be solved immediately:

$$\overline{\gamma} = \frac{\bar{b}_1 \bar{b}_6 - \bar{b}_3 \bar{b}_4}{\bar{b}_3 \bar{b}_5 - \bar{b}_2 \bar{b}_6}, \quad \overline{\mu}_0 = \frac{\bar{b}_2 \bar{b}_4 - \bar{b}_1 \bar{b}_5}{\bar{b}_3 \bar{b}_5 - \bar{b}_2 \bar{b}_6}. \tag{D.12}$$

Hence, $\overline{\gamma}$ and $\overline{\mu}_0$ can be expressed by $\psi(\bar{t})$ and $\overline{\Lambda}(\bar{t})$ and depend thus on $\bar{t}$ as well.

The relations (D.12) can be used to replace $\overline{\gamma}$ and $\overline{\mu}_0$ in (D.2). Then these deduced equations, together with the equation for the radius $\overline{\rho}$ (B.41), define a system of shape equations without the constraints imposed for l and A. Only the boundary conditions $\psi(u=0)=\psi(u=1)=0$ (see (3.2) on page 63) have to be taken into account. They imply:

$$\left.\frac{\partial\psi}{\partial\bar{t}}\right|_{u=0}=\left.\frac{\partial\psi}{\partial\bar{t}}\right|_{u=1}=0,\quad\forall\bar{t}. \tag{D.13}$$

Thus, the method, described here, transfers a time-independent problem with additional constraints into a time-dependent problem without constraints.

Generating the initial shape

The remaining difficulty of the described equilibration method is to find an appropriate initial shape. It needs to satisfy the boundary conditions $\psi(u=0)=\psi(u=1)=0$ as well as the constraints for A and l.

For finding such an initial shape it is useful to rewrite the constraint conditions (B.49) and (B.45) as:

$$\Omega = 2\overline{\Lambda}\left(1-\overline{\Lambda}I_1\right)-1, \tag{D.14}$$

$$1=\overline{\Lambda}I_2 \tag{D.15}$$

with

$$I_1 := \int_0^1 du\int_0^u du'\,\cos\psi,\quad I_2 := \int_0^1 du\,\cos\psi. \tag{D.16}$$

In this form it becomes clear that $\overline{\Lambda}$ can be eliminated in (D.14) by (D.15) so that one condition, which depends on ψ only, remains:

$$0=I_1+\frac{\Omega+1}{2}I_2^2-I_2. \tag{D.17}$$

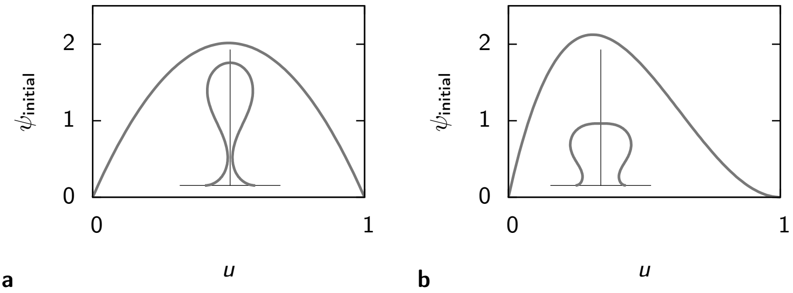

Figure D.1 | Comparison of two different initial profiles ψ_{initial}. **a** shows a profile chosen according to (D.19). **b** shows a profile chosen according to (D.23). The insets show the related profiles as a ρ-z plot.

Hence, it is sufficient to construct ψ_{initial} so that it satisfies (D.17). The value of Λ_{initial} is afterwards automatically determined by (D.15). A very simple ansatz for ψ_{initial} is given by a quadratic function

$$\psi_{\text{initial}} = Au^2 + Bu + C. \tag{D.18}$$

Applying the boundary values the profile simplifies to

$$\psi_{\text{initial}} = Au\,(1-u)\,. \tag{D.19}$$

Plugging this into (D.17) gives a determining equation for the remaining parameter A. In general, this equation needs to be solved numerically.

In practice, the quadratic ansatz for ψ_{initial} is limiting the maximal possible excess area to an approximate value of $\Omega = 6$. That is the case because above this value the neck of the initial protrusion shape is closed. This can be seen in Figure D.1a where the initial shape is plotted for $\Omega = 5$. Then the equilibration procedure fails because the radius reaches a value of zero within the boundaries. To avoid the neck closure, it is necessary to introduce an initial shape that is asymmetric with respect to the boundaries. More precisely, at the lower boundary the angle ψ has to increase faster than it decays at the upper boundary in order to broaden the neck. Furthermore, a convenient choice for the profile would include a parameter which can be tuned according to the imposed excess area. More excess area would then automatically increase the neck width. Therefore, the following two additional boundary conditions for the initial profile can be introduced:

$$\partial_u \psi_{\text{initial}}\big|_{u=0} = \Omega + 1 \qquad \partial_u \psi_{\text{initial}}\big|_{u=1} = 0. \tag{D.20}$$

Note that these conditions are purely artificial. They are not required for the actual solution of the shape equations and this solution may not even follow these conditions. However, they help to construct a profile that satisfies the requirements, discussed above. Using again a quadratic ansatz with one additional $1/u$ term

$$\psi_{\text{initial}} = Au^2 + Bu + C + \frac{D}{u+E}. \tag{D.21}$$

and applaying the four boundary conditions leads to

$$\psi_{\text{initial}} = (\Omega + 1)\,\overline{\Delta p}\,D\frac{u(u-1)^2}{D+u}. \tag{D.22}$$

Plugging this again into the conditions (D.17) shows that no value of D can satisfy this condition. However, modifying (D.22) by squaring D in the numerator

$$\psi_{\text{initial}} = (\Omega + 1)\,\overline{\Delta p}\,D^2\frac{u(u-1)^2}{D+u}. \tag{D.23}$$

rescues the ansatz as now solutions can be found. An example of the resulting initial profile for $\Omega = 5$ is shown in Figure D.1b. It can be clearly seen that, indeed, the neck of the profile is much broader than for the more simple quadratic ansatz.

It is important to emphasize here that the choices made for ψ_{initial} (especially the second) are rather based on explorative testings than on rigorous arguments or even derivations. Any other guess, which satisfies the boundary and constraint condition as explained, would be equally appropriate as those presented here.

Implementation

The numerical procedures to find an appropriate initial shape and equilibrium shape of a membrane protrusion are implemented in MATLAB. The corresponding functions `initialprofile.m` and `protrusion.m` are available upon request.

The function `initialprofile.m` generates an initial shape on a finite, equidistant, spatial grid with grid size Δu[2]. The integrals I_1 and I_2 in (D.16) are solved as well as all other integrals by a *trapezoidal integration* [213]. The initial shape is used by `protrusion.m` to compute the equilibrium shape according to (D.3). The time evolution is discretized by the simple *Euler forward step*[3] [213]:

$$\psi(\bar{t} + \overline{\Delta t}) = \psi(\bar{t}) + \frac{\bar{f}_\psi}{\bar{\alpha}_\psi}\overline{\Delta t} + \mathcal{O}(\overline{\Delta t}^2), \tag{D.24}$$

$$\bar{\Lambda}(\bar{t} + \overline{\Delta t}) = \bar{\Lambda}(\bar{t}) + \frac{\bar{f}_{\bar{\Lambda}}}{\bar{\alpha}_{\bar{\Lambda}}}\overline{\Delta t} + \mathcal{O}(\overline{\Delta t}^2). \tag{D.25}$$

The step size $\overline{\Delta t}$ of the time evolution is changed adaptively [185].

---

[2] For finding a more accurate initial profile, according to the discussion of the previous paragraph, a step size $\Delta u/10$ is used. Only to limit the computational effort the returned initial profile is then computed for a smaller resolution δu.

[3] For comparison also a fourth order Runge-Kutta step was used, which led the same results as for the Euler step.

The spatial derivatives of ψ, needed for the functions $\overline{f}_{\psi}^{(1)}$, $\overline{f}_{\psi}^{(2)}$ and $\overline{f}_{\psi}^{(3)}$ in the shape equations (B.46) and (B.47), are approximated by [185]

$$\frac{\partial\psi}{\partial u} = \frac{\psi(u+\Delta u) - \psi(u-\Delta u)}{2\Delta u} + \mathcal{O}(\Delta u^2), \tag{D.26}$$

$$\frac{\partial^2\psi}{\partial u^2} = \frac{\psi(u+\Delta u) - 2\psi(u) + \psi(u-\Delta u)}{\Delta u^2} + \mathcal{O}(\Delta u^3). \tag{D.27}$$

At the boundaries these derivates are not required for the time evolution as the time derivative vanishes there (see (D.13)).

Stability of the equilibrium solution

The equilibration of the initial guess, ψ_{initial} and $\overline{\Lambda}_{\text{initial}}$, is executed numerically as long as at least one of the conditions[4]

$$\epsilon_{\psi} := \frac{\overline{\Delta t}}{\overline{\alpha}_{\psi}} \frac{\langle \overline{f}_{\psi} \rangle}{\langle \psi(\overline{t}) \rangle} > 10^{-8}, \qquad \epsilon_{\overline{\Lambda}} := \frac{\overline{\Delta t}}{\overline{\alpha}_{\overline{\Lambda}}} \frac{\langle \overline{f}_{\overline{\Lambda}} \rangle}{\langle \overline{\Lambda}(\overline{t}) \rangle} > 10^{-8} \tag{D.28}$$

with the discrete spatial average along the shape profile

$$\langle \psi(u) \rangle = \Delta u \sum_{m=0}^{1/\Delta u} \psi(m\,\Delta u) \tag{D.29}$$

holds. If, eventually, both are undercut the obtained solution satisfies the equilibrium shape equations up to the chosen accuracy of 10^{-8}. However, only those solutions are considered that also converge to a steady state, *i.e.*, ϵ_{ψ}, $\epsilon_{\overline{\Lambda}}$ and the energy $\overline{\mathcal{F}}^{*}$ reach asymptotically a constant value as shown in Figure D.2 for an example calculation.

---

[4] Another measure would be given by computing the average of the ratios $\overline{f}_{\psi}/\psi$ and $\overline{f}_{\Lambda}/\Lambda$ instead, where the boundaries at $u = 0$ and $u = 1$ must be excluded.

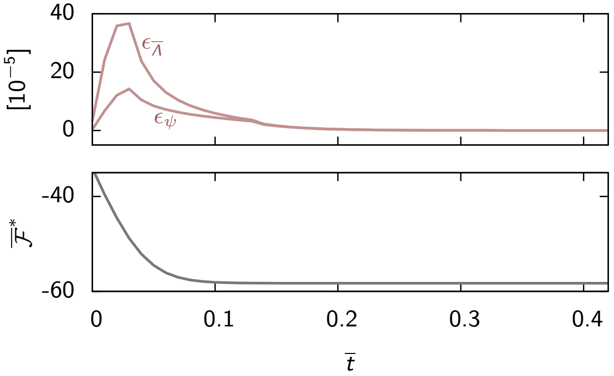

Figure D.2 | Steady state convergence of the numerical evaluation of (D.3)**.** The top figure shows the quantities introduced in (D.28) as a function of the simulation time, the lower the protrusion energy. For this example simulation the parameters are chosen as $\Omega = 2$, $\overline{\Delta p} = 200$, $\overline{f} = 0$, $\overline{C}_0 = 0$ and $\Delta u = 0.01$.

The steady-state convergence guarantees that the computed solution automatically corresponds to a (locally) *stable* equilibrium. This is because then, as derived in (D.4) and shown in Figure D.2, the energy monotonously decays to a minimal value. As a second verification of the stability, to cross-check the method, a *linear stability analysis* is applied in addition [193]. For this purpose it is convenient to rewrite the dynamic equations (D.3) in its discretized version as

$$\frac{d\mathbf{S}}{d\overline{t}} = \mathbf{G}(\mathbf{S}) \tag{D.30}$$

with

$$\mathbf{S} = \begin{pmatrix} \psi(0) \\ \psi(\Delta u) \\ \vdots \\ \psi(1) \\ \overline{\Lambda} \end{pmatrix}, \quad \mathbf{G}(\mathbf{S}) = -\begin{pmatrix} \overline{f}_{\psi}(0)/\overline{\alpha}_{\psi} \\ \overline{f}_{\psi}(\Delta u)/\overline{\alpha}_{\psi} \\ \vdots \\ \overline{f}_{\psi}(1)/\overline{\alpha}_{\psi} \\ \overline{f}_{\overline{\Lambda}}/\overline{\alpha}_{\overline{\Lambda}} \end{pmatrix}. \tag{D.31}$$

If $\mathbf{S}_0$ is a solution which satisfies the equilibrium shape equations, then $\mathbf{S}_0$ is a *fixed point*. The stability of this fixed point is determined, according to the linear stability analysis, by the *Jacobian matrix*

$$J_{ij} := \left.\frac{\partial G_i}{\partial S_j}\right|_{\mathbf{S}_0} . \tag{D.32}$$

If the eigenvalues of $\mathbf{J}$ are all smaller than zero, then the system is stable at $\mathbf{S}_0$.

The evaluation of (D.32), performed here by an implementation in `jacobiM.m`, reveals that for the equilibrium solutions found in this work all but two eigenvalues are negative. The two exceptions have zero value, indicating that their corresponding eigenvectors give rise to equally favorable solutions. However, this can be understood by the fact that the linear perturbation of the stability analysis violates the two constraint conditions, (B.45) and (B.49), and hence these new solutions belong to different constraint values, one has an increased protrusion surface area and a decreased protrusion diameter the other a decreased area and an increased diameter.

Reliability of the numerical solution

In order to ensure the reliability of the numerical results, obtained with the presented method and discussed in this work, several tests are utilized. First, it can be confirmed for every simulation that the constraint conditions (B.45) on page 148 and (B.49) on page 149, which lead to the conditions in (D.12) for $\overline{\gamma}$ and $\overline{\mu}_0$, are conserved throughout the iterative equilibration. Second, as shown in Figure D.2 for one example, also the energy is found to always decay monotonously, which is in agreement with (D.4).

Two further tests have been performed for some example simulations. One is the decrease of the spatial discretization size $\overline{\Delta u}$.

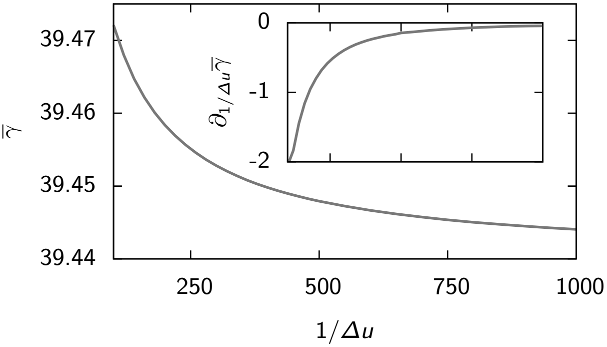

Figure D.3 | Convergence of the numerical solution for a decreasing discretization step. Plotted is an example result of the simulation for the surface tension over the inverse spatial grid size. The used simulation parameters are $\Omega = 2$, $\overline{\Delta p} = 200$, $\overline{f} = 0$ and $\overline{C}_0 = 0$. The inset shows the derivative of the main curve.

As expected, for a sufficiently small grid size the simulation results converge to a constant value (see Figure D.2). For the other test the equilibrium shape of the protrusion is separately calculated via the Monge parameterization (see appendix B.2), using the same numerical procedure. From this it can be concluded that, as required, the simulation results are, indeed, invariant under parameterization changes. One example is shown in Figure D.4 where the results for elongation and surface tension of a protrusion calculated in both the arc length and the Monge parameterization are compared (gray solid line vs. dark gray crosses).

Besides the numerical testings, analytical approximations are provided in this work to give an orientation of the trustworthiness of the numerical results (see, *e.g.*, appendix E). In particular the weak-bending approximation of the Monge parameterization is of interest. It is introduced for protrusions with axial symmetry in appendix E.1 and is plotted in addition to the full Monge parameterization and the arc length parameterization in Figure D.4 (red dashed line). The

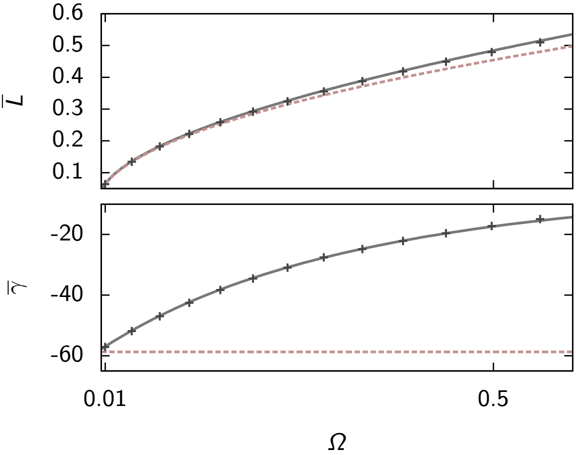

Figure D.4 | Divergence of the analytical solution from the full numerical solution for increasing excess area. The solid gray line shows the elongation (top) and the surface tension (bottom) as a function of the normalized protrusion area, obtained with the arc length parameterization. The dark gray crosses indicate the solutions for the Monge parameterization, the red dashed line these for the analytical weak-bending approximation (see appendix E.1 and Figure E.1). The used parameters are $\overline{\Delta p} = 0$, $\overline{f} = 0$, $\overline{C}_0 = 0$ and $\Delta u = 100$ (arc length) and $\overline{\Delta \rho} = 200$ (Monge), respectively.

elongation of the analytical weak-bending result approaches the full solution asymptotically as $\Omega \to 0$. This is in agreement with the definition of the weak-bending approximation, which only takes into account weak variations of the height profile, as occurring for $\Omega \approx 0$. On the other hand, the surface tension diverges immediately, not asymptotically. It only agrees with the numerical result at $\Omega = 0$ where $\overline{\gamma}$ is given by (E.19) on page 186. This can be clarified by using the shape equation (B.17) on page 142 and solve it for $\overline{\gamma}$:

$$\gamma = -\frac{f_h^{(1)}}{f_h^{(2)}}. \tag{D.33}$$

Now, either $f_h^{(1)}$ and $f_h^{(2)}$ can be expanded for weak height variations first, as done in the weak-bending approximation, or its ratio can be expanded directly. By doing so, the latter gives additional linear terms which do not appear in the first case. As, in turn, the latter case reflects the behavior of the full Monge parameterization at $\Omega \approx 0$ this indicates that the weak-bending approximation seems to miss relevant information for the description of the surface tension, even in the limit of weak bending.

APPENDIX

MEMBRANE PROTRUSIONS IN ANALYTICAL LIMITS E

In general, the equilibrium shapes of membrane protrusions as introduced and discussed in chapter 3 cannot be computed analytically. This is because in both the Monge parameterization and the arc length parameterization the obtained shape equations are strongly nonlinear. Whereas the numerical solution is discussed in appendix D, here three limits are discussed for which analytical results can be found. The first is the *weak-bending approximation*, which has been introduced in section 1.3.3. The second limit can be found for vanishing bending rigidity, $\kappa \to 0$. The third analytical limit can be discussed for a non-vanishing point force f, applied to the tip of a protrusion, which then adopts approximately the shape of cylindrical *membrane tubes*.

E.1 | Weak-bending approximation

The shape equation (B.20) for $h(\rho)$ in the weak-bending approximation is linear with non-constant coefficients. It can firstly be rewritten in dimensionless form with the help of the normalizations, introduced in section 3.1[1]. Secondly, (B.20) can immediately be integrated once to

$$\overline{\rho}^2\overline{h}_{|\overline{\rho}\overline{\rho}\overline{\rho}} + \overline{\rho}\overline{h}_{|\overline{\rho}\overline{\rho}} - (1+\overline{\gamma}^*\,\overline{\rho}^2)\overline{h}_{|\overline{\rho}} = \frac{\overline{\Delta p}}{2}\overline{\rho}^3 - D_1\overline{\rho}, \tag{E.1}$$

where the whole equation has been multiplied with $\overline{\rho}$ and D_1 is the first integration constant. By introducing a new function $\tilde{\overline{h}}(\overline{\rho})$ such that $\overline{h}_{|\overline{\rho}} \equiv \tilde{\overline{h}} + \frac{D_1}{\overline{\gamma}^*}\frac{1}{\overline{\rho}}$, (E.1) takes the following form:

$$\overline{\rho}^2\tilde{\overline{h}}_{|\overline{\rho}\overline{\rho}} + \overline{\rho}\,\tilde{\overline{h}}_{|\overline{\rho}} - (1+\overline{\gamma}^*\,\overline{\rho}^2)\tilde{\overline{h}} = \frac{\overline{\Delta p}}{2}\overline{\rho}^3. \tag{E.2}$$

A special solution for the inhomogeneous problem can be guessed as

$$\tilde{\overline{h}}_{\mathrm{s}} = -\frac{1}{\overline{\gamma}^*}\frac{\overline{\Delta p}}{2}\overline{\rho}. \tag{E.3}$$

The general solution of the remaining homogeneous problem can be obtained by performing the coordinate transformation $\overline{\rho} = \mathrm{i}\overline{\rho}^*/\sqrt{\overline{\gamma}^*}$. The resulting equation

$$\overline{\rho}^{*2}\tilde{\overline{h}}_{\mathrm{h}|\overline{\rho}^*\overline{\rho}^*} + \overline{\rho}^*\,\tilde{\overline{h}}_{\mathrm{h}|\overline{\rho}^*} + (\,\overline{\rho}^{*2} - 1)\tilde{\overline{h}}_{\mathrm{h}} = 0 \tag{E.4}$$

is, however, equivalent to the standard form of the first order *Bessel equation* whose solutions are the *Bessel function* of first kind $J_1(\overline{\gamma}^*)$ and second kind $Y_1(\overline{\gamma}^*)$ (also of first order) and their superposition for the general solution [214]

$$\tilde{\overline{h}}_{\mathrm{h}} = D_2 J_1 + D_3 Y_1. \tag{E.5}$$

---

[1] The used normalizations are: $\overline{\Delta p} := \frac{l^3}{\kappa}\Delta p$, $\overline{f} := \frac{l}{\kappa} f$ $\overline{C}_0 := l\,C_0$, $\overline{\gamma} := \frac{l^2}{\kappa}\gamma$, $\Omega := \frac{4}{\pi l^2}A - 1$, $\overline{\mathcal{F}} := 4\mathcal{F}/\pi\kappa$, $\overline{V} := 4V/\pi l^3$ and correspondingly $\overline{h} := \frac{h}{l}$ and $\overline{\rho} := \frac{\rho}{l}$.

Reverting the coordinate transformation and returning to the function $\overline{h}$ by integrating once, the final solution of the initial shape equation (B.20) becomes

$$\begin{aligned}\overline{h} =& D_1 \log \overline{\rho} + D_2 J_0(\mathrm{i}\sqrt{\overline{\gamma}^*}\overline{\rho}) \\ &+ D_3 Y_0(\mathrm{i}\sqrt{\overline{\gamma}^*}\overline{\rho}) + D_4 - \frac{\overline{\Delta p}}{4\overline{\gamma}^*}\overline{\rho}^2,\end{aligned} \tag{E.6}$$

where D_1, D_2 and D_3 have been redefined for convenience to absorb occurring constant prefactors.

In order to specify the solution (E.6) for a membrane protrusion four boundary conditions are required. Those imposed in (3.2) on page 63 for the arc length parameterization give rise to three conditions for the Monge parameterization, namely:

$$u = 0: \qquad \overline{\rho} = \frac{1}{2} \quad \& \quad \overline{h} = 0 \quad \Rightarrow \quad \overline{h}(\overline{\rho} = \frac{1}{2}) = 0 \tag{E.7}$$

$$\& \quad \psi = 0 \quad \Rightarrow \quad \overline{h}_{|\overline{\rho}}(\overline{\rho} = \frac{1}{2}) = 0, \tag{E.8}$$

$$u = 1: \qquad \overline{\rho} = 0 \quad \& \quad \psi = 0 \quad \Rightarrow \quad \overline{h}_{|\overline{\rho}}(\overline{\rho} = 0) = 0. \tag{E.9}$$

The last two relations are due to

$$\frac{\partial \overline{h}}{\partial \overline{\rho}} = \frac{\partial \overline{h}}{\partial s}\left(\frac{\partial \overline{\rho}}{\partial s}\right)^{-1} = \tan\psi \overset{\psi \ll 1}{\approx} \psi. \tag{E.10}$$

A fourth relation can be deduced from the fact that at $\overline{\rho} = 0$ the principal curvatures C_1 and C_2 have to be equal because of the axial symmetry in this point. This leads to a differential equation for $\overline{h}$:

$$\overline{\rho}\,\overline{h}_{|\overline{\rho}\overline{\rho}} - \left(\overline{h}_{|\overline{\rho}} - \overline{h}^3_{|\overline{\rho}}\right) = 0, \tag{E.11}$$

where C_1 and C_2 were taken from the curvature tensor in Table B.1. The general solution of (E.11) describes the functional dependency of $\overline{h}(\overline{\rho})$ close to $\overline{\rho} = 0^2$:

$$\overline{h} \propto \sqrt{\text{const.}_1 - \overline{\rho}^2} + \text{const.}_2 \,. \tag{E.12}$$

It implies for instance that besides the first derivative also the third derivative

$$\overline{h}_{|\overline{\rho}\,\overline{\rho}\,\overline{\rho}}(\overline{\rho} = 0) = 0. \tag{E.13}$$

This means that the curvature along the contour line has to remain continuos at $\overline{\rho} = 0$. Together with (E.9) this is only affordable for $D_1 = D_3 = 0$ of (E.6) as both related functions, the logarithm and the Bessel function of second kind, diverge at $\overline{\rho} = 0$ and any nontrivial linear combination of these functions could not balance this for both the first and third derivative. On the other hand, the remaining parts in (E.6) satisfy the two boundary conditions at $\overline{\rho} = 0$ automatically as $J_0 \propto 1 - \frac{\overline{\rho}^2}{4} + \frac{\overline{\rho}^4}{64}$. The remaining two boundary conditions specify D_2 and D_4 of (E.6) so that the final equilibrium shape of the membrane protrusion takes the form

$$\begin{aligned} \overline{h} = \frac{\overline{\Delta p}\,\overline{\gamma}^{*\,-3/2}}{4 I_1(\sqrt{\overline{\gamma}^*}/2)} \Big[& I_0(\sqrt{\overline{\gamma}^*}\overline{\rho}) - I_0(\sqrt{\overline{\gamma}^*}/2) \\ & + \sqrt{\overline{\gamma}^*}\left(1/4 - \overline{\rho}^2\right) I_1(\sqrt{\overline{\gamma}^*}/2) \Big] \,, \end{aligned} \tag{E.14}$$

where I_0 and I_1 are the zeroth and first order modified Bessel functions of first kind, respectively[3].

To determine the surface tension $\overline{\gamma}^*$ by the imposed excess area Ω of the protrusion the same strategy as presented at the end of appendix C can be applied. The excess area in the weak-bending approximation is given, according to the area element in Table B.1,

---

[2] Replacing $\overline{h}_{|\overline{\rho}} = \overline{g}$ in (E.11) leads to a separable equation, which can be integrated immediately.

[3] They are related to the Bessel functions of first kind in the following way: $I_\alpha(x) = \mathrm{i}^{-\alpha} J_\alpha(\mathrm{i}x)$.

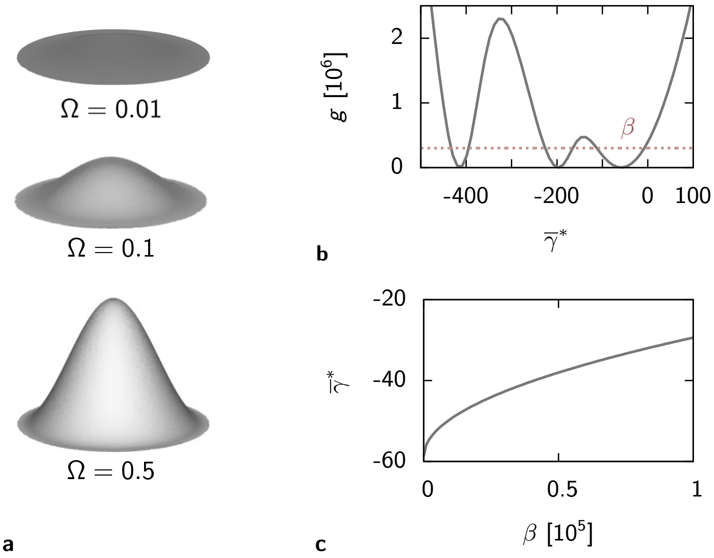

Figure E.1 | Equilibrium properties of a membrane protrusion in weak-bending approximation. a shows the protrusion shape for three different excess areas Ω as indicated, the chosen pressure difference is $\overline{\Delta p} = 100$. In **b** the function g and β, which define the surface tension via (E.16) are shown and in **c** the resulting surface tension as a function of the parameter β as defined in (E.18).

by

$$\Omega = 4 \int_0^{1/2} d\overline{\rho}\, \overline{\rho} \overline{h}^2_{|\overline{\rho}}. \tag{E.15}$$

By separating the given parameters Ω and $\overline{\Delta p}$ on one side of the equation and performing the integration the defining relation for $\overline{\gamma}^*$ reads again as

$$g(\overline{\gamma}^*) \overset{!}{=} \beta, \tag{E.16}$$

now with

$$g(\overline{\gamma}^*) := 64\, \overline{\gamma}^{*3} I_1(\sqrt{\overline{\gamma}^*}/2)^2 \Big[(3\overline{\gamma}^* + 64)\, I_1(\sqrt{\overline{\gamma}^*}/2)$$

$$-8\overline{\gamma}^* I_1(\sqrt{\overline{\gamma}^*}/2) I_0(\sqrt{\overline{\gamma}^*}/2) - 2\overline{\gamma}^* I_0(\sqrt{\overline{\gamma}^*}/2)^2\Big]^{-1} \quad \text{(E.17)}$$

and β as defined previously

$$\beta := \frac{\overline{\Delta p}^2}{\Omega}. \quad \text{(E.18)}$$

The function $g(\overline{\gamma}^*)$ is plotted together with the intersecting line β in Figure E.1b. It exhibits very similar features as those found for a membrane sheet at the end of appendix C. Likewise, (E.16) can only be solved numerically and the resulting surface tension $\overline{\gamma}^*(\beta)$ is shown in Figure E.1c, as well as three example equilibrium shapes (Figure E.1a). Here the same assumptions regarding the choice of the branch at $\overline{\gamma}^* < 0$ as for a membrane sheet are made. The minimal surface tension at $\beta = 0$ is defined by the first root of the Bessel function of first kind:

$$\overline{\gamma}_0^* = 4\left(\min J_1^{-1}(0)\right)^2, \quad \text{(E.19)}$$

where $J_\alpha^{-1}(0)$ are the roots of the respective Bessel function. For large values of β, (E.17) goes asymptotically as the quadrat of the surface tension, $g \propto 64\,\overline{\gamma}^{*2}$, as also found before in appendix C. One additional analytical result can be computed here for the special point $\overline{\gamma}^* = 0$. There $g(0) = 393216$ what specifies the ratio of $\overline{\Delta p}$ to Ω at which the surface tension vanishes.

E.2 | Zero-rigidity approximation

Setting $\kappa = 0$ the energy (B.5) reduces to a sum of the area term and volume term. In this form the energy gives rise to *Laplace's law*, which connects the (constant) curvature radius r of a membrane with the pressure difference Δp and the surface tension γ of the

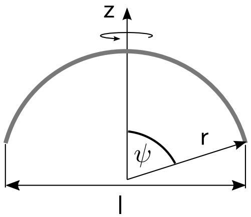

Figure E.2 | Schematic of a membrane protrusion approximated by a spherical cap.

membrane in the following way [103, 104]:

$$r = 2\frac{\gamma}{\Delta p}. \tag{E.20}$$

For a membrane protrusion with axial symmetry this means that it can be described for $\kappa \to 0$ by a spherical cap [170]. Such a cap is sketched in Figure E.2. The surface tension in (E.20) is set by the imposed surface area A of the cap, which can be computed here, *e.g.*, in spherical coordinates:

$$A = r^2 \int_0^{2\pi} d\varphi \int_0^{\psi_{\max}} d\psi \sin\psi = 2\pi r^2 \left(1 - \cos\psi_{\max}\right), \tag{E.21}$$

where the used maximal polar angle $\psi_{\max}$ is defined by the protrusion diameter l:

$$\psi_{\max} := \arcsin\left(l/2r\right). \tag{E.22}$$

Plugging (E.22) and (E.21) into (E.20) and solve this for γ gives

$$\gamma = \frac{\Delta p}{2\pi l} \frac{A}{\sqrt{\frac{4A}{\pi l^2} - 1}}. \tag{E.23}$$

In dimensionless form and using the excess area $\Omega = 4A/\pi l^2 - 1$ the radius $\overline{r}$, the surface tension $\overline{\gamma}$ and the encapsulated volume $\overline{V}$ read

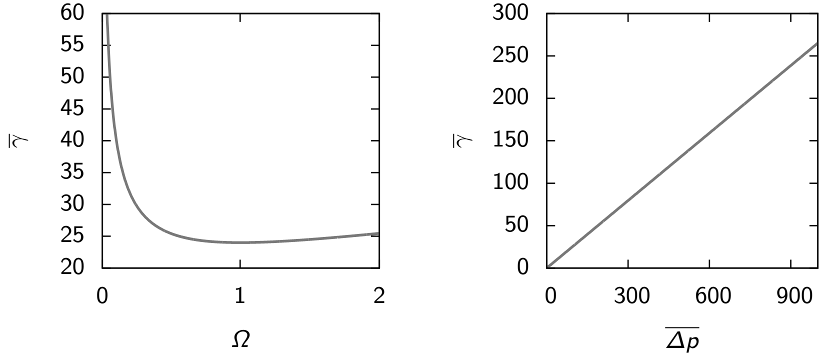

Figure E.3 | Surface tension of a membrane protrusion shaped as spherical cap. The surface tension $\overline{\gamma}$ is plotted, according to (E.24), as a function of the excess area Ω with a constant pressure difference $\overline{\Delta p} = 100$ (left) and as a function of the pressure difference $\overline{\Delta p}$ with a constant excess area $\Omega = 0.5$.

as[4]

$$\overline{r} = \frac{\Omega + 1}{4\sqrt{\Omega}}, \quad \overline{\gamma} = \frac{\overline{\Delta p}}{8} \frac{\Omega + 1}{\sqrt{\Omega}}, \\ \overline{V} = \frac{\Omega + 3}{12}\sqrt{\Omega}. \tag{E.24}$$

Whereas radius and volume do not depend on the pressure difference the surface tension depends on both. It is proportional to $\overline{\Delta p}$ and for $\Omega \to 0$ (flat protrusion) and $\Omega \to \infty$ it diverges, as well as the radius of the protrusion. The volume diverges only in the upper limit, for the lower it vanishes. Radius and surface tension become minimal for $\Omega = 1$ where the spherical cap is a hemisphere. The radius is then $\overline{r} = 1$. The detailed course of $\overline{\gamma}(\Omega, \overline{\Delta p})$ is shown in Figure E.3.

---

[4] Here the same normalization as in footnote 1 is used although it contains $\kappa \neq 0$. κ can be seen here as a simple scaling factor.

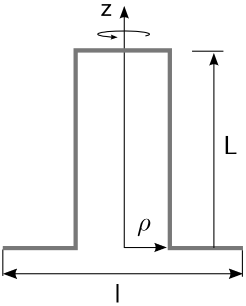

Figure E.4 | Schematic of a cylindrical membrane tube.

E.3 | Tube approximation

When membrane is pulled into a tube it can be modeled, in a good approximation, as a cylinder [116, 191]. This approximation is, compared to the two previous approximations, strictly speaking not rigorous in the mathematical sense because it neglects the bottom part of the protrusion where it is attached to the base. Here this region is instead treated as a flat disc. Then the simplified cross section of the membrane tube takes a form as shown in Figure E.4. The bottom disc as well as the disc at the top of the cylinder do not contribute to the energy of the tube since their curvature is zero. Therefore, recalling volume and side area of a cylinder, the energy (B.5) can be written as[5]

$$\mathcal{F} = \left[\frac{\kappa}{2}\frac{1}{\rho^2} + \gamma\right] 2\pi\rho L - \Delta p \pi \rho^2 L - fL. \tag{E.25}$$

In order to find the equilibrium cylinder shape (E.25) needs to be minimized with respect to both ρ and L. This gives rise to the two equations

$$0 = \overline{\Delta p}\bar{\rho}^3 - \bar{\gamma}\bar{\rho}^2 + \frac{1}{2}, \tag{E.26}$$

---

[5] Area and volume of a cylinder can also be calculated with the help of the expressions in Table B.1 taking into account that ρ is constant.

$$0 = \overline{\Delta p}\overline{\rho}^3 - 2\overline{\gamma}\,\overline{\rho}^2 + \frac{\overline{f}}{\pi}\overline{\rho} - 1, \tag{E.27}$$

where now the same normalized quantities are used as previously for axisymmetric protrusions. A third equation is given by the area conservation, which is considered for the excess area as before:

$$\Omega = 8\overline{\rho}\overline{L}. \tag{E.28}$$

The three equations match the three quantities $\overline{\rho}$, $\overline{L}$ and $\overline{\gamma}$ and can, thus, be solved to express the unknowns by the given parameters $\overline{\Delta p}$ and $\overline{f}$.

To solve (E.26), (E.27) and (E.28) for radius, elongation and surface tension, first, (E.26) and (E.28) can be solved for $\overline{\gamma}$ and $\overline{L}$, respectively:

$$\overline{\gamma} = \frac{2\overline{\Delta p}\,\overline{\rho}^3 + 1}{2\overline{\rho}^2}, \tag{E.29}$$

$$\overline{L} = \frac{\Omega}{8\overline{\rho}}. \tag{E.30}$$

Both still depend on $\overline{\rho}$. However, $\overline{\rho}$ can be determined independently by using (E.29) to eliminate $\overline{\gamma}$ in (E.27). This gives an equation that only depends on the radius:

$$0 = \overline{\Delta p}\,\overline{\rho}^3 - \frac{\overline{f}}{\pi}\overline{\rho} + 2. \tag{E.31}$$

The solution can be derived by standard techniques for cubic equations [215]. From the three occurring solutions only one is of physical relevance, namely

$$\overline{\rho} = 6\pi\frac{\zeta_{\text{tube}}^{-1}}{\overline{f}} \sin\left[\frac{\arcsin\zeta_{\text{tube}}}{3}\right] \tag{E.32}$$

with

$$\zeta_{\text{tube}} := \sqrt{\frac{27\pi^3\overline{\Delta p}}{\overline{f}^3}} \tag{E.33}$$

being a dimensionless parameter, which has to lie in the range

$$0 \leq \zeta_{\text{tube}} \leq 1. \tag{E.34}$$

The upper boundary is required to ensure that $\overline{\rho}$ is real valued, the lower boundary is due to the fact that both the pressure difference and the point force shall be equal or larger than zero here. The radius multiplied with the point force is plotted as a function of ζ_{tube} in Figure E.5a. It is monotonously increasing between 2π at $\zeta_{\text{tube}} = 0$ and 3π at $\zeta_{\text{tube}} = 1$.

The result (E.32) together with (E.29) and (E.30) fully characterizes the equilibrium shape of a membrane tube, simplified by a cylinder. It is interesting to emphasize that neither the radius of the cylindrical tube nor the surface tension depends on the imposed area. The elongation, on the other hand, is directly proportional to the excess area. The pressure difference acts in all cases as a rescaling parameter for the point force. This becomes more obvious by rewriting ζ_{tube} as

$$\frac{\overline{f}}{\overline{f}_{\text{tube}}} = \zeta_{\text{tube}}^{-2/3} \tag{E.35}$$

with

$$\overline{f}_{\text{tube}} := 3\pi\sqrt[3]{\overline{\Delta p}}\,. \tag{E.36}$$

Nevertheless, $\overline{f}_{\text{tube}}$, and therewith $\overline{\Delta p}$, is not only a scaling parameter but, according to the upper limit of ζ_{tube} in (E.34), also the minimal point force needed to induce tubes. The quantities $\overline{\rho}$, $\overline{L}$ and $\overline{\gamma}$ cannot be expressed only in terms of the rescaled point force in (E.35) but the expressions $\overline{\rho}\overline{f}$, $\overline{L}/\Omega\overline{f}$ and $\overline{\gamma}/\overline{f}^2$. The latter two are

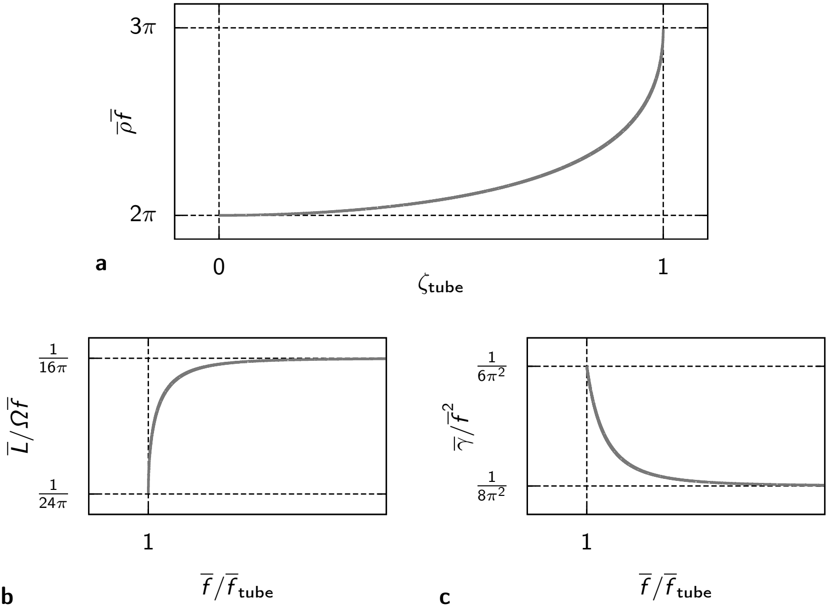

Figure E.5 | Equilibrium properties of a cylindrical membrane tube. **a** shows the tube radius as in (E.32), multiplied with the point force. In **b** the elongation, divided by the imposed excess area and point force, is shown and in **c** the surface tension, divided by the squared point force, both plotted as a function of the rescaled point force (see text). The dashed lines indicate the ranges, according to (E.34), within which the three quantities are defined.

shown in Figure E.5b and Figure E.5c, respectively. Whereas $\overline{L}/\Omega\overline{f}$ increases monotonously, starting from a minimal value at $\overline{f} = \overline{f}_{\mathrm{tube}}$, indicated in the plot, $\overline{\gamma}/\overline{f}^2$ decays monotonously, also starting from $\overline{f} = \overline{f}_{\mathrm{tube}}$. Especially interesting is the asymptotic behavior of both for $\overline{f}/\overline{f}_{\mathrm{tube}} \gg 1$. Both expressions then approach a constant value, from which can be concluded that

$$\overline{L} \propto \frac{\Omega\overline{f}}{16\pi}, \quad \overline{\gamma} \propto \frac{1}{2}\left(\frac{\overline{f}}{2\pi}\right)^2 \quad \text{for} \quad \overline{f} \gg \sqrt[3]{\Delta p}\,. \tag{E.37}$$

APPENDIX

ALTERNATIVE LATERAL TENSION EXPRESSION

F

In this work the *lateral tension* is defined as

$$\gamma_{\|} := \frac{d\mathcal{F}}{dA_{\|}}, \tag{F.1}$$

where $\mathcal{F}$ is the energy (B.5) on page 138 of the membrane and $A_{\|}$ its basal area[1]. Calculating $\gamma_{\|}$ according to (F.1) is inconvenient as it requires first the integration of the equilibrium membrane shape to compute $\mathcal{F}$ and then the differentiation. This procedure can become computationally relatively costly and also inaccurate if a numerical calculation is involved.

An alternative approach to obtain the lateral tension $\gamma_{\|}$ is to study the work dW needed to deform the membrane such that the basal area changes by $dA_{\|}$. This can be done because here the infinitesimal work performed is equal to the negative infinitesimal change of the energy:

$$dW = -d\mathcal{F} = -\gamma_{\|} dA_{\|}. \tag{F.2}$$

---

[1] The basal area $A_{\|}$ is the projection of the membrane area into the x-y-plane.

On the other hand dW can be written as the surface integral[2]

$$dW = \int dA \gamma^{ij} d\epsilon_{i|j} \tag{F.3}$$

over the scalar product of the gradient of local displacements $d\epsilon_i$ and the local, tangential tension tensor [216][3]

$$\gamma_{ij} = \frac{\kappa}{2}(C^{k}_{\ k} - C_0)\left(2C^{k}_{\ i}\, g_{jk} - (C^{k}_{\ k} - C_0)\, g_{ij}\right) - \gamma\, g_{ij}. \tag{F.4}$$

Equation (F.3) can be rewritten by using the chain rule and *force balance* $\gamma^{ij}_{\ \ |j} = 0$ so that the *divergence theorem* [214] can be applied:

$$dW = \int dA \left(\gamma^{ij} d\epsilon_i\right)_{|j} = \oint d\Gamma\, \nu_j \gamma^{ij} d\epsilon_i. \tag{F.5}$$

The second integration is performed along the closed boundary line Γ of the membrane where ν_j is the unit normal vector of the boundary line. If the local displacement $d\epsilon_i$ acts isotropically in perpendicular to the boundary line, then it is, on the one hand, independent of the path integration in (F.5) and, on the other hand, can be written as $d\epsilon_i = d\epsilon\, \nu_i$. Taking this into account in (F.5) together with (F.2) the following relation for the lateral tension can be found[4]:

$$\gamma_{||} = -\left(\frac{dA_{||}}{d\epsilon}\right)^{-1} \oint d\Gamma \nu^i \nu^j \gamma_{ij}. \tag{F.6}$$

Relation (F.6) can further be simplified for specific membrane geometries. Here it is used for membrane protrusions, as discussed in this work. Their axial symmetry is resulting from the full and smooth attachment along the circular boundary line at constant radius $\rho = l/2$. The basal area is, hence, $A_{||} = \frac{\pi}{4} l^2$ and the deformation $d\epsilon =$

---

[2] Again the simplification $_{|i} := \partial/\partial x^i$ is used here.

[3] γ_{ij} is *tangential* to the surface.

[4] Here the indices of $\nu_i \nu_j$ and γ^{ij} were flipped for convenience.

$dl/2$ acts in radial direction (due to the smooth boundary). The boundary path Γ can be parameterized by the polar angle as $d\Gamma = \frac{l}{2} d\varphi$. Equation (F.6) then simplifies to

$$\gamma_{\|} = -\frac{1}{2\pi} \int d\varphi \, \gamma_{\rho\rho} \bigg|_{\rho=\frac{l}{2}} . \tag{F.7}$$

As the membrane protrusion is axisymmetric $\gamma_{\rho\rho}$ does not depend on the integration with respect to φ. That simplifies the lateral tension to $\gamma_{\|} = -\gamma_{\rho\rho}$. Furthermore, taking into account that at the boundary line $g_{\rho\rho} = g_{ss} = \mathbf{b}_s \cdot \mathbf{b}_s = 1$, $g_{\varphi s} = g_{\varphi\rho} = \mathbf{b}_\varphi \cdot \mathbf{b}_s = 0$ and $C^\varphi_{\ \varphi} = 0$, the required tensor component $\gamma_{\rho\rho}$ can be calculated so that the lateral tension for a membrane protrusion becomes

$$\gamma_{\|} = \left[\gamma^* - \frac{\kappa}{2} (2H)^2 \right]_{\rho=\frac{l}{2}} . \tag{F.8}$$

Here the mean curvature is equivalent to $H = \frac{1}{2} C^\rho_{\ \rho}$. The found result agrees with what has been reported in [192] and [139].

APPENDIX

SELF-CONSISTENT SOLUTION FOR THE MEMBRANE-CORTEX LAYER

G

A description for the coupled cell membrane-cortex layer is introduced in chapter 4 that combines four relatively basic physical concepts for the cell membrane and cell cortex to a closed system of equations. These four concepts involve the mechanics of membrane buckling, force balance at the cell surface, a membrane area elasticity due to fluctuations and a volume elasticity, modulated by an equilibrating chemical potential of water. The closed equation system takes the form

$$A = N_\mathrm{l}\pi\rho_\mathrm{l}^2\left[\frac{k_\mathrm{B}\mathcal{T}}{8\pi\kappa}\log\left(\frac{\kappa q_\mathrm{max}^2+\gamma}{\kappa q_\mathrm{min}^2+\gamma}\right)+1\right]^{-1}, \tag{G.1}$$

$$\Delta p = k_\mathrm{B}\mathcal{T}\frac{N_\mathrm{int}}{\frac{4}{3}\pi R^3+N_\mathrm{p}V_\mathrm{p}}-\Pi_\mathrm{ext}, \tag{G.2}$$

$$\Delta p = 2\frac{T+\gamma_\parallel}{R}, \tag{G.3}$$

$$\gamma = \gamma(R, A, \Delta p, f, N_\mathrm{p}), \tag{G.4}$$

$$\gamma_\parallel = \gamma_\parallel(R, A, \Delta p, f, N_\mathrm{p}), \tag{G.5}$$

$$V_\mathrm{p} = V_\mathrm{p}(R, A, \Delta p, f, N_\mathrm{p}). \tag{G.6}$$

Here N_l is the number of lipids, N_p the number of protrusions, N_int the number of solute particles inside the cell, Π_ext the external osmotic pressure, T the cortex tension and f a local force exerted by cortex filaments onto the cell membrane. If these quantities are known, this equation system determines the global cell properties pressure difference Δp, surface tension γ, radius R, volume V and surface area A self-consistently.

Numerical solution

The equation system (G.1) – (G.6) can, in general, only be solved numerically. This is, on the one hand, owed the fact that the full information on membrane buckling, given by the relations (G.4), (G.5) and (G.6), is obtained numerically (see chapter 3 and appendix D for details). On the other hand, relation (G.1) would lead, in any case, to a transcendental relation, which can only be solved implicitly. However, the equation system can be simplified for the numerical evaluation because for the quantities γ, $\gamma_{||}$ and V_p explicit expressions are known. Hence, only three equations must be solved simultaneously. They can be obtained by plugging (G.4) into (G.1), (G.5) into (G.3) and (G.6) into (G.2). For this work the remaining set of equations is solved with the built-in function `FindRoot` of MATHEMATICA. Furthermore, with the function `Interpolation` the numerical results for γ, $\gamma_{||}$ and V_p are interpolated in order to enable the numerical evaluation.

Analytical solution for zero cortex tension

For zero cortex tension, $T = 0$, on the one hand, the force balance (G.3) turns into Laplace's law, relating the cell radius R_0 and lateral membrane tension $\gamma_{||_0}$ to the cell pressure Δp_0. On the other hand, if

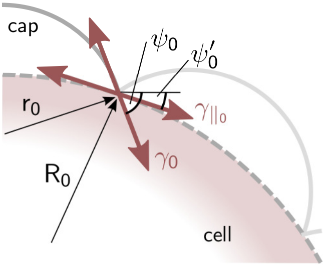

Figure G.1 | Schematic of the geometrical relations between spherical cap membrane protrusion and cell cortex. R_0 is the apparent cell radius, r_0 the cap radius, γ_0 the membrane surface tension, $\gamma_{\|0}$ the lateral membrane tension and ψ_0, ψ_0' tilt angles between the tensions and the ρ-axis.

the membrane protrusions, which form due to buckling, are treated as spherical caps (see section E.2), also each protrusion has to obey Laplace's law in the form (E.20) on page 187, relating the protrusion radius r_0 and membrane surface tension γ_0 to the pressure difference $\Delta p_0'$. Since the pressure difference has to take the same value in both cases, *i.e.*, $\Delta p_0 = \Delta p_0'$, it follows:

$$\frac{\gamma}{r_0} = \frac{\gamma_{\|0}}{R_0} = \cos\left(\psi_0 - \psi_0'\right)\frac{\gamma_0}{R_0}. \tag{G.7}$$

Here $\gamma_{\|0}$ is projected to the spherical cortex (see Figure G.1). Equation (G.7) can only be satisfied if $R_0 = r_0$ and $\psi_0 = \psi_0'$. That means the cap becomes a portion of the underlying sphere or, in other words, the cell membrane does not buckle for $T = 0$.

For an unbuckled membrane which is flat attached to the underlying cortex the equation system (G.1) – (G.6) becomes particularly simple as then $V_\mathrm{p} = 0$ and $\gamma_0 = \gamma_{\|0}$. Hence, Δp_0 in (G.2) can be replaced via (G.3) by R_0 and γ_0. Furthermore, $A_0 = 4\pi R_0^2$ and $V_0 = 4\pi R_0^3/3$ in (G.1) and (G.2), respectively. Equations (G.2) can then be solved for the surface tension

$$\gamma_0 = \frac{3k_\mathrm{B}\mathcal{T}N_\mathrm{int} - 4\pi R_0^3\,\Pi_\mathrm{ext}}{8\pi R_0^2} \tag{G.8}$$

and R_0 is implicitly determined via (G.1) by the relation

$$\frac{N_\mathrm{l}\rho_\mathrm{l}^2}{4R_0^2} = 1 + \frac{k_\mathrm{B}\mathcal{T}}{8\pi\kappa}\log\left[\frac{3k_\mathrm{B}\mathcal{T}N_\mathrm{int} + 8\pi\kappa q_\mathrm{max}^2 R_0^2 - 4\pi\Pi_\mathrm{ext}R_0^3}{3k_\mathrm{B}\mathcal{T}N_\mathrm{int} + 8\pi\kappa q_\mathrm{min}^2 R_0^2 - 4\pi\Pi_\mathrm{ext}R_0^3}\right]. \tag{G.9}$$

Area and volume elasticity for small cortex tensions

In contrast to the case $T = 0$, where the cell membrane is flat attached to the underlying cortex, for $T > 0$ the numerical solution of (G.1) – (G.6) predicts for biological relevant parameters a buckling of the cell membrane into small protrusions. This is discussion in more detail in section 4.2.2. There it is also stated that in order to enable buckling it is necessary that the cell exhibits a finite volume or area elasticity, represented by (G.1) and (G.2), respectively. For very small cortex tensions these elasticities can be estimated analytically by expanding (G.1) and (G.2) around the initial spherical shape. The result can be written in the form

$$\gamma \approx \gamma_0 + K_A\frac{A_0 - A}{A_0}, \tag{G.10}$$

$$\Delta p \approx \Delta p_0 + K_V\frac{V_0 - V}{V_0} \tag{G.11}$$

with the respective area elasticity and volume elasticity

$$K_A := -\kappa\,\alpha\frac{A_\mathrm{b}}{A_0}\frac{\left(q_\mathrm{max}^2 - q_\mathrm{min}^2\right)e^{\alpha(1+A_\mathrm{b}/A_0)}}{\left(e^\alpha - e^{\alpha A_\mathrm{b}/A_0}\right)^2}, \tag{G.12}$$

$$K_V := k_\mathrm{B}\mathcal{T}\frac{N_\mathrm{int}}{V_0}, \tag{G.13}$$

where $\alpha := 8\pi\kappa/k_\mathrm{B}\mathcal{T}$ and $A_\mathrm{b} = N_\mathrm{l}\pi\rho_\mathrm{l}^2$. The quantities A_0, V_0, γ_0 and Δp_0 correspond to those found in the limit $T \to 0$.

REFERENCES

[1] G. W. C. Kaye and T. H. Laby. *Tables of physical and chemical constants.* Longman, Harlow, 16th ed. (1995)

[2] H. Goldmann. *Spaltlampenphotographie und –photometric.* Ophthalmologica **98**, 257–270 (1939)

[3] A. Nwaneshiudu, C. Kuschal, F. H. Sakamoto, R. R. Anderson, K. Schwarzenberger, and R. C. Young. *Introduction to confocal microscopy.* Journal of Investigative Dermatology **132**, e3 (2012)

[4] P. Vesely. *Handbook of biological confocal microscopy.* Scanning **29**, 91–91 (2007)

[5] D. Kruger, P. Schneck, and H. Gelderblom. *Helmut ruska and the visualisation of viruses.* The Lancet **355**, 1713–1717 (2000)

[6] H. G. Rudenberg and P. G. Rudenberg. *Chapter 6 - Origin and background of the invention of the electron microscope: Commentary and expanded notes on memoir of reinhold rüdenberg.* In *Advances in Imaging and Electron Physics*, 207–286. Elsevier (2010)

[7] R. F. Egerton. *Physical principles of electron microscopy: an introduction to TEM, SEM, and AEM.* Springer, New York (2005)

[8] R. Hooke, J. Martyn, and J. Allestry. *Micrographia or some physiological descriptions of minute bodies made by magnifying glasses with observations and inquiries thereupon.* Royal Society (1665)

[9] B. Alberts, A. Johnson, J. Lewis, M. Raff, K. Roberts, and P. Walter. *Molecular biology of the cell.* Garland Science, 4th ed. (2002)

[10] C. R. Woese, O. Kandler, and M. L. Wheelis. *Towards a natural system of organisms: proposal for the domains archaea, bacteria, and eucarya.* Proceedings of the National Academy of Sciences **87**, 4576–4579 (1990)

[11] A. G. Clark, K. Dierkes, and E. K. Paluch. *Monitoring actin cortex thickness in live cells.* Biophysical Journal **105**, 570–580 (2015)

[12] J. Hanson and J. Lowy. *The structure of f-actin and of actin filaments isolated from muscle.* Journal of Molecular Biology **6**, 46–60 (1963)

[13] N. Morone, T. Fujiwara, K. Murase, R. S. Kasai, H. Ike, S. Yuasa, J. Usukura, and A. Kusumi. *Three-dimensional reconstruction of the membrane skeleton at the plasma membrane interface by electron tomography.* The Journal of Cell Biology **174**, 851–862 (2006)

[14] G. Charras, C.-K. Hu, M. Coughlin, and T. Mitchison. *Reassembly of contractile actin cortex in cell blebs.* Journal of Cell Biology **175**, 477–490 (2006)

[15] F. Gittes, B. Mickey, J. Nettleton, and J. Howard. *Flexural rigidity of microtubules and actin filaments measured from thermal fluctuations in shape.* The Journal of Cell Biology **120**, 923–934 (1993)

[16] G. Salbreux, G. Charras, and E. Paluch. *Actin cortex mechanics and cellular morphogenesis.* Trends in Cell Biology (2012)

[17] M. Fritzsche, A. Lewalle, T. Duke, K. Kruse, and G. Charras. *Analysis of turnover dynamics of the submembranous actin cortex.* Molecular Biology of the Cell **24**, 757–767 (2013)

[18] H. Miyata, R. Yasuda, and K. Kinosita Jr. *Strength and lifetime of the bond between actin and skeletal muscle α-actinin studied with an optical trapping technique.* Biochimica et Biophysica Acta **1290**, 83–88 (1996)

[19] S. Mukhina, Y. li Wang, and M. Murata-Hori. *α-actinin is required for tightly regulated remodeling of the actin cortical network during cytokinesis.* Developmental Cell **13**, 554–565 (2007)

[20] D. Bray and J. White. *Cortical flow in animal cells.* Science **239**, 883–888 (1988)

[21] O. Thoumine and A. Ott. *Time scale dependent viscoelastic and contractile regimes in fibroblasts probed by microplate manipulation.* Journal of Cell Science **110**, 2109–2116 (1997)

[22] G. Forgacs, R. A. Foty, Y. Shafrir, and M. S. Steinberg. *Viscoelastic properties of living embryonic tissues: a quantitative study.* Biophysical Journal **74**, 2227–2234 (1998)

[23] M. J. Tyska and D. M. Warshaw. *The myosin power stroke.* Cell Motility and the Cytoskeleton **51**, 1–15 (2002)

[24] J. Peukes and T. Betz. *Direct measurement of the cortical tension during the growth of membrane blebs.* Biophysical Journal **107**, 1810–1820 (2014)

[25] M. Mayer, M. Depken, J. S. Bois, F. Julicher, and S. W. Grill. *Anisotropies in cortical tension reveal the physical basis of polarizing cortical flows.* Nature **467**, 617–621 (2010)

[26] J. Sedzinski, M. Biro, A. Oswald, J.-Y. Tinevez, G. Salbreux, and E. Paluch. *Polar actomyosin contractility destabilizes the position of the cytokinetic furrow.* Nature **476**, 462–466 (2011)

[27] J.-F. Joanny and J. Prost. *Active gels as a description of the actin-myosin cytoskeleton.* Human Frontier Science Program Journal **3**, 94–104 (2009)

[28] A. G. Clark, O. Wartlick, G. Salbreux, and E. K. Paluch. *Stresses at the cell surface during animal cell morphogenesis.* Current Biology **24**, R484–R494 (2014)

[29] F. C. Sauer. *Mitosis in the neural tube.* The Journal of Comparative Neurology **62**, 377–405 (1935)

[30] M. P. Stewart, J. Helenius, Y. Toyoda, S. P. Ramanathan, D. J. Muller, and A. A. Hyman. *Hydrostatic pressure and the actomyosin cortex drive mitotic cell rounding.* Nature **469**, 226–230 (2011)

[31] S. P. Ramanathan, J. Helenius, M. P. Stewart, C. J. Cattin, A. A. Hyman, and D. J. Muller. *Cdk1-dependent mitotic enrichment of cortical myosin ii promotes cell rounding against confinement.* Nature Cell Biology **17**, 148–159 (2015)

[32] G. Charras and E. Paluch. *Blebs lead the way: how to migrate without lamellipodia.* Nature Reviews Molecular Cell Biology **9**, 730–736 (2008)

[33] M. Bergert, A. Erzberger, R. A. Desai, I. M. Aspalter, A. C. Oates, G. Charras, G. Salbreux, and E. K. Paluch. *Force transmission during adhesion-independent migration.* Nature Cell Biology **17**, 524–529 (2015)

[34] S. R. Naganathan, S. Fürthauer, M. Nishikawa, F. Jülicher, and S. W. Grill. *Active torque generation by the actomyosin cell cortex drives left–right symmetry breaking.* eLife **3** (2014)

[35] R. Farhadifar, J.-C. Röper, B. Aigouy, S. Eaton, and F. Jülicher. *The influence of cell mechanics, cell-cell interactions, and proliferation on epithelial packing.* Current Biology **17**, 2095–2104 (2007)

[36] R. Etournay, M. Popović, M. Merkel, A. Nandi, C. Blasse, B. Aigouy, H. Brandl, G. Myers, G. Salbreux, F. Jülicher, S. Eaton, and H. McNeill.

Interplay of cell dynamics and epithelial tension during morphogenesis of the drosophila pupal wing. eLife (2015)

[37] K. Dierkes, A. Sumi, J. Solon, and G. Salbreux. *Spontaneous oscillations of elastic contractile materials with turnover.* Physical Review Letters **113**, 148102 (2014)

[38] L. Saias, J. Swoger, A. D'Angelo, P. Hayes, J. Colombelli, J. Sharpe, G. Salbreux, and J. Solon. *Decrease in cell volume generates contractile forces driving dorsal closure.* Developmental Cell **33**, 611–621 (2015)

[39] G. Karp. *Cell and molecular biology: concepts and experiments.* Wiley, Hoboken, 5th ed. (2008)

[40] A. Krogh, B. Larsson, G. von Heijne, and E. L. Sonnhammer. *Predicting transmembrane protein topology with a hidden markov model: application to complete genomes.* Journal of Molecular Biology **305**, 567–580 (2001)

[41] B. Hille. *Ion channels of excitable membranes.* Sinauer Assoc., Sunderland, Mass., 3rd ed. (2001)

[42] S. Mukherjee, R. N. Ghosh, and F. R. Maxfield. *Endocytosis.* Physiological Reviews **77**, 759–803 (1997)

[43] B. Razani, S. E. Woodman, and M. P. Lisanti. *Caveolae: From cell biology to animal physiology.* Pharmacological Reviews **54**, 431–467 (2002)

[44] M. Algrain, O. Turunen, A. Vaheri, D. Louvard, and M. Arpin. *Ezrin contains cytoskeleton and membrane binding domains accounting for its proposed role as a membrane-cytoskeletal linker.* The Journal of Cell Biology **120**, 129–139 (1993)

[45] R. G. Fehon, A. I. McClatchey, and A. Bretscher. *Organizing the cell cortex: the role of erm proteins.* Nature Reviews Molecular Cell Biology **11**, 276–287 (2010)

[46] M. P. Sheetz. *Cell control by membrane–cytoskeleton adhesion.* Nature Reviews Molecular Cell Biology **2**, 392–396 (2001)

[47] M. Fritzsche, R. Thorogate, and G. Charras. *Quantitative analysis of ezrin turnover dynamics in the actin cortex.* Biophysical Journal **106**, 343–353 (2014)

[48] F. Brochard and J. Lennon. *Frequency spectrum of the flicker phenomenon in erythrocytes.* J. Phys. France **36**, 1035–1047 (1975)

[49] E. Sackmann, J. Engelhardt, K. Fricke, and H. Gaub. *On dynamic molecular and elastic properties of lipid bilayers and biological membranes.* Colloids and Surfaces **10**, 321–335 (1984)

[50] T. Betz and C. Sykes. *Time resolved membrane fluctuation spectroscopy.* Soft Matter **8**, 5317–5326 (2012)

[51] S. Levin and R. Korenstein. *Membrane fluctuations in erythrocytes are linked to mgatp-dependent dynamic assembly of the membrane skeleton.* Biophysical Journal **60**, 733–737 (1991)

[52] S. Tuvia, S. Levin, A. Bitler, and R. Korenstein. *Mechanical fluctuations of the membrane–skeleton are dependent on f-actin atpase in human erythrocytes.* The Journal of Cell Biology **141**, 1551–1561 (1998)

[53] J.-B. Manneville, P. Bassereau, S. Ramaswamy, and J. Prost. *Active membrane fluctuations studied by micropipet aspiration.* Physical Review E **64**, 021908 (2001)

[54] N. Gov. *Membrane undulations driven by force fluctuations of active proteins.* Physical Review Letters **93**, 268104 (2004)

[55] A. C. Woodka, P. D. Butler, L. Porcar, B. Farago, and M. Nagao. *Lipid bilayers and membrane dynamics: Insight into thickness fluctuations.* Physical Review Letters **109**, 058102 (2012)

[56] H. M. McConnell and R. D. Kornberg. *Inside-outside transitions of phospholipids in vesicle membranes.* Biochemistry **10**, 1111–1120 (1971)

[57] F. Kamp and J. A. Hamilton. *ph gradients across phospholipid membranes caused by fast flip-flop of un-ionized fatty acids.* Proceedings of the National Academy of Sciences **89**, 11367–11370 (1992)

[58] F. Kamp, D. Zakim, F. Zhang, N. Noy, and J. A. Hamilton. *Fatty acid flip-flop in phospholipid bilayers is extremely fast.* Biochemistry **34**, 11928–11937 (1995)

[59] T. Fujiwara, K. Ritchie, H. Murakoshi, K. Jacobson, and A. Kusumi. *Phospholipids undergo hop diffusion in compartmentalized cell membrane.* The Journal of Cell Biology **157**, 1071–1082 (2002)

[60] G. Lindblom and G. Orädd. *Lipid lateral diffusion and membrane heterogeneity.* Biochimica et Biophysica Acta **1788**, 234–244 (2009)

[61] J. Lippincott-Schwartz, E. Snapp, and A. Kenworthy. *Studying protein dynamics in living cells.* Nature Reviews Molecular Cell Biology **2**, 444–456 (2001)

[62] K. Schmidt and B. J. Nichols. *A barrier to lateral diffusion in the cleavage furrow of dividing mammalian cells.* Current Biology **14**, 1002–1006 (2004)

[63] S. J. Singer and G. L. Nicolson. *The fluid mosaic model of the structure of cell membranes.* Science **175**, 720–731 (1972)

[64] A. Kusumi and Y. Sako. *Cell surface organization by the membrane skeleton.* Current Opinion in Cell Biology **8**, 566–574 (1996)

[65] A. Kusumi, C. Nakada, K. Ritchie, K. Murase, K. Suzuki, H. Murakoshi, R. S. Kasai, J. Kondo, and T. Fujiwara. *Paradigm shift of the plasma membrane concept from the two-dimensional continuum fluid to the partitioned fluid: High-speed single-molecule tracking of membrane molecules.* Annual Review of Biophysics and Biomolecular Structure **34**, 351–378 (2005)

[66] K. Suzuki, K. Ritchie, E. Kajikawa, T. Fujiwara, and A. Kusumi. *Rapid hop diffusion of a g-protein-coupled receptor in the plasma membrane as revealed by single-molecule techniques.* Biophysical Journal **88**, 3659–3680 (2005)

[67] R. D. Allen. *Fine structure of membranous and microfibrillar systems in the cortex of paramecium caudatum.* The Journal of Cell Biology **49**, 1–20 (1971)

[68] E. A. C. Follett and R. D. Goldman. *The occurrence of microvilli during spreading and growth of bhk21/c13 fibroblasts.* Experimental Cell Research **59**, 124–136 (1970)

[69] S. J. Burwen and B. H. Satir. *Plasma membrane folds on the mast cell surface and their relationship to secretory activity.* The Journal of Cell Biology **74**, 690–697 (1977)

[70] M. P. Sheetz, J. E. Sable, and H.-G. Döbereiner. *Continuous membrane-cytoskeleton adhesion requires continuous accommodation to lipid and cytoskeleton dynamics.* Annual Review of Biophysics and Biomolecular Structure **35**, 417–434 (2006)

[71] S. Mayor. *Need tension relief fast? Try caveolae.* Cell **144**, 323–324 (2011)

[72] B. Sinha, D. Köster, R. Ruez, P. Gonnord, M. Bastiani, D. Abankwa, R. V. Stan, G. Butler-Browne, B. Vedie, L. Johannes, N. Morone, R. G. Parton, G. Raposo, P. Sens, C. Lamaze, and P. Nassoy. *Cells respond to mechanical stress by rapid disassembly of caveolae.* Cell **144**, 402–413 (2011)

[73] P. Sens and M. S. Turner. *Budded membrane microdomains as tension regulators.* Physical Review E **73**, 031918 (2006)

[74] D. Raucher and M. P. Sheetz. *Characteristics of a membrane reservoir buffering membrane tension.* Biophysical Journal **77**, 1992–2002 (1999)

[75] N. Groulx, F. Boudreault, S. Orlov, and R. Grygorczyk. *Membrane reserves and hypotonic cell swelling.* Journal of Membrane Biology **214**, 43–56 (2006)

[76] C. Morris and U. Homann. *Cell surface area regulation and membrane tension.* Journal of Membrane Biology **179**, 79–102 (2001)

[77] L. Figard and A. M. Sokac. *A membrane reservoir at the cell surface: Unfolding the plasma membrane to fuel cell shape change.* Bioarchitecture **4**, 39–46 (2014)

[78] R. M. Steinman, I. S. Mellman, W. A. Muller, and Z. A. Cohn. *Endocytosis and the recycling of plasma membrane.* The Journal of Cell Biology **96**, 1–27 (1983)

[79] J. Wolfe and P. L. Steponkus. *Mechanical properties of the plasma membrane of isolated plant protoplasts: Mechanism of hyperosmotic and extracellular freezing injury.* Plant Physiology **71**, 276–285 (1983)

[80] E. Boucrot and T. Kirchhausen. *Endosomal recycling controls plasma membrane area during mitosis.* Proceedings of the National Academy of Sciences **104**, 7939–7944 (2007)

[81] L. Thilo and G. Vogel. *Kinetics of membrane internalization and recycling during pinocytosis in dictyostelium discoideum.* Proceedings of the National Academy of Sciences of the United States of America **77** (1980)

[82] N. C. Gauthier, M. A. Fardin, P. Roca-Cusachs, and M. P. Sheetz. *Temporary increase in plasma membrane tension coordinates the activation of exocytosis and contraction during cell spreading.* Proceedings of the National Academy of Sciences **108**, 14467–14472 (2011)

[83] H. Harris. *The Birth of the Cell.* Yale University Press (2000)

[84] S. J. Morrison and J. Kimble. *Asymmetric and symmetric stem-cell divisions in development and cancer.* Nature **441**, 1068–1074 (2006)

[85] H. T. K. Tse, W. M. Weaver, and D. Di Carlo. *Increased asymmetric and multi-daughter cell division in mechanically confined microenvironments.* PLoS ONE **7**, e38986 (2012)

[86] P. Kunda and B. Baum. *The actin cytoskeleton in spindle assembly and positioning.* Trends in Cell Biology **19**, 174–179 (2009)

[87] S. Carreno, I. Kouranti, E. S. Glusman, M. T. Fuller, A. Echard, and F. Payre. *Moesin and its activating kinase slik are required for cortical stability and microtubule organization in mitotic cells.* The Journal of Cell Biology **180**, 739–746 (2008)

[88] C. E. Walczak and R. Heald. *Chapter 3 - Mechanisms of mitotic spindle assembly and function.* In *A Survey of Cell Biology*, *International Review of Cytology*, vol. 265, 111–158. Academic Press (2008)

[89] J. Brugués and D. Needleman. *Physical basis of spindle self-organization.* Proceedings of the National Academy of Sciences **111**, 18496–18500 (2014)

[90] C. Luxenburg, H. Amalia Pasolli, S. E. Williams, and E. Fuchs. *Developmental roles for srf, cortical cytoskeleton and cell shape in epidermal spindle orientation.* Nature Cell Biology **13**, 203–214 (2011)

[91] O. M. Lancaster, M. L. Berre, A. Dimitracopoulos, D. Bonazzi, E. Zlotek-Zlotkiewicz, R. Picone, T. Duke, M. Piel, and B. Baum. *Mitotic rounding alters cell geometry to ensure efficient bipolar spindle formation.* Developmental Cell **25**, 270 – 283 (2013)

[92] J. R. McIntosh, E. L. Grishchuk, and R. R. West. *Chromosome-microtubule interactions durin mitosis.* Annual Review of Cell and Developmental Biology **18**, 193–219 (2002)

[93] S. Dumont. *Chromosome segregation: Spindle mechanics come to life.* Current Biology **21**, R688–R690 (2011)

[94] L. G. Cao and Y. L. Wang. *Signals from the spindle midzone are required for the stimulation of cytokinesis in cultured epithelial cells.* Molecular Biology of the Cell **7**, 225–232 (1996)

[95] S. Oliferenko, T. G. Chew, and M. K. Balasubramanian. *Positioning cytokinesis.* Genes & Development **23**, 660–674 (2009)

[96] C. Cabernard, K. E. Prehoda, and C. Q. Doe. *A spindle-independent cleavage furrow positioning pathway.* Nature **467**, 91–94 (2010)

[97] T. E. Schroeder. *Cell constriction: Contractile role of microfilaments in division and development.* American Zoologist **13**, 949–960 (1973)

[98] L. G. Cao and Y. L. Wang. *Mechanism of the formation of contractile ring in dividing cultured animal cells. i. recruitment of preexisting actin filaments into the cleavage furrow.* The Journal of Cell Biology **110**, 1089–1095 (1990)

[99] D. N. Robinson and J. A. Spudich. *Towards a molecular understanding of cytokinesis.* Trends in Cell Biology **10**, 228–237 (2000)

[100] K. Murthy and P. Wadsworth. *Myosin-ii-dependent localization and dynamics of f-actin during cytokinesis.* Current Biology **15**, 724–731 (2005)

[101] H. Turlier, B. Audoly, J. Prost, and J.-F. Joanny. *Furrow constriction in animal cell cytokinesis.* Biophysical Journal **106**, 114–123 (2014)

[102] W. Greiner, D. Rischke, L. Neise, and H. Stöcker. *Thermodynamics and Statistical Mechanics.* Springer, New York (2000)

[103] T. Young. *An essay on the cohesion of fluids.* Philosophical Transactions of the Royal Society of London **95**, 65–87 (1805)

[104] P. S. d. Laplace. *Traité de mécanique céleste.* Duprat, Paris (1799)

[105] S. K. Feller (Editor). *Computational Modeling of Membrane Bilayers*, vol. 60. Elsevier, Amsterdam (2008)

[106] P. B. Canham. *The minimum energy of bending as a possible explanation of the biconcave shape of the human red blood cell.* Journal of Theoretical Biology **26**, 61–81 (1970)

[107] S. Svetina and B. Žekš. *Membrane bending energy and shape determination of phospholipid vesicles and red blood cells.* European Biophysics Journal **17**, 101–111 (1989)

[108] R. Lipowsky. *The conformation of membranes.* Nature **349**, 475–481 (1991)

[109] F. Jülicher. *Die Morphologie von Vesikeln.* Ph.D. thesis, University of Cologne (1994)

[110] W. Helfrich. *Elastic properties of lipid bilayers: Theory and possible experiments.* Zeitschrift für Naturforschung **28c**, 693–703 (1973)

[111] E. A. Evans. *Bending resistance and chemically induced moments in membrane bilayers.* Biophysical Journal **14**, 923–931 (1974)

[112] R. Dimova. *Recent developments in the field of bending rigidity measurements on membranes.* Advances in Colloid and Interface Science **208**, 225–234 (2014)

[113] W. Helfrich. *Blocked lipid exchange in bilayers and its possible influence on the shape of vesicles.* Zeitschrift für Naturforschung **29c**, 510–515 (1974)

[114] U. Seifert. *Configurations of fluid membranes and vesicles.* Advances in Physics **46**, 13–137 (1997)

[115] O.-Y. Zhong-can and W. Helfrich. *Instability and deformation of a spherical vesicle by pressure.* Physical Review Letters **59**, 2486–2488 (1987)

[116] I. Derényi, F. Jülicher, and J. Prost. *Formation and interaction of membrane tubes.* Physical Review Letters **88**, 238101 (2002)

[117] E. Hannezo, J. Prost, and J.-F. Joanny. *Mechanical instabilities of biological tubes.* Physical Review Letters **109**, 018101 (2012)

[118] M. Raatz, R. Lipowsky, and T. R. Weikl. *Cooperative wrapping of nanoparticles by membrane tubes.* Soft Matter **10**, 3570–3577 (2014)

[119] X. Liang, Y. Zu, Y.-P. Cao, and C. Yang. *A dual-scale model for the caveolin-mediated vesiculation.* Soft Matter **9**, 7981–7987 (2013)

[120] M. P. do Carmo. *Differential geometry of curves and surfaces.* Prentice Hall, Englewood Cliffs (1976)

[121] E. P. Petrov, S. Arumugam, J. Ehrig, and P. Schwille. *Cytoskeletal pinning prevents large-scale phase separation in model membranes.* Biophysical Journal **104**, 252a (2013)

[122] L. J. Pike. *The challenge of lipid rafts.* Journal of Lipid Research **50**, S323–S328 (2009)

[123] E. Glassinger and R. M. Raphael. *Influence of thermally driven surface undulations on tethers formed from bilayer membranes.* Biophysical Journal **91**, 619–625 (2006)

[124] E. Evans and A. Yeung. *Special issue functional dynamics of lipids in biomembranes hidden dynamics in rapid changes of bilayer shape.* Chemistry and Physics of Lipids **73**, 39–56 (1994)

[125] U. Seifert and S. A. Langer. *Viscous modes of fluid bilayer membranes.* Europhysics Letters **23**, 71 (1993)

[126] M. A. Peterson, H. Strey, and E. Sackmann. *Theoretical and phase contrast microscopic eigenmode analysis of erythrocyte flicker: amplitudes.* Journal de Physique II **2**, 1273–1285 (1992)

[127] M. B. Schneider, J. T. Jenkins, and W. W. Webb. *Thermal fluctuations of large quasi-spherical bimolecular phospholipid vesicles.* Journal de Physique **45**, 1457–1472 (1984)

[128] S. T. Milner and S. A. Safran. *Dynamical fluctuations of droplet microemulsions and vesicles.* Physical Review A **36**, 4371–4379 (1987)

[129] M. A. Peterson. *Shape fluctuations of red blood cells.* Molecular Crystals and Liquid Crystals **127**, 159–186 (1985)

[130] J. Paulose, G. A. Vliegenthart, G. Gompper, and D. R. Nelson. *Fluctuating shells under pressure.* Proceedings of the National Academy of Sciences **109**, 19551–19556 (2012)

[131] A. Gholami, M. Enculescu, and M. Falcke. *Membrane waves driven by forces from actin filaments.* New Journal of Physics **14**, 115002 (2012)

[132] B. Loubet, U. Seifert, and M. A. Lomholt. *Effective tension and fluctuations in active membranes.* Physical Review E **85**, 031913 (2012)

[133] N. Gov and S. A. Safran. *Pinning of fluid membranes by periodic harmonic potentials.* Physical Review E **69**, 011101 (2004)

[134] W. Choi, J. Yi, and Y. W. Kim. *Fluctuations of red blood cell membranes: The role of the cytoskeleton.* Physical Review E **92**, 012717 (2015)

[135] W. Helfrich. *Effect of thermal undulations on the rigidity of fluid membranes and interfaces.* Journal de Physique **46**, 1263–1268 (1985)

[136] L. Peliti and S. Leibler. *Effects of thermal fluctuations on systems with small surface tension.* Physical Review Letters **54**, 1690–1693 (1985)

[137] F. David and S. Leibler. *Vanishing tension of fluctuating membranes.* J. Phys. II France **1**, 959–976 (1991)

[138] W. Helfrich and R.-M. Servuss. *Undulations, steric interaction and cohesion of fluid membranes.* Il Nuovo Cimento D **3**, 137–151 (1984)

[139] J.-B. Fournier and C. Barbetta. *Direct calculation from the stress tensor of the lateral surface tension of fluctuating fluid membranes.* Physical Review Letters **100**, 078103 (2008)

[140] R. Courant and D. Hilbert. *The Calculus of Variations*, 164–274. Wiley-VCH, Weinheim (1989)

[141] O.-Y. Zhong-can and W. Helfrich. *Bending energy of vesicle membranes: General expressions for the first, second, and third variation of the shape energy and applications to spheres and cylinders.* Physical Review A **39**, 5280–5288 (1989)

[142] E. J. Post. *Formal Structure of Electromagnetics: General Covariance and Electromagnetics.* Dover Publications, Mineola (1997)

[143] F. L. Brown. *Elastic modeling of biomembranes and lipid bilayers.* Annual Review of Physical Chemistry **59**, 685–712 (2008)

[144] M. Deserno and T. Bickel. *Wrapping of a spherical colloid by a fluid membrane.* Europhysics Letters **62**, 767 (2003)

[145] T. R. Powers, G. Huber, and R. E. Goldstein. *Fluid-membrane tethers: Minimal surfaces and elastic boundary layers.* Physical Review E **65**, 041901 (2002)

[146] W. Cai and T. C. Lubensky. *Covariant hydrodynamics of fluid membranes.* Physical Review Letters **73**, 1186–1189 (1994)

[147] J. L. Harden, F. C. MacKintosh, and P. D. Olmsted. *Budding and domain shape transformations in mixed lipid films and bilayer membranes.* Physical Review E **72**, 011903 (2005)

[148] F. Jülicher and U. Seifert. *Shape equations for axisymmetric vesicles: A clarification.* Physical Review E **49**, 4728–4731 (1994)

[149] J. Chen and M. C. Wagner. *Altered membrane-cytoskeleton linkage and membrane blebbing in energy-depleted renal proximal tubular cells.* American Journal of Physiology Renal Physiology **280**, F619–F627 (2001)

[150] M. Simunovic, A. Srivastava, and G. A. Voth. *Linear aggregation of proteins on the membrane as a prelude to membrane remodeling.* Proceedings of the National Academy of Sciences **110**, 20396–20401 (2013)

[151] G. J. Doherty and H. T. McMahon. *Mediation, modulation, and consequences of membrane-cytoskeleton interactions.* Annual Review of Biophysics **37**, 65–95 (2008)

[152] G. Lim H. W., M. Wortis, and R. Mukhopadhyay. *Stomatocyte–discocyte–echinocyte sequence of the human red blood cell: Evidence for the bilayer–couple hypothesis from membrane mechanics.* Proceedings of the National Academy of Sciences **99**, 16766–16769 (2002)

[153] N. Sarkar and A. Basu. *Instabilities and diffusion in a hydrodynamic model of a fluid membrane coupled to a thin active fluid layer.* The European Physical Journal E **35**, 1–14 (2012)

[154] R. Alert, J. Casademunt, J. Brugués, and P. Sens. *Model for probing membrane-cortex adhesion by micropipette aspiration and fluctuation spectroscopy.* Biophysical Journal **108**, 1878–1886 (2015)

[155] P. Sens and N. Gov. *Force balance and membrane shedding at the red-blood-cell surface.* Physical Review Letters **98**, 018102 (2007)

[156] L. C.-L. Lin and F. L. H. Brown. *Dynamics of pinned membranes with application to protein diffusion on the surface of red blood cells.* Biophysical Journal **86**, 764–780 (2004)

[157] J.-B. Fournier, D. Lacoste, and E. Raphaël. *Fluctuation spectrum of fluid membranes coupled to an elastic meshwork: Jump of the effective surface tension at the mesh size.* Physical Review Letters **92**, 018102 (2004)

[158] R.-J. Merath and U. Seifert. *Nonmonotonic fluctuation spectra of membranes pinned or tethered discretely to a substrate.* Physical Review E **73**, 010401 (2006)

[159] K. Gowrishankar, S. Ghosh, S. Saha, R. C., S. Mayor, and M. Rao. *Active remodeling of cortical actin regulates spatiotemporal organization of cell surface molecules.* Cell **149**, 1353–1367 (2012)

[160] F. Heinemann, S. Vogel, and P. Schwille. *Lateral membrane diffusion modulated by a minimal actin cortex.* Biophysical Journal **104**, 1465–1475 (2013)

[161] B. B. Machta, S. Papanikolaou, J. P. Sethna, and S. L. Veatch. *Minimal model of plasma membrane heterogeneity requires coupling cortical actin to criticality.* Biophysical Journal **100**, 1668–1677 (2011)

[162] A. Honigmann, S. Sadeghi, J. Keller, S. W. Hell, C. Eggeling, R. Vink, and R. Schekman. *A lipid bound actin meshwork organizes liquid phase separation in model membranes.* eLife **3** (2014)

[163] R. Shlomovitz and N. S. Gov. *Membrane waves driven by actin and myosin.* Physical Review Letters **98**, 168103 (2007)

[164] Lim, F. Y., Chiam, K.-H., and Mahadevan, L. *The size, shape, and dynamics of cellular blebs.* Europhysics Letters **100**, 28004 (2012)

[165] G. T. Charras. *A short history of blebbing.* Journal of Microscopy **231**, 466–478 (2008)

[166] J.-Y. Tinevez, U. Schulze, G. Salbreux, J. Roensch, J.-F. Joanny, and E. Paluch. *Role of cortical tension in bleb growth.* Proceedings of the National Academy of Sciences **106**, 18581–18586 (2009)

[167] A. P. Liu, D. L. Richmond, L. Maibaum, S. Pronk, P. L. Geissler, and D. A. Fletcher. *Membrane-induced bundling of actin filaments.* Nature Physics **4**, 789–793 (2008)

[168] S. A. Rautu, G. Rowlands, and M. S. Turner. *Membrane composition variation and underdamped mechanics near transmembrane proteins and coats.* Physical Review Letters **114**, 098101 (2015)

[169] P. Rangamani, K. K. Mandadap, and G. Oster. *Protein-induced membrane curvature alters local membrane tension.* Biophysical Journal **107**, 751–762 (2014)

[170] R. Lipowsky. *Budding of membranes induced by intramembrane domains.* Journal de Physique II **2**, 1825–1840 (1992)

[171] J. Derganc, B. Antonny, and A. Čopič. *Membrane bending: the power of protein imbalance.* Trends in Biochemical Sciences **38**, 576–584 (2013)

[172] W. Wiese and W. Helfrich. *Theory of vesicle budding.* Journal of Physics: Condensed Matter **2**, SA329 (1990)

[173] M. Kapustina, T. C. Elston, and K. Jacobson. *Compression and dilation of the membrane-cortex layer generates rapid changes in cell shape.* The Journal of Cell Biology **200**, 95–108 (2013)

[174] M. Staykova, D. P. Holmes, C. Read, and H. A. Stone. *Mechanics of surface area regulation in cells examined with confined lipid membranes.* Proceedings of the National Academy of Sciences **108**, 9084–9088 (2011)

[175] M. Staykova, M. Arroyo, M. Rahimi, and H. A. Stone. *Confined bilayers passively regulate shape and stress.* Physical Review Letters **110**, 028101 (2013)

[176] L. Figard, H. Xu, H. G. Garcia, I. Golding, and A. M. Sokac. *The plasma membrane flattens out to fuel cell-surface growth during drosophila cellularization.* Developmental Cell **27**, 648–655 (2013)

[177] M. Lenz, D. J. G. Crow, and J.-F. *Membrane buckling induced by curved filaments.* Physical Review Letters **103**, 038101 (2009)

[178] M. P. Sheetz and J. Dai. *Modulation of membrane dynamics and cell motility by membrane tension.* Trends in Cell Biology **6**, 85–89 (1996)

[179] K. Sliogeryte, S. D. Thorpe, D. A. Lee, L. Botto, and M. M. Knight. *Stem cell differentiation increases membrane-actin adhesion regulating cell blebability, migration and mechanics.* Scientific Reports **4**, 7307 (2014)

[180] R. Lipowsky. *Spontaneous tubulation of membranes and vesicles reveals membrane tension generated by spontaneous curvature.* Faraday Discussions **161**, 305–331 (2013)

[181] L. C.-L. Lin and F. L. H. Brown. *Dynamic simulations of membranes with cytoskeletal interactions.* Physical Review E **72**, 011910 (2005)

[182] J. D. Jackson. *Classical electrodynamics.* Wiley, New York, 3rd ed. (1999)

[183] D. G. Duffy. *Green's Functions with Applications.* CRC Press (2001)

[184] D. Schmidt, C. Monzel, T. Bihr, R. Merkel, U. Seifert, K. Sengupta, and A.-S. Smith. *Signature of a nonharmonic potential as revealed from a consistent shape and fluctuation analysis of an adherent membrane.* Physical Review X **4**, 021023 (2014)

[185] W. H. Press, S. A. Teukolsky, W. T. Vetterling, and B. P. Flannery. *Numerical Recipes 3rd Edition: The Art of Scientific Computing.* Cambridge University Press, New York, 3 ed. (2007)

[186] W. Wiese, W. Harbich, and W. Helfrich. *Budding of lipid bilayer vesicles and flat membranes.* Journal of Physics: Condensed Matter **4**, 1647 (1992)

[187] H. Kusumaatmaja and R. Lipowsky. *Droplet-induced budding transitions of membranes.* Soft Matter **7**, 6914–6919 (2011)

[188] R. Bar-Ziv and E. Moses. *Instability and pearlingßtates produced in tubular membranes by competition of curvature and tension.* Physical Review Letters **73**, 1392–1395 (1994)

[189] T. Zhang, R. Sknepnek, M. J. Bowick, and J. M. Schwarz. *On the modeling of endocytosis in yeast.* Biophysical Journal **108**, 508–519 (2015)

[190] G. Koster, A. Cacciuto, I. Derényi, D. Frenkel, and M. Dogterom. *Force barriers for membrane tube formation.* Physical Review Letters **94**, 068101 (2005)

[191] F. Hochmuth, J. Shao, J. Dai, and M. Sheetz. *Deformation and flow of membrane into tethers extracted from neuronal growth cones.* Biophysical Journal **70**, 358–369 (1996)

[192] J.-B. Fournier. *On the stress and torque tensors in fluid membranes.* Soft Matter **3**, 883–888 (2007)

[193] S. Strogatz. *Nonlinear dynamics and chaos: with applications to physics, biology, chemistry, and engineering.* Westview Press, Boulder, 2nd ed. (2015)

[194] J. H. van't Hoff. *Lois de l'équilibre chemique dans l'état dilué, gazeuz ou dissous.* In *Kongliga Svenska vetenskaps-akademiens handlingar.*, 594. Royal Swedish Society of Sciences, Stockholm (1885)

[195] R. Phillips, J. Kondev, J. Theriot, and H. Garcia. *Physical Biology of the Cell.* Garland Science, New York, 2nd ed. (2012)

[196] C. S. Peskin, G. M. Odell, and G. F. Oster. *Cellular motions and thermal fluctuations: the brownian ratchet.* Biophysical Journal **65**, 316–324 (1993)

[197] M. J. Footer, J. W. J. Kerssemakers, J. A. Theriot, and M. Dogterom. *Direct measurement of force generation by actin filament polymerization using an optical trap.* Proceedings of the National Academy of Sciences **104**, 2181–2186 (2007)

[198] C. Waymouth. *Osmolality of mammalian blood and of media for culture of mammalian cells.* In Vitro **6**, 109–127 (1970)

[199] E. Evans and W. Rawicz. *Entropy-driven tension and bending elasticity in condensed-fluid membranes.* Physical Review Letters **64**, 2094–2097 (1990)

[200] J. Solon, J. Pécréaux, P. Girard, M.-C. Fauré, J. Prost, and P. Bassereau. *Negative tension induced by lipid uptake.* Physical Review Letters **97**, 098103 (2006)

[201] Y. Y. Avital and O. Farago. *Small membranes under negative surface tension.* The Journal of Chemical Physics **142** (2015)

[202] E. Fischer-Friedrich, A. A. Hyman, F. Jülicher, D. J. Müller, and J. Helenius. *Quantification of surface tension and internal pressure generated by single mitotic cells.* Scientific Reports **4**, 6213 (2014)

[203] R. Osserman. *The isoperimetric inequality.* Bulletin of the American Mathematical Society **84**, 1182–1238 (1978)

[204] L. M. Bond, D. A. Tumbarello, J. Kendrick-Jones, and F. Buss. *Small-molecule inhibitors of myosin proteins.* Future Medicinal Chemistry **5**, 41–52 (2012)

[205] E. Evans and K. Ritchie. *Dynamic strength of molecular adhesion bonds.* Biophysical Journal **72**, 1541–1555 (1997)

[206] S. Dmitrieff and F. Nédélec. *Membrane mechanics of endocytosis in cells with turgor.* PLoS Computational Biolology **11**, e1004538 (2015)

[207] E. Loiseau, J. A. M. Schneider, F. C. Keber, C. Pelzl, G. Massiera, G. Salbreux, and A. R. Bausch. *Shape remodeling and blebbing of active cytoskeletal vesicles.* Science Advances **2** (2016)

[208] P. Mangeat, C. Roy, and M. Martin. *Erm proteins in cell adhesion and membrane dynamics.* Trends in Cell Biology **9**, 187 – 192 (1999)

[209] D. Robinson, G. Cavet, H. Warrick, and J. Spudich. *Quantitation of the distribution and flux of myosin-ii during cytokinesis.* BioMed Central Cell Biology **3** (2002)

[210] E. Kreyszig. *Differential Geometry.* Dover Publications, New York (1959)

[211] M. Deserno. *Fluid lipid membranes: From differential geometry to curvature stresses.* Chemistry and Physics of Lipids **185**, 11–45 (2015)

[212] R. G. Parr. *Density-Functional Theory of Atoms and Molecules.* Oxford University Press, New York (1989)

[213] K. Atkinson. *An Introduction to Numerical Analysis.* Wiley, New York (1988)

[214] I. N. Bronshtein, K. A. Semendyayev, G. Musiol, and H. Mühlig. *Handbook of Mathematics.* Springer, Berlin Heidelberg (2007)

[215] R. W. D. Nickalls. *Viète, descartes and the cubic equation.* The Mathematical Gazette **90**, 203–208 (2006)

[216] R. Capovilla and J. Guven. *Stresses in lipid membranes.* Journal of Physics A: Mathematical and General **35**, 6233 (2002)

LIST OF FIGURES

1.1 Illustration of the internal cell organization 20
1.2 Illustration of the cell membrane with the underlying cell cortex 23
1.3 Cell pole oscillations during cytokinesis 27
1.4 Schematic of a fluctuating membrane 32
1.5 Schematic of two special parameterizations for curves and surfaces 35
1.6 Local membrane deformations during cytokinesis 40
1.7 Illustration of membrane buckling induced by lateral compression 41
1.8 Illustration of an anchored membrane buckled due to available excess area 43

2.1 Illustration of a membrane sheet 46
2.2 Membrane sheet bound to a square lattice of discrete anchoring points 48
2.3 Surface tension of an anchored membrane sheet 53
2.4 Resistive forces at the membrane anchoring points 55
2.5 Equilibrium shapes of a membrane sheet anchored to a square lattice of discrete anchoring points 57

3.1 Illustration of a membrane protrusion with axial symmetry . . . 62
3.2 Equilibrium shapes of a membrane protrusion 67
3.3 Stability of compressed membrane protrusions 70
3.4 Formation of membrane tubes 72
3.5 Surface tension of a membrane protrusion 75
3.6 Lateral tension of a membrane protrusion 77
3.7 Membrane structured as a collection of protrusions 80
3.8 Equilibrium shapes of coupled membrane protrusions 83

3.9 Stability of a homogeneous excess area distribution for a collection of protrusions 85
3.10 Shape states for a collection of protrusions perturbed by local point forces 89

4.1 The cell membrane as a regular mesh of protrusions with axial symmetry 93
4.2 Global cell parameters determined through the interplay of cell membrane and cell cortex 100
4.3 Theoretical prediction for cell blebbing and cortex driven tubulation 106
4.4 Membrane perturbations caused by local anchoring forces 110
4.5 Cross section of a cell during cytokinesis 113
4.6 Membrane flow across the cleavage furrow 116
4.7 Surface elasticity caused by membrane buckling 121

5.1 Membrane buckling during bleb retraction 127
5.2 Experimentally measured membrane protrusions fitted by theoretical shapes 128
5.3 Membrane sheet bound to a hexagonal lattice 129

A.1 Schematic of a parameterized curved surface 134

C.1 Truncation error of the function $\overline{\Gamma}_\alpha(\overline{x}, \overline{y})$ 160
C.2 Higher order equilibrium solutions of an anchored membrane sheet 162
C.3 Surface tension of an anchored membrane sheet 165

D.1 Comparison of two different initial profiles ψ_{initial} 171
D.2 Steady state convergence of the numerical evaluation 175
D.3 Convergence of the numerical solution for a decreasing discretization step 177
D.4 Divergence of the analytical solution from the full numerical solution for increasing excess area 178

E.1 Equilibrium properties of a membrane protrusion in weak-bending approximation. 185
E.2 Schematic of a membrane protrusion approximated by a spherical cap 187
E.3 Surface tension of a membrane protrusion shaped as spherical cap 188

E.4 Schematic of a cylindrical membrane tube 189
E.5 Equilibrium properties of a cylindrical membrane tube 192

G.1 Schematic of the geometrical relations between spherical cap membrane protrusion and cell cortex 199

Versicherung

Hiermit versichere ich, dass ich die vorliegende Arbeit ohne unzulässige Hilfe Dritter und ohne Benutzung anderer als der angegebenen Hilfsmittel angefertigt habe; die aus fremden Quellen direkt oder indirekt übernommenen Gedanken sind als solche kenntlich gemacht. Die Arbeit wurde bisher weder im Inland noch im Ausland in gleicher oder ähnlicher Form einer anderen Prüfungsbehörde vorgelegt.
Die Arbeit wurde am Max-Planck-Institut für Physik komplexer Systeme angefertigt und von Dr. Guillaume Salbreux betreut.
Ich erkenne die Promotionsordnung der Fakultät Mathematik und Naturwissenschaften der Technischen Universität Dresden an.

Jochen A. M. Schneider